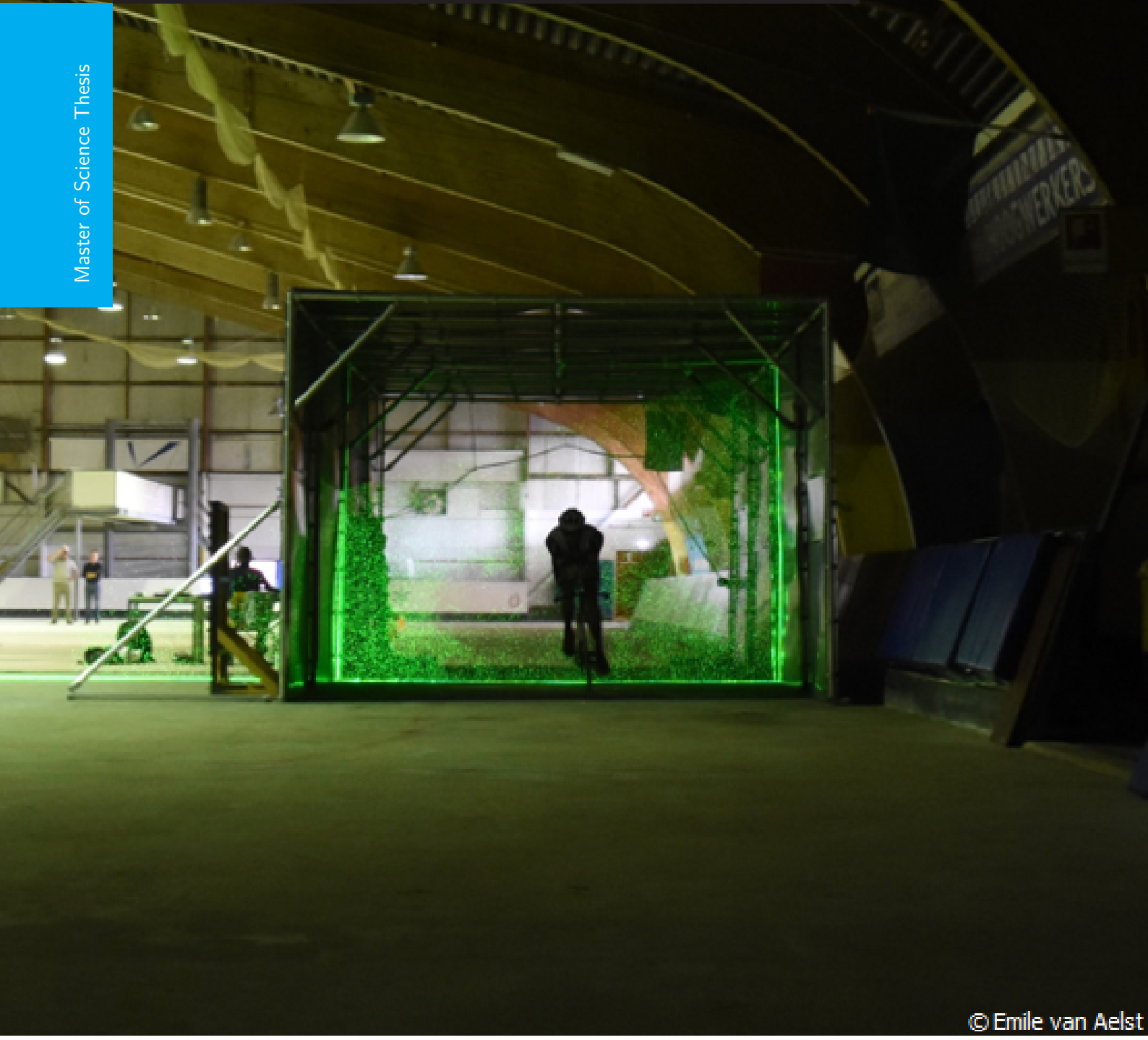


Accuracy assessment of the Ring of Fire system for on-site aerodynamic drag measurements

Maximilian Hirsch

Master of Science Thesis



© Emile van Aelst

**ACCURACY ASSESSMENT OF THE
RING OF FIRE SYSTEM FOR ON-SITE
AERODYNAMIC DRAG MEASUREMENTS**

by

Maximilian Hirsch

in partial fulfillment of the requirements for the degree of

Master of Science
in Aerospace Engineering

at the Delft University of Technology,
to be defended publicly on Wednesday, December 19th, 2018 at 12:00 AM.

Student number:	4161424	
Project duration:	April 24th, 2018 - December 19th, 2018	
Supervisor:	Dr. A. Sciacchitano	
Thesis committee:	Prof. dr. F. Scarano,	Chairman
	Dr. A. Schwab,	External Member
	Ir. A. Spoelstra,	Daily supervisor

An electronic version of this thesis is available at <http://repository.tudelft.nl/>.

PREFACE

The present work concludes the master in the Aerodynamics profile at the Aerospace Engineering faculty at the Technical University of Delft. Earlier this year, in April, Dr. Andrea Sciacchitano and Ir. Alexander Spoelstra gave me the opportunity to continue the work on the Ring of Fire, a project that combines two passions of mine, namely aerodynamics and cycling. For their trust in me and their continuous support as supervisors throughout the project, I am deeply thankful. I highly benefited from their advice and expertise and thoroughly enjoyed working alongside them.

For the experimental campaign within the framework of this thesis, I do have to express my gratitude to all parties involved in making this test possible. To begin with, I would like to thank Team Sunweb for providing the necessary cycling equipment and in particular Tom Davis for good communication throughout the project. I thank Albert Timmer and Floortje Mackaij for sacrificing their time to ride a combined 550 laps or 105km. At this point, I would also like to mention Florian who travelled from Germany to offer me his help as a test rider. Furthermore, I highly appreciate the cost-free support from SRM by providing us with a high-end power meter for the test duration. In addition, the assistance we received from the staff of the ice-rink in Leiden was very welcomed.

Thank you also to the staff of the High-speed Laboratory: Dennis Bruikman, Peter Duyndam and Frits Donker for their support in Leiden, as well as Nico van Beek and Colette Russo for their organizational assistance throughout the project. Additionally, I thank Rado Dukalski for showing his enthusiasm about the project and providing me with media documents of the campaign.

I would further like to use this opportunity to thank my friends who made these last seven years here in Delft unforgettable. Thank you Arwin, Conni, Martin, Nils, Radu and Sid for creating memories that I will be very happy to look back to. Finally, and most importantly, I would like to express my deepest gratitude to my girlfriend, Hanna, my sister, Katharina and my parents Andrea and Ralph. The amount of support I received from them over all those years cannot be expressed in words and I would not have been able to pursue any of my personal or professional dreams without them.

*Maximilian Hirsch
Delft, December 2018*

ABSTRACT

The continuous pursuit of reducing drag in many speed sports, such as cycling and ice-skating, demands novel approaches to gain further insight into flow phenomena around athletes. In recent years, the Ring of Fire measurement technique has emerged as a feasible option to visualise and analyse flow structures of transiting objects based on particle image velocimetry. The accuracy of this on-site measurement technique has not yet been validated under equal test conditions.

This master's thesis aims to compare drag area values of a cyclist from Ring of Fire measurements to simultaneously acquired power meter data. Tests with the cyclist in upright and time-trial posture, as well as different helmet types and various drafting distances, are envisaged to assess the correlation between the two measurement techniques in multiple drag area regimes, and to gain insight into large distance drafting above 3m, which, to the best knowledge of the author, has not yet been studied in academic research. In addition, the campaign plans to remove any user operations during the test, which would be another step towards a fully autonomous Ring of Fire system, as envisioned in the future. A spacious indoor facility is suggested as the testing site to minimize environmental effects and to allow for the continuous motion of the cyclist. The Ring of Fire method shows great potential, as the measurements are conducted under simulated racing conditions and wake visualisation allows the operator to locate origins of drag. Validating the drag area results could further attest to the Ring of Fire's viability as an optimisation tool in the upcoming years.

The conducted campaign, within the framework of this thesis, indicates good agreement between the power meter and Ring of Fire techniques when assessing the relative drag area delta of a small-scale helmet change and a large-scale posture change. In terms of absolute values, the power meter model shows a high dependency on underlying model constants. Using literature-based coefficients, the absolute $C_d A$ values are within 5% of the Ring of Fire derived values.

Furthermore, the feasibility of evaluating long distance drafting effects with the Ring of Fire system is demonstrated. Measurable drag area savings of 15% are obtained by the trailing cyclist at front wheel to front wheel distances of 7 – 9m. Due to non-uniform inflow conditions in front of the trailing cyclist, a wake contouring algorithm needed to be employed to satisfy mass preservation within the control volume by resizing the inlet and outlet plane. In addition, enclosure of the wake structure and contouring of a representative inlet plane is achieved. The flow topology in the wake of the trailing cyclist is acquired by a stereo-PIV system. Primary wake structures, as well as in-plane velocity fields, are comparable to those observed behind isolated riders.

CONTENTS

Preface	iii
Abstract	v
List of Figures	xi
List of Tables	xv
Nomenclature	xvii
1 Background	1
2 Literature Study	3
2.1 Ring of Fire Method	3
2.2 Aerodynamic Effect of Helmet Shape	6
2.3 Drag Savings in Drafting Configuration	8
2.3.1 Wind Tunnel Studies on Drafting	8
2.3.2 On-site Studies on Drafting	9
2.3.3 Numerical Studies on Drafting	10
2.4 Flow Topology Behind Cyclist in Time-Trial Position	14
2.4.1 Wake Topology of Individual Cyclist	14
2.4.2 Wake Topology of Trailing Cyclist	17
2.4.3 Wake Behaviour Far Downstream	19
2.5 Objective and Relevance of This Thesis	20
2.6 Outline of This Report	20
3 Theoretical Framework	21
3.1 Resistive Forces During Cycling	21
3.2 Drag Area Evaluation Through Power Meter	22
3.3 Working Principle of Particle Image Velocimetry	24
3.3.1 Tracer Particles	25
3.3.2 Particle Imaging	26
3.3.3 Stereoscopic PIV	27
3.4 Control Volume Approach	29
4 Experimental Installation, Settings and Procedure	33
4.1 Ring of Fire Setup	33
4.1.1 Test Facility	33
4.1.2 Tunnel Structure	34
4.1.3 Laser Light	35
4.1.4 Acquisition Hardware	35
4.1.5 Seeding Production	36
4.1.6 Triggering Hardware	37
4.1.7 Drafting Distance	37

4.2	Test Objects	38
4.2.1	The Riders	39
4.2.2	The Bicycles	39
4.2.3	Power Measuring Device	40
4.3	Acquisition System Test Settings	41
4.3.1	Pulse Separation Time, Δt	41
4.3.2	Time Delay of Trigger	41
4.3.3	Images per Loop	42
4.3.4	Recording Frequency of the PIV-System	42
4.4	System Calibration	42
4.5	Testing Schedule	43
4.6	Testing Procedure	44
5	Data Reduction and Analysis Techniques	47
5.1	Data Reduction of Power Meter Data	47
5.1.1	Velocity Correction	47
5.1.2	Relative Velocity	48
5.1.3	Outlier Removal Power Meter Data	49
5.2	Data Reduction of PIV Measurement Data	49
5.2.1	Pre-Processing	49
5.2.2	Vector Processing	51
5.2.3	Post-Processing	51
5.2.4	Outlier Removal PIV Data	52
5.3	Contouring of Inlet and Outlet Plane	52
5.3.1	Selecting Wake Contour	52
5.3.2	Contour Adaptation for Mass Conservation	54
5.4	Upstream Pressure Propagation of Cyclist	55
5.5	Choice of Inlet Plane Under Drafting Conditions	56
5.6	Longitudinal Wake Alignment	57
5.7	Determination of Drafting Distance	58
5.7.1	Drafting Distance Extracted from Video	59
5.7.2	Drafting Distance Extracted from PIV Images	60
5.7.3	Drafting Distance Measurement Technique Comparison	60
5.8	Synchronization of the Data Acquisition Systems	61
6	Results and Discussion	63
6.1	Power Meter Results	63
6.1.1	Linear Regression Analysis for C_{rr} Value	63
6.1.2	Phase-Averaged Power Meter Data	64
6.1.3	CdA Value from Power Meter	65
6.2	Ring of Fire Results	67
6.2.1	CdA Value from Individual Tests	67
6.2.2	CdA Value from Drafting Tests	69
6.3	Comparison CdA Between Power Meter and Ring of Fire	71
6.4	Drag Savings Under Drafting Condition	73
6.5	Flow Topology Under Drafting Conditions	75
6.5.1	Mean Out-of-Plane Velocity Upstream	75
6.5.2	Mean Out-of-Plane Velocity Downstream	76
6.5.3	Mean Vorticity in Wake	76

7 Conclusion and Recommendations	79
Bibliography	83
A Seeding Problem Induced by Circulation	
B Sample Code for Wake Contouring Procedure	

LIST OF FIGURES

1.1	Triathlete on normal road bike, 1982. Adapted from Allen (1982).	1
1.2	Triathlete breaking course record with 4:18h, 2006. Adapted from Hill (2006).	1
1.3	Triathlete riding third fastest bike time in 2017 with 4:14h. Adapted from Rauschendorfer (2017).	1
1.4	Baseline extension bar setup with existing gap. Adapted from Hilger (2018).	2
1.5	Innovative 3D printed aerobars, individually shaped to fit the cyclist's arm. Adapted from Rauschendorfer (2018).	2
1.6	Pro athletes spaced at minimum legal drafting distance for aerodynamic benefit. Adapted from Wechsel (2017).	2
2.1	Conceptual integration of Ring of Fire system in velodrome (Sciacchitano et al., 2015)	4
2.2	Feasibility study of Ring of Fire approach on a transiting sphere (Terra et al., 2017)	4
2.3	Outdoor large-scale Ring of Fire using high-speed cameras (Spoelstra et al., 2018)	5
2.4	Indoor large-scale Ring of Fire using low-speed cameras, enlarged tunnel structure (de Martino Norante, 2018)	5
2.5	Wind tunnel test setup of Blair and Sidelko (2009)	6
2.6	Wind tunnel test setup of Alam et al. (2014)	6
2.7	Streamline plots of three helmet configurations tested by Beaumont et al. (2018)	7
2.8	Setup by Zdravkovich et al. (1996) in staggered arrangement	8
2.9	Wind tunnel test at minimum separation distance, as conducted in Barry et al. (2014a)	8
2.10	Wind tunnel study with four in-line cyclists as conducted by Barry et al. (2015)	9
2.11	Pressure interaction between two drafting cyclists (Blocken et al., 2013)	11
2.12	Pressure distribution on cyclists as presented in Blocken et al. (2013)	11
2.13	Velocity plot at 0.1 m wheel gap as simulated by Swissside (2017)	12
2.14	Velocity plot at 10 m wheel gap as simulated by Swissside (2017)	12
2.15	Streamwise isosurface vorticity plot as created by Jux et al. (2018) based on a wind tunnel experiment	14
2.16	Labelled streamwise vorticity plots behind individual cyclist	16
2.17	Water tunnel setup by Barry et al. (2016a) using a single PIV measurement plane.	17
2.18	8 PIV measurement planes in front and behind the trailing cyclist as used in Barry et al. (2016a).	17
2.19	Streamwise vorticity behind rider in asymmetric position (Barry et al., 2016a).	17
2.20	Streamwise velocity upstream of trailing cyclist at gap of 1/11 (left) and 1 (right) bike length (Barry et al., 2016a)	18
2.21	Phase-averaged streamwise vorticity plots by Barry et al. (2016b). Upper row isolated rider, lower row trailing cyclist	18
2.22	Time-averaged normalized streamwise velocity behind cyclist (Barry et al., 2016b)	18
2.23	Normalized streamwise velocity plots at distance x behind cyclist obtained from Ring of Fire measurements	19
2.24	Asymmetric flow topology in the wake (Crouch et al., 2017)	19
2.25	Streamwise vorticity at 3.025 m behind cyclist (Spoelstra, 2017)	19
3.1	Schematic representation of opposing forces during cycling	21

3.2	Interpolated drivetrain efficiency, based on measurements conducted in Hinzen et al. (2012)	23
3.3	Linear regression analysis to determine C_{rr} (Debraux et al., 2011)	24
3.4	Process flow schematic of a planar PIV system, adapted from Giaquinta (2018)	25
3.5	Light scattering of a $4\mu\text{m}$ sized water droplet at (0,0,0) with $\lambda = 633\text{nm}$ (Normal vector of light ray [0 1 0]). Adapted from Michels (2010).	26
3.6	Translation stereo-PIV configuration (Prasad, 2000)	27
3.7	Angular-displacement stereo-PIV configuration (Prasad, 2000)	27
3.8	Stereo angle causes uniform grid in image plane to become warped in object plane. Adapted from Prasad (2000).	28
3.9	Construct out-of-plane velocity vector (Raffel et al., 2007)	29
3.10	Control Volume around a cyclist	30
4.1	Top view of testing ground	34
4.2	Tunnel structure (side/rear view)	35
4.3	1) BNC cable - 2) Multi-angle mount - 3) MDR cables - 4) sCMOS camera - 5) Scheimpflug adapter - 6) Lens - 7) Bandpass filter	36
4.4	Seeding rake attached to vertical tunnel beam standing in a sump	36
4.5	1) Drafting camera - 2) Evergreen Laser - 3) Laser line for lateral position - 4) Seeding rake - 5) PC Terminal - 6) PTU - 7) sCMOS camera right - 8) Suspended MDR cable - 9) PHD interface box - 10) PHD receiver - 11) sCMOS camera left - 12) Convergent trajectory markings - 13) PHD transmitter	38
4.6	Helmet types used throughout the campaign	39
4.7	Giant Trinity Advanced SL 2018	40
4.8	Power measuring system	41
4.9	Side view to scale of acquisition phase at $V = 30\text{kmh}^{-1}$ and $f_{rec} = 15\text{Hz}$. Time starts at passage of photo-detector	42
4.10	Big calibration plate with enlarged image of geometrical calibration	43
4.11	Experimental procedure	45
5.1	Difference in trajectory between wheel and CG	48
5.2	FBD during cornering to obtain lean angle Φ	48
5.3	Phase-averaged velocity plot using data of individual upright test at 8.33ms^{-1}	48
5.4	Comparison between raw image (left) and fully pre-processed image (right)	50
5.5	Signal-to-noise ratio for each vector resulting from the vector processing of the raw image (left) and the filtered image (right)	50
5.6	Signal-to-noise ratio for 1.5 m behind cyclist (left) and 4 m behind cyclist (right)	51
5.7	Flow schematic of contouring procedure	53
5.8	Contour adaptation of fixed inlet, variable outlet plane case (contour color corresponds to color framing the wake plane)	54
5.9	Contour adaptation of fixed outlet, variable inlet plane case (contour color corresponds to color framing the inlet plane)	55
5.10	Pressure coefficient in centre line plane (Blocken et al., 2016). Box illustrates area of interest. (Gap between cyclist and motorbike is 7.5 m.)	56
5.11	Effect of inlet plane choice on the CdA value for trailing cyclist at 11–13 m drafting distance. Images above show out-of-plane velocity, ranging from -2 to 1ms^{-1} , together with the applied contour	57
5.12	Streamwise relocation of wake planes with respect to the rear portion of the rear wheel	58
5.13	Cropped and filtered image extracted from video, capturing side view of the cyclists before entering the tunnel	59

5.14 Last image of leading cyclist (left) and first image of trailing cyclist (right) traversing the laser sheet at two different time stamps	60
5.15 Comparison between the two approaches based on the video and the PIV images, respectively	61
6.1 Linear regression to determine C_{rr} . Data recorded at velocities of 15–33 km h ⁻¹ in steps of 3 km h ⁻¹	64
6.2 Phase-locked velocity, power, cadence, and drag area traces over one lap. Data from 30 km h ⁻¹ upright individual test	65
6.3 Drag area coefficient derived from power meter results. Drafting tests were conducted in time-trial posture with a road helmet	66
6.4 Streamwise CdA evolution in wake of individual cyclist at 30 km h ⁻¹	68
6.5 Streamwise CdA evolution in wake of trailing cyclist at 30 km h ⁻¹ under drafting conditions	70
6.6 Comparison of drag area coefficients between power meter and Ring of Fire.	71
6.7 Reynolds number dependency of individual body parts and the entire cyclist as computed by numerical studies and a full scale wind tunnel experiment (all tests in TT position). Reproduced from Defraeye et al. (2011)	73
6.8 Drag area coefficient change in drafting conditions at 30 km h ⁻¹ as measured by the Ring of Fire	74
6.9 Normalized out-of-plane velocity 1.3–1.7 m upstream of cyclist	75
6.10 Normalized out-of-plane velocity 0.4–0.6 m downstream of cyclist	76
6.11 Streamwise vorticity 0.4–0.6 m downstream of cyclist	77
6.12 Schematic showing responsible flow features for downwashed wake, as well as upper wake narrowing and lower wake broadening.	78
A.1 Bubbles carried downstream immediately after production by seeding rake	
A.2 Initial seeding distribution in measurement plane	
A.3 Mats and later blanket carried by one operator in opposite cycling direction to reduce circulation effect in tunnel.	
A.4 Improved seeding distribution in measurement plane due to reduced circulation	

LIST OF TABLES

2.1	Summary of drafting studies	13
4.1	Test matrix	44
6.1	Drag area coefficient in the four drafting zones. Standard deviation of drafting distance in brackets.	70
6.2	$\overline{CdA[m^2]}$ with $\Delta\overline{CdA[m^2]}$ in brackets w.r.t to individual time-trial test with time-trial helmet	72

NOMENCLATURE

ABBREVIATIONS

BFS	Bubble fluid solution
BNC	Bayonet Neill–Concelman
CFD	Computational fluid dynamics
CG	Centre of gravity
CI	Confidence interval
CMOS	Complementary metal-oxide-semiconductor
DSLR	Digital single-lens reflex camera
DSR	Dynamic spatial range
DVR	Dynamic velocity range
FBD	Free-Body Diagram
FSU	Fluid supply unit
HFSB	Helium-filled soap bubbles
LES	Large eddy simulation
MDR	Mini D Ribbon
Nd:YAG	Neodymium-doped yttrium aluminum garnet
PHD	Photo-detector
PIV	Particle image velocimetry
PM	Power meter
ppp	Particles per pixel
PTU	Programmable timing unit
RANS	Reynolds averaged Navier Stokes
sCMOS	Scientific complementary metal-oxide-semiconductor
SNR	Signal-to-noise ratio
SRM	Schober Rad Messtechnik
SSD	Solid-state drive
TT	Time-trial
UCI	Union Cycliste Internationale

LIST OF SYMBOLS

A	Frontal surface area	$[m^2]$
α	Angle between cameras and z-axis in XZ-plane	$[\circ]$
β	Angle between cameras and z-axis in YZ-plane	$[\circ]$
CdA	Drag area coefficient	$[m^2]$
C_p	Pressure coefficient	$[-]$
C_{rr}	Rolling resistance coefficient	$[-]$
D_{aero}	Aerodynamic drag force	$[N]$
$D_{bearing}$	Drag force from bearings	$[N]$
$D_{drivetrain}$	Drag force from drivetrain	$[N]$
$D_{rolling}$	Rolling resistance	$[N]$
D_{total}	Total drag force	$[N]$
d_{diff}	Diffraction diameter	$[m]$
$d_{drafting}$	Drafting distance front wheel to front wheel	$[m]$
d_{geom}	Geometrical diameter of particle	$[m]$
d_i	Distance sensor to lens	$[m]$
d_{inter}	Distance on bike where laser intersects	$[m]$
d_o	Distance object to lens	$[m]$
d_p	Diameter of particle	$[m]$
$d_{phd-laser}$	Distance photo-detector to laser	$[m]$
d_{τ}	Particle Image diameter	$[m]$
$d_{\#i}$	Distance of image behind rear wheel	$[m]$
Δt	Pulse separation time	$[s]$
Δx	Horizontal displacement in image plane	$[m]$
Δy	Vertical displacement in image plane	$[m]$
δz	Focal depth	$[m]$
e	Error-ratio	$[-]$
F	Force	$[N]$
f	Focal length	$[m]$
f_{rec}	Recording frequency	$[Hz]$
$f\#$	F-stop	$[-]$
g	Gravitational acceleration	$[ms^{-2}]$
h_{cog}	Height centre of gravity	$[m]$
I_p	Particle scattering intensity	$[Wm^{-2}]$
l_{bike}	Length bike	$[m]$
$\#I$	Image number	$[-]$
λ	Laser wavelength	$[m]$
M	Magnification factor	$[-]$
m	Mass of cyclist and bike	$[kg]$
μ	Dynamic viscosity	$[kgm^{-1}s^{-1}]$
\mathbf{n}	Normal vector	$[-]$
n_{images}	Number of images	$[-]$
$n_{samples}$	Number of samples	$[-]$
$\eta_{drivetrain}$	Drivetrain efficiency	$[\%]$
$P_{athlete}$	Instantaneous power by rider	$[W]$
P_{total}	Total power	$[W]$
p	Local static pressure	$[Pa]$
p_{∞}	Freestream static pressure	$[Pa]$
Φ	Lean angle	$[\circ]$
r_{cog}	Corner radius centre of gravity	$[m]$
r_w	Corner radius wheel	$[m]$

ρ	Density of air	$[kgm^{-3}]$
ρ_p	Density of particle	$[kgm^{-3}]$
S	Surface area	$[m^2]$
S_p	Particle's Stokes number	$[-]$
t	Time	$[s]$
$t_{acquisition}$	Duration of acquisition	$[s]$
$t_{delay_{max}}$	Maximum time delay	$[s]$
t_{lap}	Duration of one lap	$[s]$
$t_{storing}$	Storing duration	$[s]$
θ	Polar coordinate of corner	$[^\circ]$
$\bar{\tau}$	Viscous stress tensor	$[Pa]$
τ_p	Particle's response time	$[s]$
\mathbf{u}	Fluid velocity	$[ms^{-1}]$
u	Horizontal velocity in object plane	$[ms^{-1}]$
$u_{1,2}$	Horizontal velocity in image plane	$[ms^{-1}]$
u_c	Velocity cyclist	$[ms^{-1}]$
u_{inlet}	Out-of-plane velocity in inlet plane	$[ms^{-1}]$
u_{outlet}	Out-of-plane velocity in outlet plane	$[ms^{-1}]$
V	Control volume	$[m^3]$
V	Velocity	$[ms^{-1}]$
V_{rel}	Relative velocity	$[ms^{-1}]$
v	Vertical velocity in object plane	$[ms^{-1}]$
$v_{1,2}$	Vertical velocity in image plane	$[ms^{-1}]$
v	Out-of-plane velocity in object plane	$[ms^{-1}]$
$w_{shoulder}$	Width shoulder	$[m]$
\mathbf{x}	Position vector	$[m]$
x	Streamwise direction	$[m]$
x_{rw}	Streamwise distance behind rear wheel	$[m]$

1

BACKGROUND

In long-distance triathlon events, the best athletes spend around 4 h on the bike, covering the 180 km long bike course at an average velocity of 45 km h^{-1} . Marginal improvements in drag value accumulate over time to create large differences in energy expenditure and could be the decisive factor in the upcoming marathon, and ultimately in winning or losing the race.

Kyle et al. (2004) proposed that at cycling velocities beyond 15 km h^{-1} , the aerodynamic drag becomes the dominant resistance. At common race speeds exceeding 40 km h^{-1} , more than 90 % of the athlete's power is expended to overcome the air resistance as suggested by Kyle et al. (1984) and later confirmed by Grappe et al. (1997), Di Prampero (2000), Belluye et al. (2001) and Lim et al. (2011). It is therefore essential to optimise the aerodynamic efficiency of the entire system in order to gain an advantage over the competition.

Over the course of the last 40 years, an ever-increasing effort was made to minimize the aerodynamic drag in triathlon cycling. Compared to professional cycling, which is governed by rules of the UCI, triathlon bikes enjoy more relaxed rules concerning frame geometry, rider seating position, hydration, and other storage systems (Crouch et al., 2017). The development in bike technology is apparent in Figures 1.1, 1.2 and 1.3.



Figure 1.1: Triathlete on normal road bike, 1982. Adapted from Allen (1982).



Figure 1.2: Triathlete breaking course record with 4:18h, 2006. Adapted from Hill (2006).



Figure 1.3: Triathlete riding third fastest bike time in 2017 with 4:14h. Adapted from Rauschendorfer (2017).

Here, the round frame tubes were replaced with airfoil shaped elements. The standard road bike drops were removed and a pair of aerobar extensions was added. Integrated cables and novel storage solutions were employed to further decrease the drag. Finally, deep rim bike wheels, aerodynamically shaped helmets, and long-sleeve skin suits proved to be very effective in the pursuit of drag reduction.

Figures 1.4 and 1.5 demonstrate an example of the effort spent to marginally improve the aerodynamic efficiency of a professional athlete. Here, a titanium aero bar pair was individually designed and 3D printed for a customized fit with the athlete's arm, removing the existing gap between the round-tubed extension and the lower arm itself. This further allows for the leading edge of the aero bar-arm system to be optimally shaped. A measurable drag benefit of the novel solution is claimed to be in the range of 1–2 % based on wind tunnel testing.



Figure 1.4: Baseline extension bar setup with existing gap. Adapted from [Hilger \(2018\)](#).



Figure 1.5: Innovative 3D printed aero bars, individually shaped to fit the cyclist's arm. Adapted from [Rauschendorfer \(2018\)](#).

To preserve the spirit of an individual effort, drafting another contestant at less than 12 m distance is prohibited, measured from front wheel to front wheel and according to the official racing regulations a violation of this rule would result in a time penalty ([Ironman, 2018](#)). However, various non-academic sources and athletes have reported a noticeable drag benefit even outside the 12 m range, which is underlined by Figure 1.6, showing the professional athletes in non-staggered configuration, riding as close to the legal limit as possible to gain the maximum aerodynamic advantage.



Figure 1.6: Pro athletes spaced at minimum legal drafting distance for aerodynamic benefit. Adapted from [Wechsel \(2017\)](#).

2

LITERATURE STUDY

This chapter begins in section 2.1 with an introduction to the emerging Ring of Fire measurement technique and its reached milestones over recent years. Thereupon, previously conducted research on the aerodynamic efficiency of different cycling helmet types are presented in section 2.2. Sections 2.3 and 2.4 intend to provide an overview of relevant studies on drafting in cycling, covering both aerodynamic drag savings, as well as encountered flow field changes. The chapter is concluded with the research objective and its relevance in section 2.5, before an outline of the remaining report is provided to the reader in section 2.6.

2.1. RING OF FIRE METHOD

Nowadays, professional and ambitious amateur athletes are seeking small aerodynamic improvements relying on wind tunnel balance measurements, velodrome tests, and outdoor field tests. Many new companies have specialized in offering such testing days, which underlines the growing importance and demand on improving the aerodynamic efficiency. However, one of the big drawbacks of these traditional testing methods is that they act as a black box, as only overall drag data can be extracted, without visualizing the flow structures around the cyclist, which could be used to identify the region that offers the greatest potential. In order to gain further insight into the flow around the cyclist, other approaches need to be tested. One of the methods is CFD (Computational Fluid Dynamics) which allows simulating the airflow around the cyclist numerically. Even though this method shows the capability of simulating complex flows in sports, as shown in [Gardan et al. \(2017\)](#), it is often limited to an idealized environment without modelling the transiting behaviour occurring in most sports, like the pedalling motion of a cyclist.

In recent years, particle image velocimetry (PIV) has grown in popularity, as an alternative method to visualize the flow field around an object. This technique relies on the tracking of small particles, which are illuminated by short light pulses, while their positions are recorded by one or more high-performance cameras. Through post-processing methods, it is possible to reconstruct instantaneous velocity fields of the measurement volume and to retrieve quantitative flow information, like pressure. Even though small tracer particles are inserted into the flow, PIV is considered a non-intrusive measurement technique. The tracer particles are carefully selected based on their light scattering properties and their ability to follow the motion of the flow ([Raffel et al., 2007](#)).

Until lately, PIV measurement volumes were constrained to small dimensions, limiting the model size and thus the Reynolds number, as similarity parameter to full-size objects. [Bosbach et al. \(2008\)](#) investigated the use of Helium-filled soap bubbles (HFSB) with a diameter of 0.2–0.3 mm as possible tracer particles. Improved light scattering properties were assigned to the HFSB over typically used

micron-sized tracer particles. This enabled the authors to trace the bubbles in an area of interest spanning 7 m^2 , proving the feasibility of large-scale PIV measurements. However, due to low bubble production rates, HFSB seeding was not applicable to wind tunnel tests at that time. [Scarano et al. \(2015\)](#) demonstrated the feasibility of using Helium-filled soap bubbles in the sub-millimetre regime by achieving good tracing properties in the flow upstream of a circular cylinder. The authors additionally accomplished a faster tracer production, yielding to a higher particle concentration in large test volumes and thus paving the way for large-scale measurements in the wind tunnel.

Thereupon, [Sciacchitano et al. \(2015\)](#) proposed the Ring-of-Fire approach, where tomographic-PIV is utilized to gain quantitative insight into the flow around a cyclist, traversing a measurement volume of more than $10,000 \text{ cm}^3$. The authors envision, performing the experiment in a velodrome to imitate racing conditions with the test object in motion, which cannot be simulated in wind tunnels or numerical methods. Until now, no velodrome test has been performed, as the soap bubbles might harm the wooden track surface and cause slippery conditions for the test cyclists. A conceptual integration of the setup is illustrated in [Figure 2.1](#).

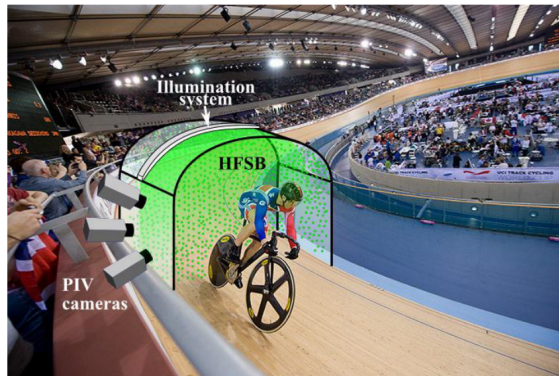


Figure 2.1: Conceptual integration of Ring of Fire system in velodrome ([Sciacchitano et al., 2015](#))

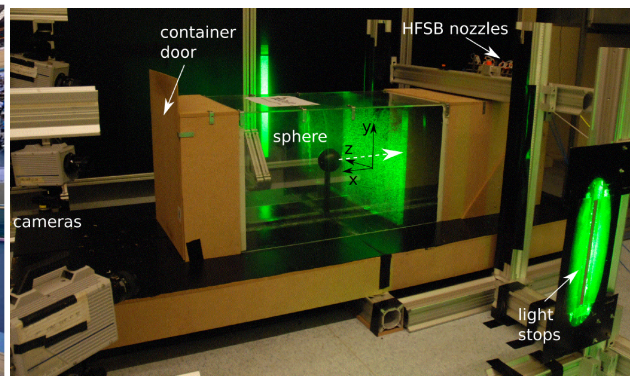


Figure 2.2: Feasibility study of Ring of Fire approach on a transiting sphere ([Terra et al., 2017](#))

As an initial study on the proposed Ring of Fire technique, [Terra et al. \(2017\)](#) carried out a tomographic PIV experiment, measuring the aerodynamic drag of a sphere with a diameter of 0.1 m , as seen in [Figure 2.2](#). During the test, the sphere transits a PIV measurement volume at 1.5 ms^{-1} . Using the time-averaged momentum equation it is possible to apply momentum conservation in a control volume, as depicted in [Anderson \(2011\)](#). By comparing the flow field parameters before and after the passage of the sphere it is possible to determine the sphere's drag force. The results show large drag fluctuations when taking wake data close to the sphere ($x/0.1 \text{ m} < 2$), where the pressure term plays a dominant role. Further downstream, the drag value plateaus, as the pressure term approaches zero. In the regime of ($x/0.1 \text{ m} > 2$) the drag value of the sphere is overestimated by 8–20 %, compared to literature values. The author explains this behaviour by the presence of the sphere's support strut, which adds to the momentum deficit in the wake.

The first large-scale Ring of Fire experiment was conducted by [Spoelstra et al. \(2018\)](#), using a high-speed stereo PIV setup recording at 2 kHz ([Figure 2.3](#)). The velocity component in the direction of a moving cyclist is captured over a measurement plane of $1000 \text{ mm} \times 1700 \text{ mm}$, with the cyclists transiting through the laser plane at a velocity of 8 ms^{-1} . The results of this test show little fluctuations in the drag area value for wake measurement taken further downstream than 3 m . The author concludes furthermore, that the drag delta between upright and time trial position matches previously published reference data well. However, compared to wind tunnel force balance measurements, performed in the same study with the same rider's posture and bike setup, the Ring of Fire showed a

30 % lower drag area value. The author applies a correction due to the missing interaction between a moving ground and the bike which reduces the difference between the two measurement techniques to 10 %. The remaining discrepancy could originate from a different rider's movement and posture on the bike, which are difficult to accurately repeat. Finally, the added model supports and the non-rotating wheels during the wind tunnel test are additional differences relative to the Ring of Fire test. In order to assess the accuracy of the Ring of Fire system, conducting simultaneous measurements with a power meter device, while the rider is passing through the Ring of Fire could lead to a more representative comparison.

In the latest Ring of Fire experiment, performed by [de Martino Norante \(2018\)](#), the author investigated the applicability of low-speed cameras, sampling at 8 Hz. One of the major disadvantages in the experiment by [Spoelstra et al. \(2018\)](#) was the storage time in the range of 5–8 min for the acquired images, delaying the progress of the campaign. The Ring of Fire setup in [de Martino Norante \(2018\)](#) was installed indoors, reducing the environmental effects, such as wind, on the measurements. Considering these two changes, the author sought to further improve the accuracy of the Ring of Fire compared to the maiden test. Any blockage effects of the tunnel, seen in [Figure 2.3](#), were eliminated by erecting a larger structure, as shown in [Figure 2.4](#). The previously stated adjustments lowered the uncertainty of the drag measurements from 5 %, as in [Spoelstra et al. \(2018\)](#) down to 2 %. The usage of low-speed cameras reduced the time interval between two consecutive runs to 1–2 min, with the high-speed camera used for velocity measurements being the limiting factor. The author suggests, relying on velocity data provided by a magnetic speed sensor mounted on the bike instead, to enable shorter time intervals between runs. Similar to the high-speed Ring of Fire study, the drag area plateaus at more than 3.3 m downstream of the cyclist. Furthermore, it has been established that in the far wake, the effect of the pedal position on the drag area value diminishes, due to mixing processes in the flow. The structures in the near wake of both the indoor and outdoor experiments are in agreement with the results of [Crouch et al. \(2014\)](#), who conducted a wake study using a pitot rake at various crank angles. Due to spatial limitations at the indoor facility, the experiment could not be performed continuously, as the cyclists needed to accelerate and decelerate for each run. The use of a larger indoor hall would allow the cyclist to ride at a constant velocity and thus also improving the consistency of the rider's posture between transits.

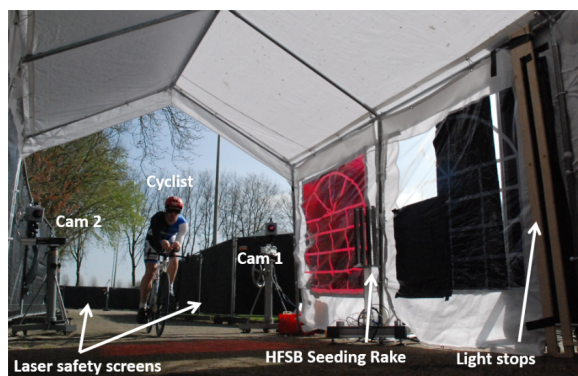


Figure 2.3: Outdoor large-scale Ring of Fire using high-speed cameras ([Spoelstra et al., 2018](#))

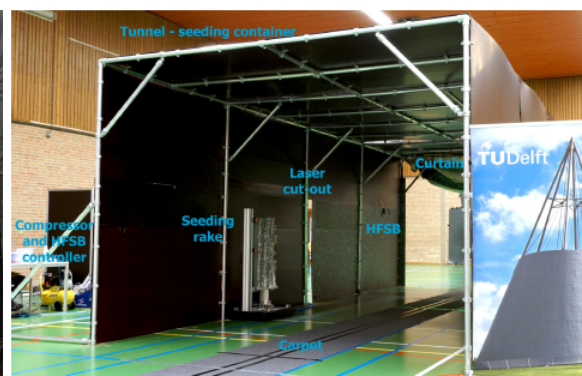


Figure 2.4: Indoor large-scale Ring of Fire using low-speed cameras, enlarged tunnel structure ([de Martino Norante, 2018](#))

The main restrictions in previous Ring of Fire measurements can be assigned to: Firstly, the limitation of space, which prevented the cyclist from maintaining a constant velocity. Secondly, extensive storage times of acquired images from a high-speed camera to derive the rider's velocity, causing long time intervals between measurements. And finally, missing validation of Ring of Fire results

with simultaneously acquired data.

2.2. AERODYNAMIC EFFECT OF HELMET SHAPE

In competitive cycling, the technical regulations of the UCI require all athletes to wear a helmet to lower the risk of head injuries [UCI \(2018\)](#). As with all parts on the bike, the helmet has evolved considerably over the years. Nowadays, the helmet serves not only the purpose of injury prevention but can also be designed to improve the thermal comfort or aerodynamic efficiency of the cyclist. In [Alam et al. \(2014\)](#), the authors mention that at speeds between 30–40 km h⁻¹ the various helmet shapes contribute to 2–8% of the overall drag. With most time-trial helmets the aerodynamic drag is lowered compared to no helmet ([Blair and Sidelko, 2009](#)). [Brownlie et al. \(2010\)](#) explain this behaviour with the non-streamlike shape of the head. The same article also emphasises that the drag difference between a road helmet and a time-trial helmet is significantly larger than the difference between two time-trial helmets.

[Alam et al. \(2010\)](#) conducted a study concerning the relation between increased ventilation and aerodynamic drag. The test consisted of six helmet shapes, ranging from low-cost road helmets to professional time-trial helmets with an aerodynamically-shaped tail. The test was carried out in a wind tunnel with the helmets mounted on a mannequin head. Lower drag area values were measured for the time-trial helmets when compared to the road type. This trend was confirmed by [Blair and Sidelko \(2009\)](#), where 10 different time-trial helmets were compared to a road helmet, mounted on an upper body mannequin in the wind tunnel, which is illustrated in [Figure 2.5](#). The authors found a measurable drag benefit of 1–1.5 N using a time-trial helmet over a road helmet at a test velocity of 13.4 ms⁻¹.

In [Alam et al. \(2014\)](#) the authors investigated the effect of surface roughness on the helmet by the addition of dimples, comparable to a golf ball. For this test, six different helmets were used, four time-trial helmets with a tail and two road helmets. Again, the helmets were installed on a mannequin placed in a wind tunnel, as shown in [Figure 2.6](#).



Figure 2.5: Wind tunnel test setup of [Blair and Sidelko \(2009\)](#)



Figure 2.6: Wind tunnel test setup of [Alam et al. \(2014\)](#)

One could argue, that the lengths of the arms of the mannequin might not be sufficient for studying the drag value of the helmets, as with the wider time-trial helmets the flow around the shoulders and upper arms is considerably altered. Using this setup, the authors concluded that the time-trial helmets again performed more aerodynamically efficient than the road helmets, but the difference became only apparent for test velocities above 30 km h⁻¹. Moreover, the effect of adding dimples to

the time trial helmets was not measurable.

[Chowdhury et al. \(2014\)](#) carried out a wind tunnel test with four different time trial helmets of different lengths and vent geometries. Longer tails were found to be aerodynamically more efficient and the vent area, as seen from the front, should be minimized. Continuing the investigation of the effect of vents on the drag area, [Underwood et al. \(2015\)](#) manufactured a prototype helmet with twelve front and rear vent openings, which could be opened or blocked. Contrary to [Chowdhury et al. \(2014\)](#), the author of [Underwood et al. \(2015\)](#) describes the importance of vent configurations as negligible. It should be seen critical that for the latter campaign the mannequin only consisted of a model head and therefore does not accurately represent the flow, in particular, due to the lack of a torso.

In addition to the wind tunnel campaigns presented above, [Sims et al. \(2011\)](#) performed a numerical study on the length of the helmet tail. The authors used the Giro Advantage time trial helmet with a tail as a baseline and tested different truncation lengths together with trailing edge modifications. The aim of this study was to maintain the performance of the baseline helmet when the athlete is looking forward and to improve the performance when the athlete is looking down. After the initial numerical study, the best design was tested in the wind tunnel on a head model at different pitch angles. The results of both CFD and wind tunnel confirmed that the truncated helmet shape performed better when the athlete was looking down, whilst maintaining the performance for the standard head position to within 1%. Again, similar to the study of [Underwood et al. \(2015\)](#) it can be seen critical that no torso was included in the model.

A more representative numerical study was carried out by [Beaumont et al. \(2018\)](#), also focusing on helmets with different lengths at head up and head down position. The results of the simulation showed that a slightly truncated time trial helmet performs better than a long tail helmet in head up position (Figure 2.7). This is opposite to what was suggested in [Chowdhury et al. \(2014\)](#), where longer tails show improve aerodynamic efficiency. However, overall the author of [Beaumont et al. \(2018\)](#) concludes that the performance of the three helmets in head up position is nearly identical.

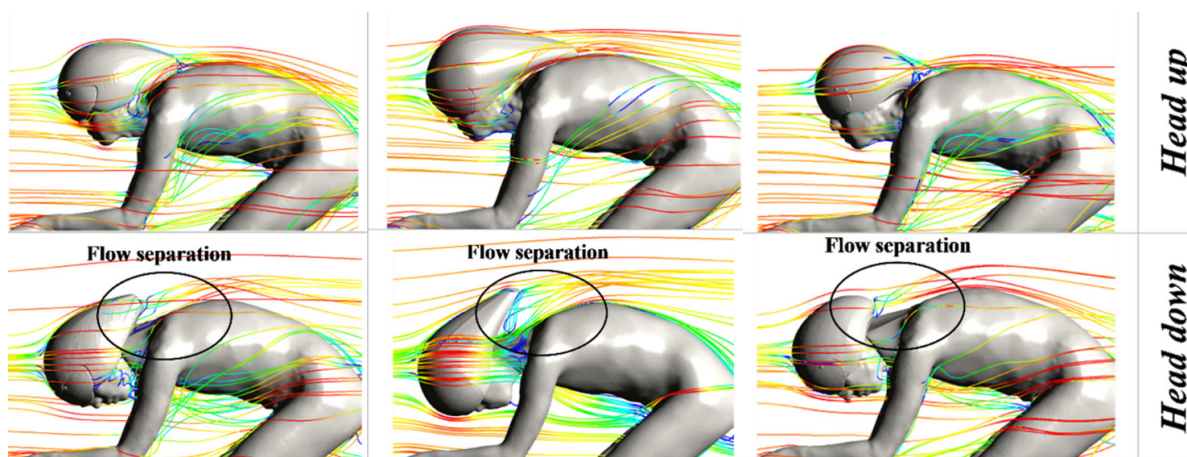


Figure 2.7: Streamline plots of three helmet configurations tested by [Beaumont et al. \(2018\)](#)

In head down position, the two truncated helmets exhibited equal drag area data and outperformed the long tail helmet. By plotting the pressure coefficient on the surface of the model the main source of drag was appointed to pressure drag, which is due to the separation of the flow at the trailing edge of the helmet.

It can be summarized that all studies report improved aerodynamic efficiency using time trial helmets over road helmets. No clear trend could be determined which shape causes the least drag, concerning vent geometry and tail length. This might be explained by the different testing conditions and models used in the presented studies. Nowadays, it is known that the most suitable helmet depends very much on the athlete's riding position and body stature and is therefore highly individual (Blair and Sidelko, 2009).

2.3. DRAG SAVINGS IN DRAFTING CONFIGURATION

When observing team time trial events in cycling the streamwise aligned configuration becomes apparent. This formation originates in the drafting effect that trailing cyclists experience following another rider, allowing them to preserve energy. In the following, relevant research about drafting in cycling is presented, starting with wind tunnel measurements, followed by field tests and numerical investigations.

2.3.1. WIND TUNNEL STUDIES ON DRAFTING

The first wind tunnel study attempting to evaluate the drafting effects has been performed by Kawamura (1953). Two 1/4 scaled model cyclist were used in racing position. Results of the drag savings experienced by the trailing cyclist range from 54 % at no wheel gap to 40 % at a separation distance of 2 m. Later, Zdravkovich et al. (1996) presented a wind tunnel test, that was conducted on full-scale cyclists in a small test section, where the speed was set to 8.2 ms^{-1} . Only the upright posture with hands on the brake hoods was tested, as can be seen in Figure 2.8. The tests covered 20 different drafting positions, not only changing the longitudinal distance between the cyclists but also the lateral.



Figure 2.8: Setup by Zdravkovich et al. (1996) in staggered arrangement



Figure 2.9: Wind tunnel test at minimum separation distance, as conducted in Barry et al. (2014a)

The results show a maximum drag reduction of the trailing cyclist of 49 %, at 0.1 m streamwise separation and at non-staggered configuration. A linear decrease of the aerodynamic benefit is observed when the gap is increased. The maximum separation distance in this test was 0.9 m, where the drag reduction amounted to 15 %. Furthermore, it can be concluded that the larger the staggered distance is, the smaller the aerodynamic benefit becomes, considering zero yaw angle of the incoming wind.

Barry et al. (2014a) set out to conduct similar tests as those of Zdravkovich et al. (1996). The test

was carried out in the wind tunnel with two full-scale models on time-trial bikes at a test velocity of 65 km h^{-1} , simulating race conditions of a team pursuit in a velodrome. A maximum drag saving of 49 % was measured for the trailing rider at minimum achievable spacing (Figure 2.9), supporting the findings of Zdravkovich et al. (1996). This configuration also resulted in a drag reduction of the leading cyclist of 5 %. At the maximum gap of 0.7 m, a 40 % drag saving could still be measured for the trailing cyclist, while for the leading cyclist the benefit reduces to 2.5 %. Compared to Zdravkovich et al. (1996) the aerodynamic benefit decreases less strong with increasing drafting distance, suggesting that also at gaps larger than 1 m a drafting effect could be experienced. The difference between the two studies can be attributed to the large blockage ratio of over 15 %, which was present in the small wind tunnel used by Zdravkovich et al. (1996). The authors of Barry et al. (2014a) also noticed that the leading rider's body size is likely to affect the drag savings of the trailing cyclist, with larger riders providing more shelter for the trailing cyclist, than smaller ones.

Continuing, Barry et al. (2015) increased the number of investigated athletes from two to four, simulating a team pursuit on time trial bikes. The wind tunnel test was conducted at a velocity of 65 km h^{-1} with a separation distance of 0.12 m between each rider (Figure 2.10). The results showed a mean drag saving of 5, 45, 55 and 57 %, for position 1, 2, 3 and 4, respectively. The authors additionally observed that drag savings found in isolated riding position also translated to drag savings in the team configuration.



Figure 2.10: Wind tunnel study with four in-line cyclists as conducted by Barry et al. (2015)

The latest wind tunnel campaign investigating drafting is presented in Belloli et al. (2016). Two full-scale cyclists on road bikes in upright position are tested at a velocity of 50 km h^{-1} . The investigated separation distance ranges from 0.05–1 m. At the smallest gap, the trailing cyclist experienced a drag reduction of 48 %, which is comparable to the results of the studies presented above. For the leading cyclist, a drag saving of 7 % was measured at this setpoint. At 1 m longitudinal separation, the benefits degrade to 38 % for the trailing cyclist, while the front rider does not experience any drag reduction. The authors also investigated the effect of side winds by introducing a yaw angle between the pair of cyclists and the incoming wind. Here, the results show a decrease of drag savings with increasing magnitude of the side wind angle. In this study, no staggered arrangements were tested, which is commonly employed in cycling when encountering side wind conditions.

2.3.2. ON-SITE STUDIES ON DRAFTING

The first field study dedicated to drafting effects in cycling was carried out by (Kyle, 1979). A coast-down test was envisioned in a 200 m long enclosed hallway. The campaign included measurements with 1–4 cyclists, estimating their aerodynamic drag by the rate of deceleration. At a separation gap between the two cyclists of 0.3 m, the results showed a drag decrease of 38 % independent of the test velocities, which were between $24\text{--}56 \text{ km h}^{-1}$. No benefit for the leading cyclist was observed. The

author also noticed a reduced drag saving for staggered formations compared to tests with equal streamwise spacing but no offset, confirming the findings of [Zdravkovich et al. \(1996\)](#). Additionally, it was established that larger body sizes of the leading cyclist result in larger drag benefits for the trailing rider. Interestingly, [Olds et al. \(1995\)](#) uses these data to conclude that there is no drafting effect at a wheel spacing of more than 3 m. This statement can be seen as highly critical as even though this spacing was not tested by [Kyle \(1979\)](#), extrapolating the existent data would not suggest this behaviour.

[Edwards et al. \(2007\)](#) conducted further on-site drafting measurements, with athletes of different physical stature. The test subjects were asked to ride an outdoor 200 m flat segment from both directions at a constant velocity of 45 km h^{-1} and maintain a certain posture. The investigated drafting distance was 0.5 m with no lateral offset. The power output of the athletes was measured by a hub based power meter, which was utilized to extract the aerodynamic resistance from each test. The main result of this research is that the leading athlete with the largest drag area also provided the largest drag saving for the trailing cyclists (49.4 %), underlining the findings of [Barry et al. \(2014a\)](#). The mean drag reduction for the trailing cyclist behind the intermediate and small-sized athlete was 41.8 % and 35.4 %, respectively. Moreover, no clear conclusion could be drawn whether the drafting arrangement would benefit the leading cyclist. Ambient wind direction and speed were measured for each test, however, the results will be affected by local wind behaviour. Additionally, it can be argued that the drafting distance of 0.5 m was not kept constant throughout the test.

[Broker et al. \(1999\)](#) describe an outdoor velodrome test carried out with four cyclists riding as close to each other as feasible. The power output from each rider was measured with an SRM crank-sprocket power meter. Race conditions of a team pursuit were simulated at a target velocity of $57\text{--}61 \text{ km h}^{-1}$. The study showed that the second, third and fourth rider in the arrangement saves 29.2, 35.9 and 36 %, respectively, of the leading cyclist's power. As seen in previous studies, the authors conclude that the size and posture of the leading rider has a big influence on the drag savings of the trailing cyclists. Some of the gathered data were compromised due to increased spacing between the riders.

Recently, [Fitton et al. \(2017\)](#) conducted a similar study to the one from [Broker et al. \(1999\)](#). Once again, evaluating the correlation between the physical characteristics of athletes and their drag savings when riding at different positions in a team pursuit. For this, a mathematical model was created, which uses power meter data and the geometry of the velodrome as input data. Four professional female athletes were then asked to ride once individually and once in close proximity to each other, at a velocity of 50 km h^{-1} . Here, similar results were obtained as in [Broker et al. \(1999\)](#), where the largest drag benefits were assigned to athlete 3 and 4, albeit slightly higher in magnitude. During the test, the authors describe that due to the continuous circulation an artificial tailwind develops in the hall. Similar to the aforementioned studies, it was concluded that the size and the mass of the riders are correlating criteria with the drag area value of the athlete.

2.3.3. NUMERICAL STUDIES ON DRAFTING

An early numerical study on the subject of drafting in cycling is presented in [Torre et al. \(2009\)](#). Due to the complexity and cost of 3D fluid dynamic simulations, the authors decided to investigate the effect using a two-dimensional solver. The bike and rider system was modelled using a simplified elliptic shape, which was tweaked to match experimental data of cyclists to within 5 %. The velocity in the simulation was set to 15 ms^{-1} with a separation gap of 0.2 m. The results confirmed a drag reduction of the leading cyclist by 5 %, as previous studies indicate. However, the drag saving of the trailing cyclist is lower than in comparative literature, namely only 26 %. Due to the simple setup of

the simulation, the authors tested a group of up to nine riders. Here, the riders in position two to nine experience a drag benefit in the range of 32–34 %. Nowadays, it is known that complex vortical structures play an important role in the flow around the cyclist and therefore this study, albeit providing a trend, cannot reproduce the correct magnitude of drag savings during drafting.

A more representative analysis was performed by [Blocken et al. \(2012\)](#), where 3D laser scanned models were imported into the solver, which represent both the dropped position on a race bike and the time trial position. One of the main goals of this research was to compare RANS (a time-average approach) to LES (time-resolved approach). The velocity in the simulation was chosen to be 15 ms^{-1} . The separation distance was tested in the range of 0–1 m, resulting in drag savings for the trailing cyclist in time trial position of 37–29 % for LES and 17–13 % for RANS. Both simulations showed a linear decrease for increasing wheel gap, as already indicated by [Zdravkovich et al. \(1996\)](#). Additionally, a maximum benefit of 3 % was observed for the leading cyclist at no separation distance. It can be concluded, that the choice of solver plays a critical role in the results of the simulation, as large discrepancies between RANS and LES were found. It is important to add that surface details of the scanned model were removed and no bicycle was included in the simulation. The tested geometry is therefore not fully representing reality.

In a further study [Blocken et al. \(2013\)](#) attempt to explain the cause of drag reduction for both the leading and trailing cyclist. The same rider-only model as in [Blocken et al. \(2012\)](#) is used and duplicated for drafting studies. Zero roughness was applied to the cyclist's surface, which can be seen critical as hair and suits do not provide a smooth surface. At minimum separation distance, the numerical results show the largest drag reduction for the trailing cyclist in upright position and the smallest for the time trial position, with 27 % and 14 %, respectively. The draft benefits again show a linear decay for all three positions at increased drafting distance. At 1 m a drag benefit of 12 % for the trailing cyclist in time trial position is reported. Looking at [Figure 2.11](#), the region with low pressure behind the isolated cyclist is weakened by the upstream pressure propagation of the drafting cyclist. This high-pressure region extends further forward in time-trial position than in upright position, explaining why the leading cyclist experiences the largest drag reduction in time-trial position. Concerning the trailing cyclist, the high-pressure region in front is reduced, while the authors also state a smaller low-pressure region on the back of the trailing cyclist ([Figure 2.12](#)).

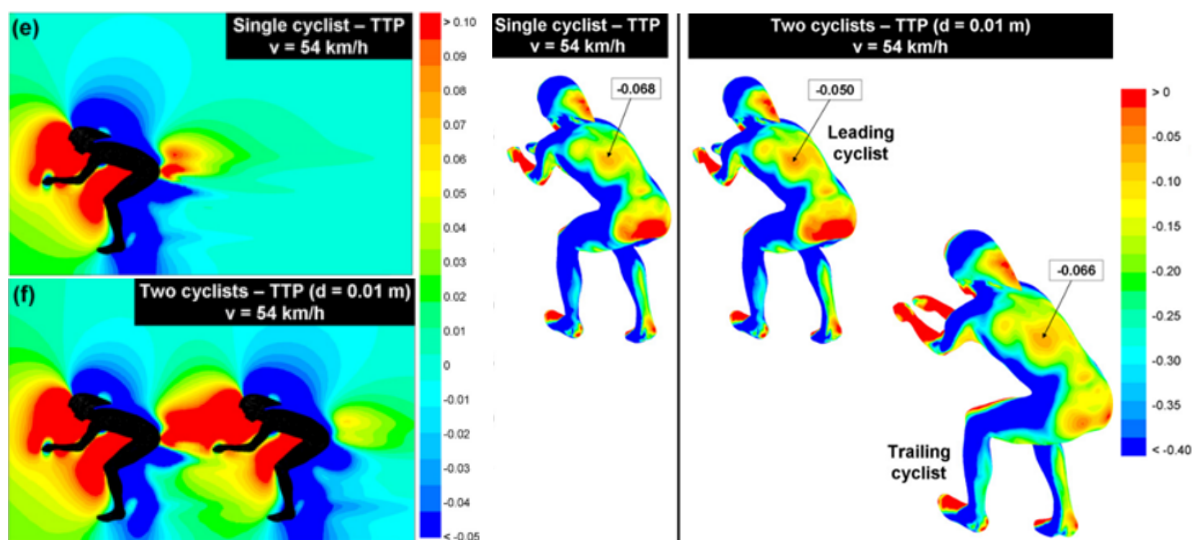


Figure 2.11: Pressure interaction between two drafting cyclists ([Blocken et al., 2013](#))

Figure 2.12: Pressure distribution on cyclists as presented in [Blocken et al. \(2013\)](#)

In [Defraeye et al. \(2013\)](#) the authors conducted a numerical study on the cyclist's drag in a team pursuit, by scanning four male athletes and importing their geometry into the simulation. Similar to [Blocken et al. \(2012\)](#) and [Blocken et al. \(2013\)](#), the bicycle was not included in the model in order to reduce computational costs. The CFD simulation used a steady RANS approach, while the drafting gap was assumed to be quasi-zero and the velocity was set to 60 km h^{-1} . As already described in [Blocken et al. \(2013\)](#), the surface of the cyclist was modelled with zero-roughness. However, the author acknowledges that increased surface roughness may have a positive effect on the drag values of the cyclist. The results confirm the findings of previous studies, where the leading cyclist experiences a drag reduction of 3 %, while the trailing cyclists encounter a drag benefit of up to 40 %.

In a recent non-peer reviewed study, the bike wheel manufacturer, SwissSide, has investigated the effect of drafting at larger distances. As mentioned above, the regulations in non-drafting races state that a minimum distance of 12 m between front wheel and front wheel must be maintained [Ironman \(2018\)](#). The study was conducted at 45 km h^{-1} , which is the common race velocity in long-distance triathlons. The results are in line with previous studies, estimating the drag saving of the trailing cyclist at minimum separation distance to 39.5 % (Figure 2.13). Furthermore, it is shown that at 10 m wheel-to-wheel gap the drafting effect is still measurable for the trailing cyclist. A clear velocity deficit can be observed in Figure 2.14 upstream of the second rider, leading to a drag reduction of 13.4 %. The results even show a small drag benefit of 8.9 % at a distance of 20 m trailing the leading cyclist. These results contradict the statement of [Olds et al. \(1995\)](#), where the author suggested negligible drafting effect at wheel gaps larger than 3 m.

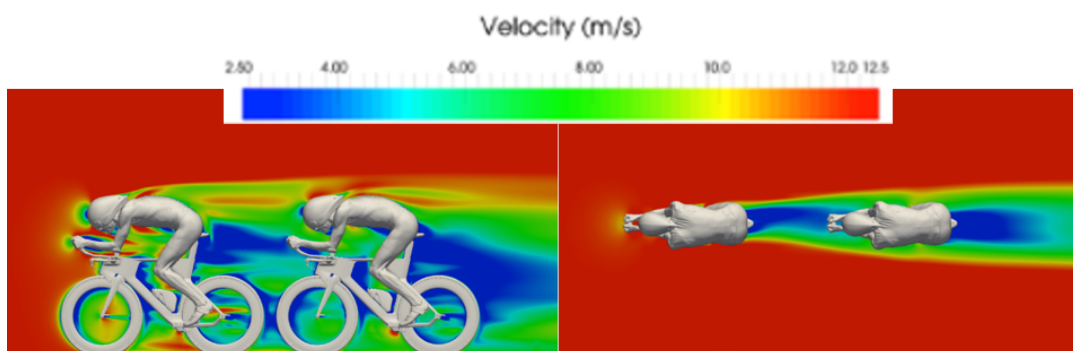


Figure 2.13: Velocity plot at 0.1 m wheel gap as simulated by [SwissSide \(2017\)](#)

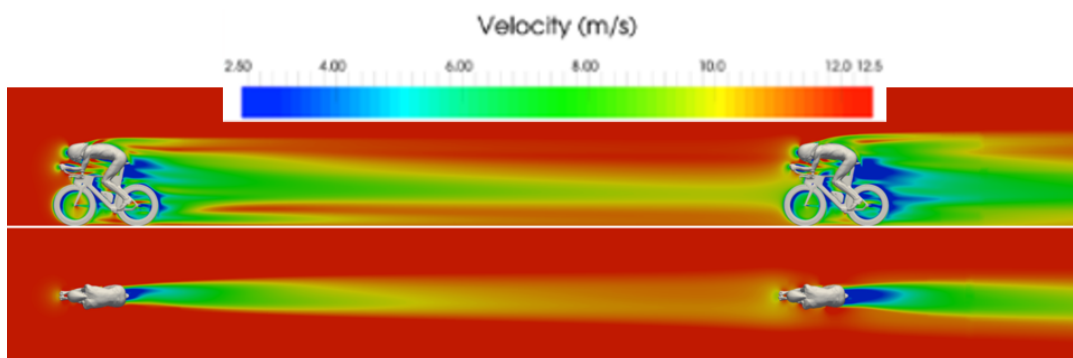


Figure 2.14: Velocity plot at 10 m wheel gap as simulated by [SwissSide \(2017\)](#)

The results of all presented studies are summarized in table 2.1. Here, the gap is defined as the distance between the rear wheel of the lead cyclist and the front wheel of the trailing cyclist.

Table 2.1: Summary of drafting studies

Article	Method	Velocity [kmh^{-1}]	Gap [m]	Pos.	Drag reduction by rider [%]			
					# 1	# 2	# 3	# 4
Kawamura (1953)	Wind tunnel	N/A	0	D ¹	-	54	-	-
			2			40		
Kyle (1979)	Coastdown		0.3	D	0	38	-	-
			40			38		
			56			38		
			40			29		
Zdravkovich et al. (1996)	Wind tunnel	29.5	0.1	UP ²	0	49	-	-
			0.9			15		
Broker et al. (1999)	Velodrome	57-61	<0.3	TT ³	-	29.2	35.9	36
Edwards et al. (2007)	Field test	45	0.5	D	0	35.4-49.4	-	-
Torre et al. (2009)	CFD	54	0.2	-	4	26	-	-
	CFD (RANS)				4	31	32	30
Blocken et al. (2012)	CFD (LES)	54	0	TT	0	13	-	-
			1		2	36		
			0		0	30		
Defraeye et al. (2013)	CFD (RANS)	60	0	TT	3	40	40	40
			0	UP	0.8	14		
			1		0.5	12		
Blocken et al. (2013)	CFD (RANS)	54	0	D	1.7	23	-	-
			1		0.4	21		
			0	TT	2.7	27		
			1		0.6	25		
Barry et al. (2014a)	Wind tunnel	65	0	TT	5	49	-	-
			0.8		3	45		
Barry et al. (2015)	Wind tunnel	65	0.12	TT	5	45	55	57
Belloli et al. (2016)	Wind tunnel	50	0.1	UP	7	47	-	-
			1		0	38		
			0.1		4.4	39.5		
			5		0.4	20.3		
Swissside (2017)	CFD	45	10	TT	0	13.4	-	-
			15		0	10.6		
			20		0	8.9		
Fitton et al. (2017)	Velodrome	50	<0.3	TT	4	42	48	47

¹ Drops² Upright³ Time-trial

The aforementioned studies can be summarized by a measurable drag saving for the trailing cyclist at small separation distances of less than 3 m. A trend towards a linear decreasing drag benefit at increasing separation distance has been observed. At close drafting configuration, multiple authors also report a positive effect on the lead cyclist. No academic investigations have been found concerning a drafting distance beyond 3 m. However, a non-peer reviewed article suggests drag savings for the trailing cyclist at a separation gap of up to 20 m. Numerous studies have confirmed that the drafting effects are strongly related to the physical appearance of the riders involved.

2.4. FLOW TOPOLOGY BEHIND CYCLIST IN TIME-TRIAL POSITION

In recent years an increasing effort was made to conduct flow field measurements in the wake of a cyclist and to indicate the main vortical structures. In the following, first, the wake topology behind an individual cyclist is presented before moving on the drafting case. To conclude this chapter relevant literature is presented discussing the potential dominant structures in the far wake.

2.4.1. WAKE TOPOLOGY OF INDIVIDUAL CYCLIST

An early study by [Crouch et al. \(2014\)](#) investigated the flow topology in the upper wake at different crank angle positions. Multiple streamwise vortices downstream of the cyclist were observed, whose strength and position showed a dependency on the leg position. For the asymmetric scenario, with the pedals in vertical alignment, this statement is confirmed by a tomographic PIV study conducted by [Jux et al. \(2018\)](#), in which distinct vortex structures could be extracted, as visualized in [Figure 2.15](#).

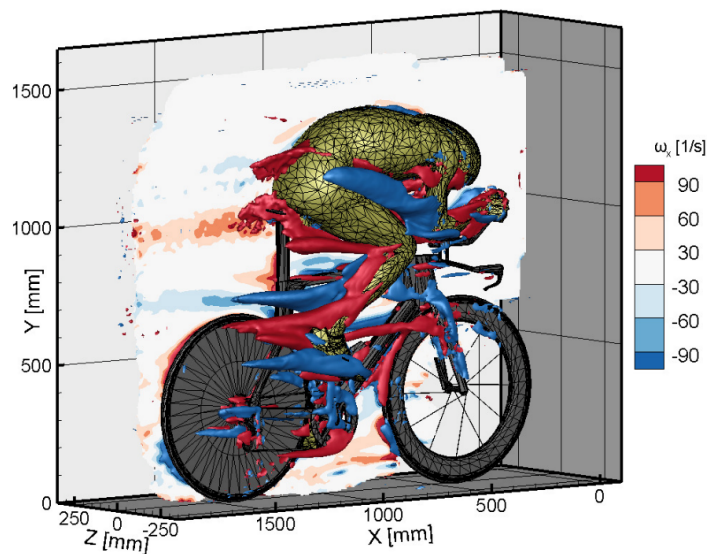
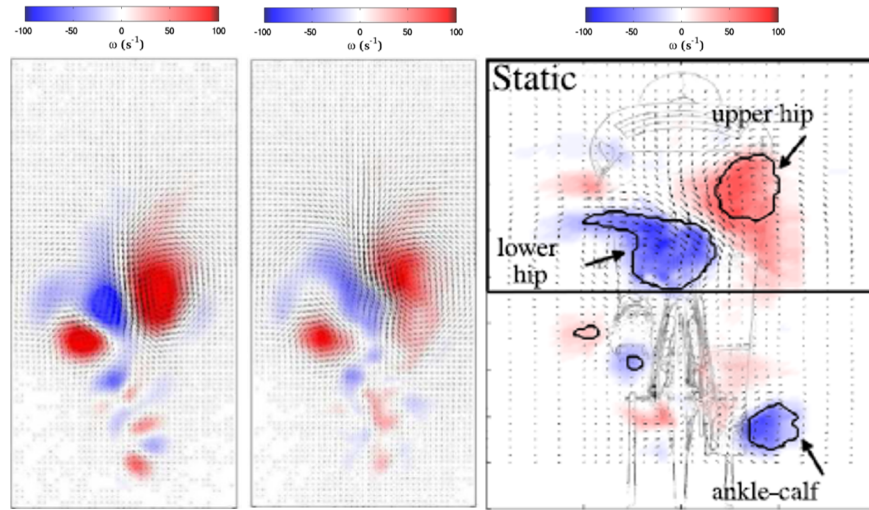


Figure 2.15: Streamwise isosurface vorticity plot as created by [Jux et al. \(2018\)](#) based on a wind tunnel experiment

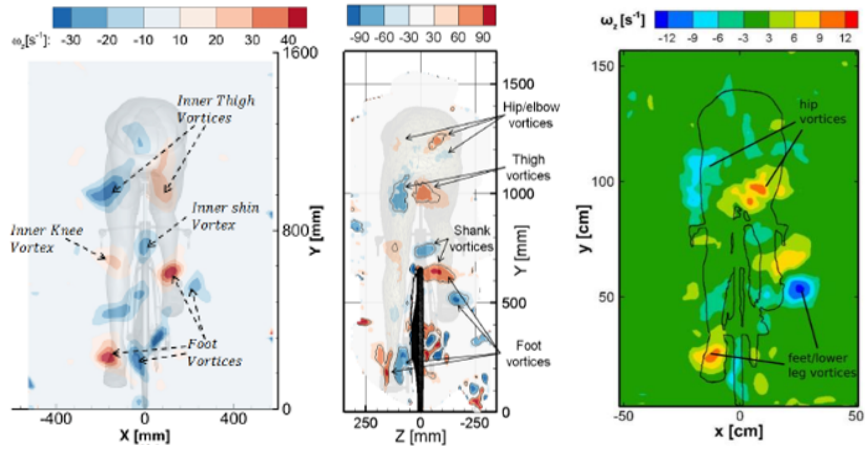
To continue the research of [Crouch et al. \(2014\)](#), [Crouch et al. \(2016a\)](#) expanded the dimensions of the measurement plane in vertical direction to capture the entire wake field behind the cyclist. From this study, the authors concluded, that the differences in wake topology between a static pedal position and its phase-averaged dynamic pedalling counterpart, are marginal, regardless of the pedalling frequency. This observation is supported by the results of the previous Ring of Fire campaign, performed by [de Martino Norante \(2018\)](#), in which only the magnitude of the vorticity showed a deviating value, explained by a different Reynolds number regime between the tests.

An initial attempt was made by [Crouch et al. \(2016a\)](#) and [Griffith et al. \(2014\)](#) to characterize the

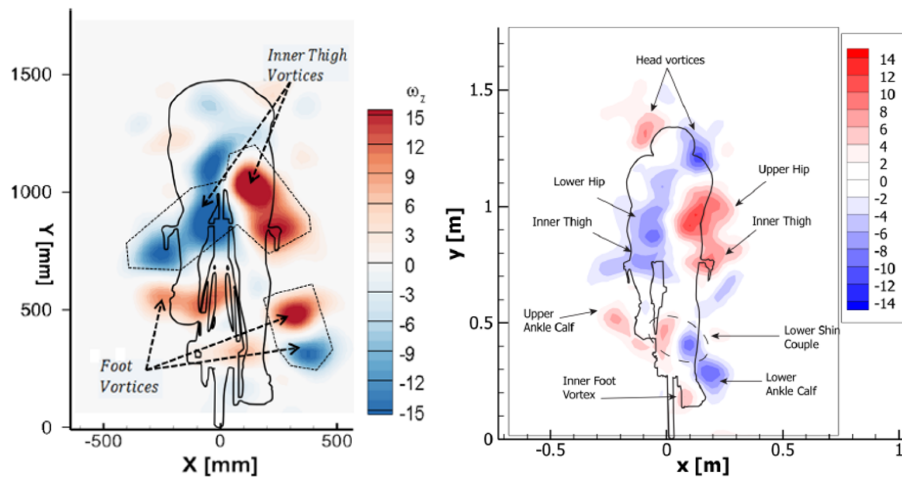
primary vortical structures in the wake of the cyclist. The origin of the dominating counter-rotating vortex pair was assigned to the hip/thigh region of the cyclist. Subsequent, wind tunnel PIV measurements, acquired in the wake of a 3D printed cycling mannequin in asymmetric pedal position showed reoccurring structures, with the most prominent being the hip/thigh and foot vortices (Terra et al. (2016), Shah (2017) and Jux et al. (2018)). Moreover, from the previous two Ring of Fire experiments by Spoelstra (2017) and de Martino Norante (2018) asymmetric phase-locked vorticity fields were obtained, which showed a more pronounced hip/thigh vortex pair, likely due to the different posture when compared to the mannequin used in the aforementioned wind tunnel studies. Again, vortical structures originating from the foot region can be identified. The most recent Ring of Fire campaign furthermore depicted a counter-rotating head vortex pair, which has not been observed in preceding studies. The resultant vorticity plots behind a single rider from all previously mentioned works are presented in Figure 2.16. Here, images 2.16d through 2.16f are conducted with the same mannequin, equal to the one illustrated in Figure 2.15.



(a) Numerical steady-state (Griffith et al., 2014) (b) Numerical transient (Griffith et al., 2014) (c) Wind tunnel (Crouch et al., 2016a)



(d) Wind tunnel (Shah, 2017) (e) Wind tunnel (Jux et al., 2018) (f) Wind tunnel (Terra et al., 2016)



(g) Ring of Fire (Spoelstra et al., 2018) (h) Ring of Fire (de Martino Norante, 2018)

Figure 2.16: Labelled streamwise vorticity plots behind individual cyclist

2.4.2. WAKE TOPOLOGY OF TRAILING CYCLIST

In order to study the flow field around a trailing cyclist, [Barry et al. \(2016a\)](#) tested two scaled cyclists in a water channel, as shown in Figure 2.17. The authors acknowledge a reduced Reynolds number by an order of magnitude compared to the real condition. An increased rate of diffusion of the streamwise vortex structures is assumed and therefore suggests that this configuration is more representative for larger separation distances than were tested in this paper. [Crouch et al. \(2016b\)](#) found that primary vortex structures observed in the scaled water channel test show good agreement with the full-size wind tunnel campaign, confirming that the test by [Barry et al. \(2016a\)](#) is representative. The flow field around the cyclist was captured with a planar PIV setup to acquire time-averaged data. The selected measurement planes are depicted in Figure 2.18.

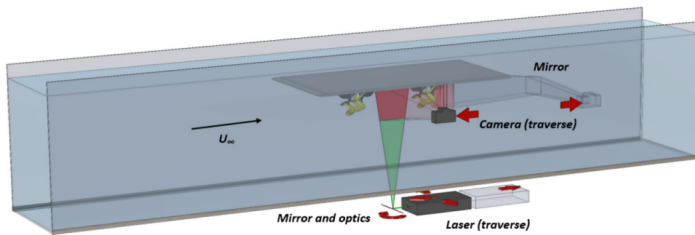


Figure 2.17: Water tunnel setup by [Barry et al. \(2016a\)](#) using a single PIV measurement plane.

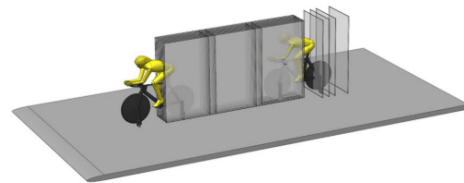


Figure 2.18: 8 PIV measurement planes in front and behind the trailing cyclist as used in [Barry et al. \(2016a\)](#).

Two separation distances were investigated, namely 1/11 of a bike length and one bike length, when translated into full scale. The results of the study are presented in Figure 2.19a to 2.19c, showing the leading and trailing cyclist both in asymmetric leg position.

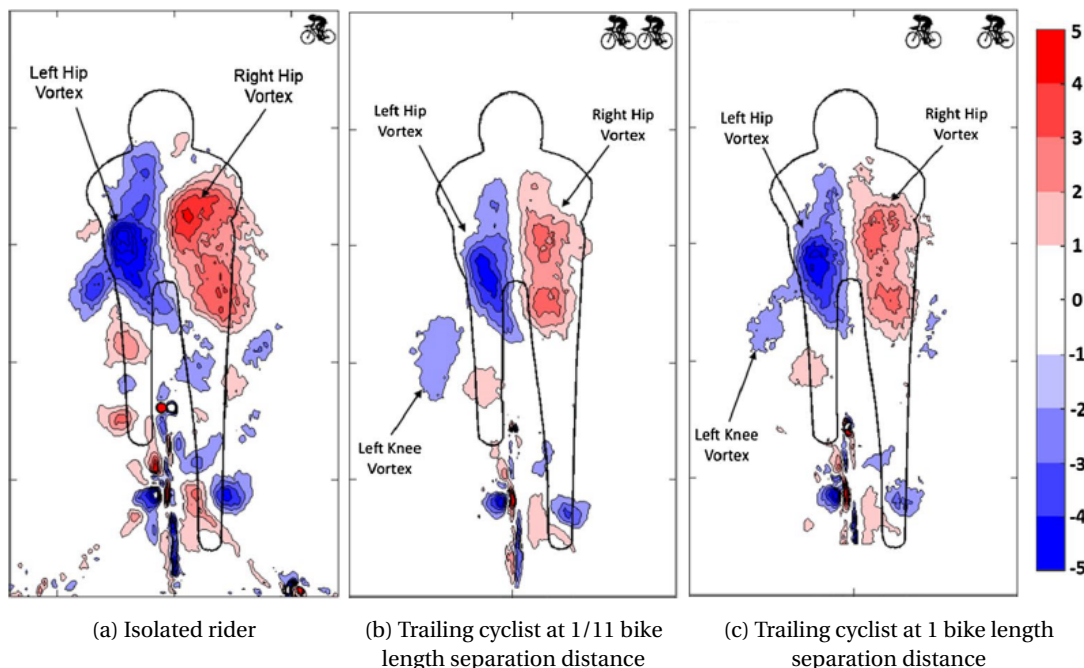


Figure 2.19: Streamwise vorticity behind rider in asymmetric position ([Barry et al., 2016a](#)).

The authors concluded that the main wake structures stemming from the trailing cyclist are comparable to those from an isolated rider, despite the significant upstream disturbance. It should be added that the strength of the upper hip vortex structures is slightly weakened, explained by the

authors due to the reduced energy in the flow faced by the trailing rider. Streamwise vortical structures in the foot region are consistent, although weaker. Additionally, the findings of [Blocken et al. \(2013\)](#) are supported in that the majority of the drag benefit for the trailing cyclist originates from decreased stagnation pressure, due to the presence of the leading cyclist. For this, [Barry et al. \(2016a\)](#) plotted the streamwise velocity contours just upstream of the trailing cyclist. A clear velocity deficit can be identified for the small separation distance. A less pronounced deficit is observed at one bike length behind the leading cyclist as depicted in Figure 2.20.

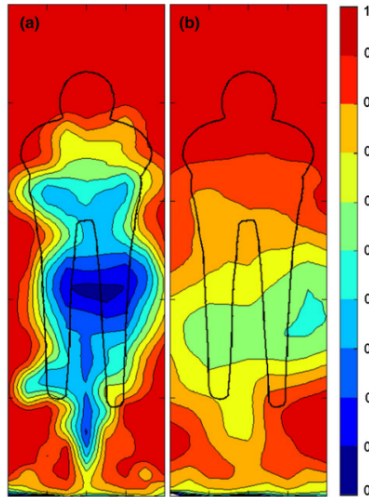


Figure 2.20: Streamwise velocity upstream of trailing cyclist at gap of $1/11$ (left) and 1 (right) bike length ([Barry et al., 2016a](#))

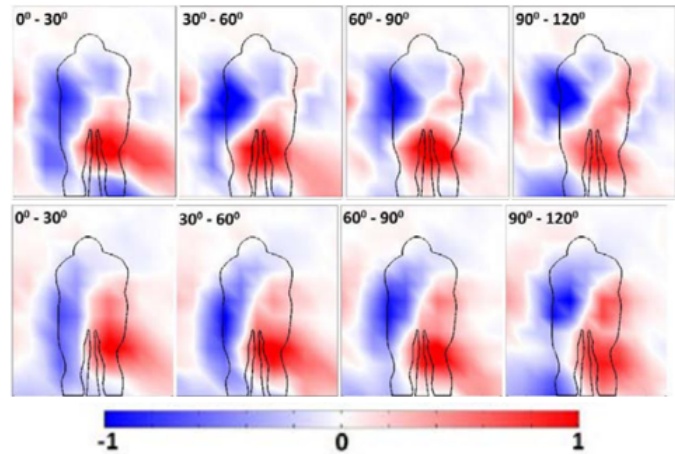


Figure 2.21: Phase-averaged streamwise vorticity plots by [Barry et al. \(2016b\)](#). Upper row isolated rider, lower row trailing cyclist

Following the water tunnel test, [Barry et al. \(2016b\)](#) conducted a wind tunnel study, again with the intention of comparing the wake topologies between isolated and trailing cyclist. The test was carried out with full-scale riders in dynamic pedalling configuration. Similar to [Barry et al. \(2016a\)](#), the main vortical structures, in particular, the hip vortices are consistent between the isolated and trailing case, although the streamwise vorticity is weakened in magnitude. In Figure 2.21, phase-averaged streamwise vorticity plots can be obtained comparing the wake structures of an isolated rider to those of a trailing cyclist in tandem configuration with a separation distance of approximately 0.2 m. The author concludes that the drag savings of the trailing cyclist do not originate in a change of wake structures. Lastly, the authors provided normalized streamwise velocity plots just downstream of the isolated and trailing cyclist, which are given in Figure 2.22a and 2.22b, respectively.

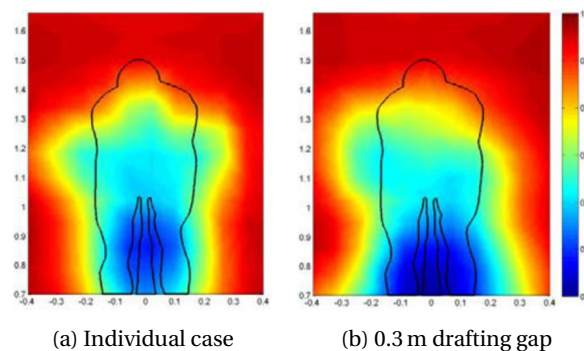


Figure 2.22: Time-averaged normalized streamwise velocity behind cyclist ([Barry et al., 2016b](#))

Similar to the primary flow structures, the velocity deficit contour in the near wake region behind a trailing cyclist resembles the individual rider case, albeit the peak velocity deficit and width of the lower wake are slightly more pronounced in the drafting case.

2.4.3. WAKE BEHAVIOUR FAR DOWNSTREAM

Considering drafting cases at larger separation distances, the downstream evolution of the lead cyclist's wake is of importance, as it represents the flow field encountered by the trailing cyclist. The previous two Ring of Fire studies provide flow field information in the far wake region, which are shown in Figure 2.23b and 2.23d. In both results, the lower wake broadens in downstream direction, with the peak velocity deficit being concentrated in the lower portion of the wake itself. The upper wake region does not diffuse in width but stays rather narrow.

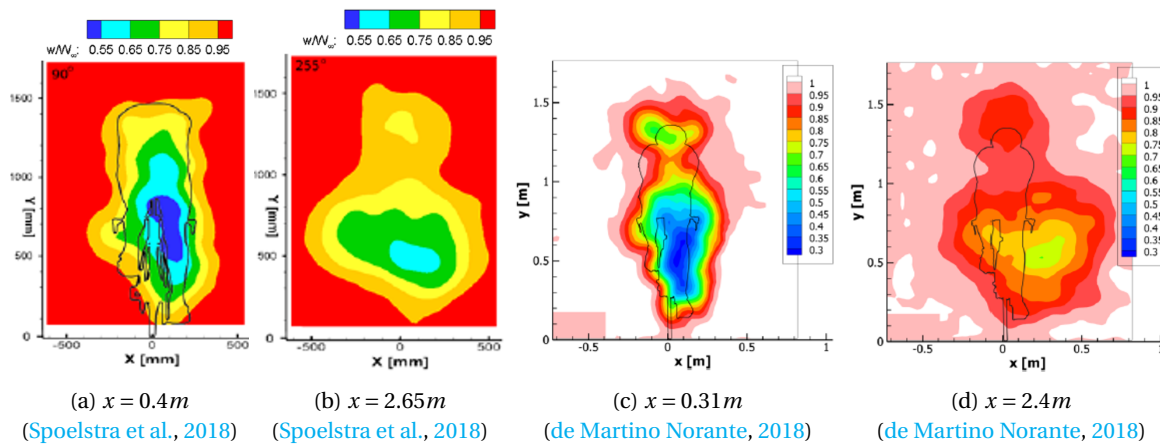


Figure 2.23: Normalized streamwise velocity plots at distance x behind cyclist obtained from Ring of Fire measurements

From the previously investigated literature the hip/thigh couple can be considered as being the most dominant vortex pair in the wake of a cyclist, as illustrated by Figure 2.24. It can be expected that these structure outlast the smaller-scale features from the lower portion of the wake. This trend is shown in Figure 2.25, extracted from the initial Ring of Fire study by Spoelstra (2017), where the counter-rotating vortices from the hip/thigh region are still identifiable 3.025 m downstream of the cyclist.

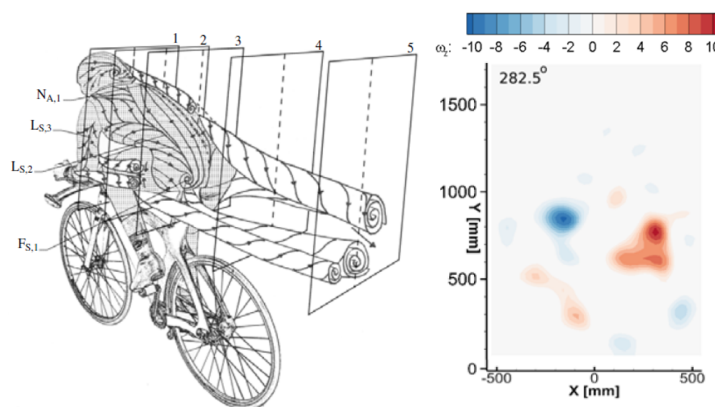


Figure 2.24: Asymmetric flow topology in the wake (Crouch et al., 2017)

Figure 2.25: Streamwise vorticity at 3.025 m behind cyclist (Spoelstra, 2017)

2.5. OBJECTIVE AND RELEVANCE OF THIS THESIS

In the works of Spoelstra (2017) and de Martino Norante (2018), the Ring of Fire system has previously shown great potential in analysing the flow field around a transiting cyclist. Particularly strong agreement to literature was found concerning the flow topology in the near wake. To evaluate the accuracy of the drag area value, Spoelstra (2017) conducted a reference wind tunnel study in which a before and after correction a 30 % and 10 % discrepancy to the Ring of Fire method was obtained. To further assess the accuracy of the Ring of Fire system, this thesis intends to compare the resultant drag area values from the Ring of Fire approach to simultaneously acquired power meter data, which allows the formulation of the research objective as follows:

"Assessment of the Ring of Fire system for cycling aerodynamics by simultaneous state-of-the-art power meter measurement techniques"

A successful outcome of the experiment would show good agreement between the drag results from the two approaches and would attest to the Ring of Fire's viability as measurement technique for cycling aerodynamics. As part of the campaign, a long distance drafting beyond 3 m is envisaged, as no academic research has been performed in this regime, to the best author's knowledge and belief. Based on the background provided in chapter 1, the drag savings in non-drafting races, such as long-distance triathlon could be quantified and flow structures responsible for the downstream wake behaviour could be identified.

2.6. OUTLINE OF THIS REPORT

Following the preceding introductory text in chapter 1, the current chapter chapter 2 presented a literature review, concerning the Ring of Fire measurement technique, aerodynamic drag measurements on different helmet types, as well as aerodynamic benefits and flow topology changes under drafting condition. The subsequent chapter 3, introduces the employed model to extract drag area values from the power meter recordings, before the working principles of the PIV technique are presented, with particular emphasis on stereo-PIV setups. The theoretical framework chapter concludes with the concept of the control volume approach. Chapter 4 informs the reader about the experimental installation used for the measurement campaign, describing the test facility, the Ring of Fire setup, the test object and the chosen acquisition settings. Thereupon, chapter 5 focuses on the data reduction processes employed for both power meter and Ring of Fire data. The processed data are then used in chapter 6 to compare the two measurement techniques against each other and to discuss flow field changes around the trailing cyclist in drafting condition. A final conclusion concerning the previous findings, as well as recommendations for future Ring of Fire experiments are given in chapter 7. Supplementary information about an encountered seeding problematic can be found in Appendix A. A sample code of the applied wake contouring algorithm is provided in Appendix B.

3

THEORETICAL FRAMEWORK

The subsequent chapter examines the underlying principles used to evaluate the cyclist's drag through power meter and PIV techniques. First, section 3.1 introduces the individual drag components that must be overcome by the cyclist. Second, models and empirical formulas are provided, that allow the determination of the aerodynamic drag from the power meter data (section 3.2). Third, section 3.3 explains the working principle of PIV, with particular emphasis on a stereoscopic configuration, before presenting the control volume approach used to extract the aerodynamic drag from the PIV measurements in section 3.4.

3.1. RESISTIVE FORCES DURING CYCLING

Cyclists expend their energy to overcome resistive forces that oppose their forward motion, comprising rolling and gradient resistance, friction forces in drivetrain and bearings components, bump losses and finally the aerodynamic drag. A constant velocity is maintained when the cyclist's power output equals the sum of all opposing forces times the rider's velocity. During acceleration and deceleration, inertial effects play an additional role. A schematic, shown in Figure 3.1, highlights the origin of the drag components encountered during cycling.

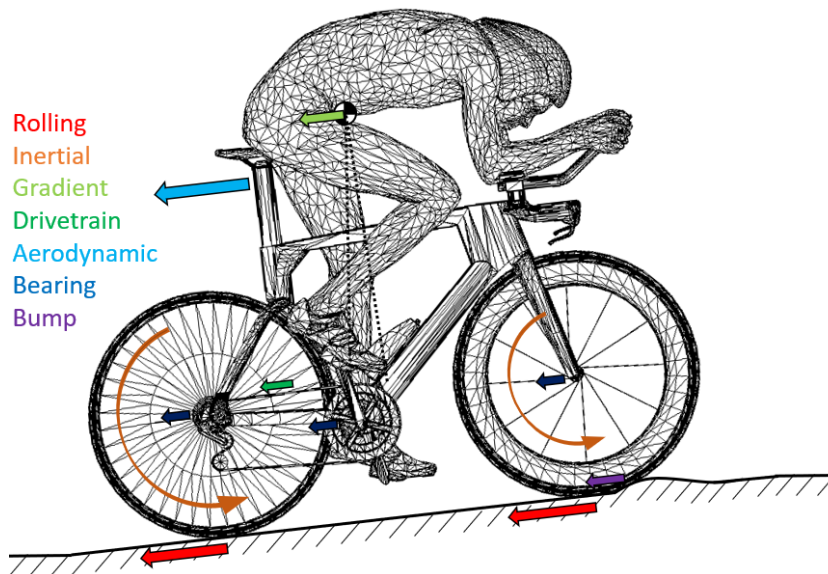


Figure 3.1: Schematic representation of opposing forces during cycling

The experiment in the framework of this project aims at a constant velocity of the cyclist riding over a level surface with minimum undulations and thus inertial effects, bump losses and gradient resistance can be neglected. Of the remaining forces, the aerodynamic drag dominates at velocities beyond 15 km h^{-1} , as established by [Kyle et al. \(2004\)](#) and contributes to 90 % at race velocities around 45 km h^{-1} ([Kyle et al., 1984](#)), of which 60–80 % can be attributed to the cyclist him/herself ([Defraeye et al. \(2013\)](#), [Blocken et al. \(2013\)](#) and [Crouch et al. \(2017\)](#)). While the aerodynamic resistance increases with the square of velocity, rolling resistance can be considered independent from speed, as stated in [Grappe et al. \(1997\)](#). Empirical expressions for the drivetrain and bearing losses are given in section 3.2 and together account for less than 5 % of the total resistance in racing conditions, according to [Wilson et al. \(2004\)](#).

3.2. DRAG AREA EVALUATION THROUGH POWER METER

This master's thesis objective is the validation of the Ring of Fire system with simultaneously acquired measurements with a state-of-the-art power meter device. A wide range of power meter types exist, with common mounting locations being the pedals, cranks, spider, bottom bracket and the hub of the rear wheel. Each system offers advantages and disadvantages, in terms of cost, durability, accessibility and most important accuracy. The torque, resulting from the rider's force on the pedal, causes material deformations, which are measured by one or multiple strain gauges packaged in the power meter. Together with the angular velocity, which is either measured by accelerometers or magnetic sensors, the power output of the cyclist can be determined.

Throughout one crank cycle, the applied torque varies strongly, due to biomechanical properties of the rider ([Quintana-Duque et al., 2015](#)). In order to extract meaningful information, the power meter averages the acquired data over one crank cycle.

The recorded power data, P_{total} , can be utilized to obtain the total drag force D_{total} , opposing the rider's motion, through the basic relation:

$$P_{total} = D_{total} \cdot V \rightarrow D_{total} = \frac{P_{total}}{V} \quad (3.1)$$

, where V is the cyclist's velocity and D_{total} comprises of:

$$D_{total} = D_{aero} + D_{rolling} + D_{drivetrain} + D_{bearing} \quad (3.2)$$

The aerodynamic drag must be extracted from equation 3.2, in order to compare the aerodynamic drag value to the results of the Ring of Fire technique. It is therefore required to first determine the remaining terms, through models, empirical values and data fitting.

- **Wheel bearing resistance** Measurements on wheel bearing losses were conducted by [Dahn et al. \(1991\)](#). Based on these data [Martin et al. \(1998\)](#) formulated a numerical model to express the wheel bearing losses in each wheel as a function of velocity:

$$D_{bearing} = (91 + 8.7V) \cdot 10^{-3} \quad (3.3)$$

Losses within the bearing components can be expected to account for less than 2 % of the overall drag force.

- **Drivetrain resistance** The drivetrain efficiency comprises friction losses within the chain and at the interface with the front chainring and rear sprocket. Throughout studies by [Spicer et al. \(2000\)](#), [Kyle et al. \(2001\)](#), [Rohloff et al. \(2004\)](#) as well as [Hinzen et al. \(2012\)](#) it is consistent that transmission efficiency increase with larger power output. Ultimately, the data from the most recent study by [Hinzen et al. \(2012\)](#) are utilized to quantify the chain drive resistance, as the

study investigates power outputs as low as 50–200 W and are thus representative of the test regime of the current experiment. Furthermore, the author claims to measure the drivetrain efficiency at per mille accuracy. The discrete results are linearly interpolated and plotted in Figure 3.2, which displays the drivetrain efficiency as a function of the transmitted power and the selected gear (number of chainring teeth and number of sprocket teeth).

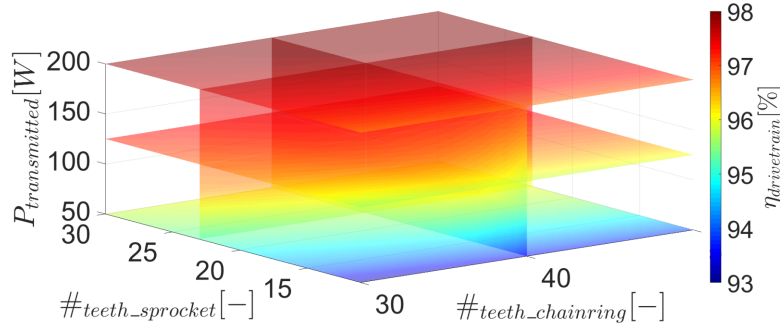


Figure 3.2: Interpolated drivetrain efficiency, based on measurements conducted in [Hinzen et al. \(2012\)](#)

- **Rolling resistance** The rolling resistance is dependent on the tyre-pressure, -loading, -diameter and -temperature, as well as the surface properties of the ground and the steering conditions ([Burke, 2003](#)). In automotive engineering, the rolling coefficient, C_{rr} , is also a function of velocity. However, [Grappe et al. \(1997\)](#) and [Baldissera et al. \(2017\)](#) regard the effect of speed on the rolling coefficient in cycling as negligible and therefore use a speed-invariant C_{rr} value. A wide range of rolling coefficient values are documented in literature based on bicycle tyre and surface properties, mostly ranging between 0.0017–0.0043 for high-performance tyres on concrete ([Kyle et al. \(1985\)](#) and [Lafford \(2000\)](#)). For low inflation pressures this rolling resistance coefficient increases up to 0.005–0.006 at 5 bar, according to [Grappe et al. \(1999\)](#) and [Wilson et al. \(2004\)](#). In the current experiment, an attempt is made to evaluate the C_{rr} value under local test conditions, using a linear regression method, based on [Debraux et al. \(2011\)](#), where only the aerodynamic drag and the rolling drag are considered. To obtain the C_{rr} data, the cyclist conducts tests at different velocities while maintaining a constant posture on the bike. The power output at the different speeds is recorded with a power meter and thus allows the extraction of the total resistive drag force. [Debraux et al. \(2011\)](#) assume a linear relationship between the total resistive force and the squared velocity, since the rolling resistance is velocity invariant, as established above and the aerodynamic drag scales with the velocity squared as defined by:

$$D_{aero} = \frac{1}{2} \rho C_d A V_{rel}^2 \quad (3.4)$$

Here, ρ is the air density, C_d the drag coefficient, A the frontal area and V_{rel} is the relative velocity between the cyclist and the surrounding air. A linear regression can then be performed, as shown in Figure 3.3.

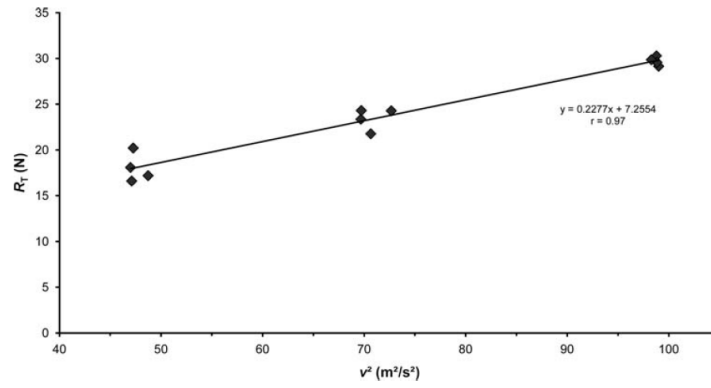


Figure 3.3: Linear regression analysis to determine C_{rr} (Debraux et al., 2011)

The rolling resistance, $D_{rolling}$, can be extracted from Figure 3.3, at the intercept between the y-axis and the curve-fitted straight, as the aerodynamic drag becomes 0. The rolling resistance coefficient is now derived using:

$$D_{rolling} = C_{rr}mg \rightarrow C_{rr} = \frac{D_{rolling}}{mg} \quad (3.5)$$

, where m is the combined mass of the rider and the bike and g is the gravitational acceleration. The resultant rolling coefficient is used in formula 3.6 to compute the drag contribution of the rolling resistance.

For the actual comparison between the power meter data and the Ring of Fire values, the drag of the bearings, drivetrain and tyres are substituted into equation 3.2, isolating the aerodynamic drag. In aerodynamic cycling studies, it is common practice to quantify the drag as drag area coefficient CdA with dimensions of m^2 to avoid the necessity of frontal area measurements. Ultimately, the drag area value can be obtained by:

$$CdA = \frac{2 \left(\eta_{drivetrain} \frac{P_{total}}{V} - C_{rr}mg - (91 + 8.7V) \cdot 10^{-3} \right)}{\rho V_{rel}^2} \quad (3.6)$$

3.3. WORKING PRINCIPLE OF PARTICLE IMAGE VELOCIMETRY

PIV is considered a non-intrusive flow visualization method, which relies on capturing the motion of tracer particles, entrained by the fluid flow. A high power laser light is used to illuminate the tracers within a confined measurement region. Shortly separated light-pulses are synchronized with one or multiple high-performance cameras, which record the scattered light from the tracer particles. The captured images are partitioned into multiple smaller "interrogation windows", in which a cross-correlation function is applied to evaluate the mean particle motion between two consecutive recordings. Ultimately, the instantaneous velocity field within the area of interest is derived from the measured particle displacement and the time interval between the light pulses. A schematic representation of a planar PIV system is shown in Figure 3.4, where a single camera is directed with the lens axis orthogonal to the measurement plane.

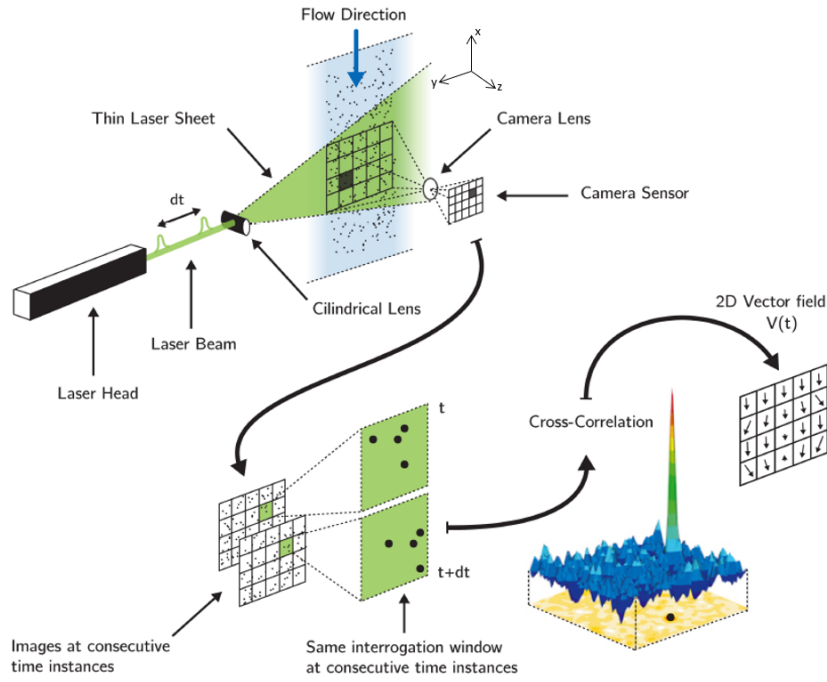


Figure 3.4: Process flow schematic of a planar PIV system, adapted from [Giaquinta \(2018\)](#)

3.3.1. TRACER PARTICLES

The choice of the appropriate tracer particle is important, as it must faithfully follow the fluid flow and exhibit good light scattering properties. To quantify the tracing fidelity, the particle's Stokes number, S_p , is considered, which is defined as the ratio of the particle response time, τ_p , over the flow characteristic time, τ_f . For instantaneous tracing characteristics, the Stokes number should be 0. Stokes numbers above 0 indicate a velocity discrepancy, called slip velocity, between the fluid and the particle, when a velocity gradient is encountered. Following such a velocity change, the particle time response is defined as the time delay after which the particle velocity has reached 63 % of the fluid velocity. τ_p is given in equation 3.7 as stated in [Adrian and Westerweel \(2011\)](#).

$$\tau_p = \frac{\left| \frac{(\rho_p - \rho)}{\rho} \right| d_p^2}{18\mu} \quad (3.7)$$

, where ρ and ρ_p is the density of the air and the tracer particle, respectively. Additionally, d_p represents the particle diameter and μ the dynamic viscosity of the fluid. To reduce the particle response time and thus the Stokes number, the particle size should be minimized or the tracer should behave neutrally buoyant ($\rho = \rho_p$). For incompressible flows, [Samimy et al. \(1991\)](#) conclude that the measurement error introduced by the slip velocity is linearly increasing with the Stokes number ($S_p = 0.2$ corresponds to an error of 2 %).

Contrary to the previously mentioned attribute of small tracer particles being advantageous for tracing fidelity, light scattering properties improve with increasing particle size. Capturing high light intensities on the camera sensor is desirable to increase the contrast to the background. [Adrian and Y. \(1985\)](#) report that for particle sizes far smaller than the laser wavelength, λ , Rayleigh scattering applies and the scattering intensity scales according to, $I_p \propto d_p^4$. The Mie scattering regime is defined in a region where $d_p \gg \lambda$, in which $I_p \propto d_p^2$ holds. Figure 3.5 displays the light scattering behaviour within the Mie scattering regime. In general, the dominant scattering direction is forward, while less light is scattered at angles between 90–180°.

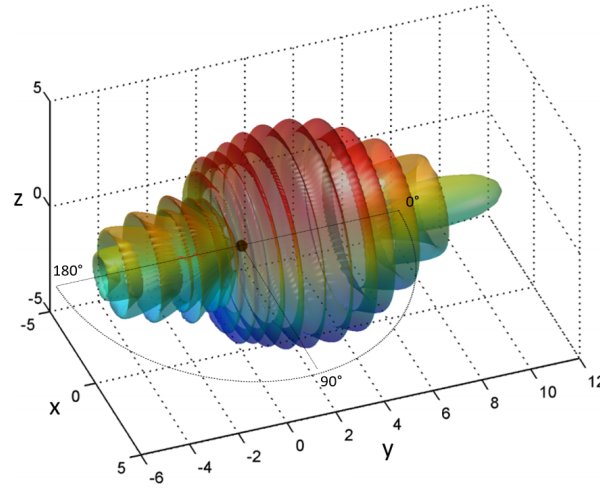


Figure 3.5: Light scattering of a $4\ \mu\text{m}$ sized water droplet at $(0,0,0)$ with $\lambda = 633\text{nm}$ (Normal vector of light ray $[0\ 1\ 0]$). Adapted from Michels (2010).

For large-scale PIV experiments, intense light scattering properties are required, which are not achieved by traditional tracers in the micron-size regime. Bosbach et al. (2008) therefore investigated Helium-filled soap bubbles (HFSB) with a diameter of $0.3\ \text{mm}$ as potential tracer particles. The increased amount of light scattering and the good tracing characteristic due to the neutrally buoyant behaviour of the HFSB (Scarano et al., 2015) enable the possibility of large-scale PIV measurements.

3.3.2. PARTICLE IMAGING

The sensor of the PIV camera detects the particle position by measuring the number of absorbed light per pixel over a certain exposure time. This is realized by using one photo-diode in each pixel, which converts the amount of absorbed photons into an electric current. This way, each pixel in the sensor plane can be assigned its own distinct intensity value. The amount of incident light during the exposure time can be controlled with the aperture diameter setting, called $f_{\#}$ or f-stop, defined as the ratio of the focal length over the lens aperture diameter (Goodman, 2004). Most lenses only allow discrete f-stop settings, whereas each larger $f_{\#}$ step halves the incoming light intensity compared to the previous one.

In addition to the light intensity, the chosen f-stop affects the amount of particle image diffraction. For small particles, this effect is to a certain extent desirable as it prevents the occurrence of "peak locking", by distributing the light intensity over adjacent pixel and thus allowing velocity reconstruction to sub-pixel accuracy. Smaller $f_{\#}$ values lead to larger diffractions which result in a circular pattern called "Airy disc". For small-scale PIV applications, the minimum particle image diameter is typically limited by the diffraction diameter d_{diff} and can be obtained through expression 3.8 (Raffel et al., 2007). Here, λ is the wavelength of the laser light and M is the magnification factor, defined as the ratio of the sensor size over the field of view size. However, in large-scale PIV experiments with increased particle size and higher Magnification factors, the geometrical image size d_{geom} dominates the diffraction phenomenon and thus the minimum particle image size can be approximated by formula 3.9. In the crossover range in between, the Euclidean sum of both contributions is taken, resulting in a minimum image particle diameter as shown in equation 3.10:

$$d_{diff} = 2.44\lambda(1 + M)f_{\#} \quad (3.8) \quad d_{geom} = Md_p \quad (3.9) \quad d_{\tau} = \sqrt{d_{geom}^2 + d_{diff}^2} \quad (3.10)$$

, where d_p is the particle diameter. It is advised by Adrian and Westerweel (2011) to ensure a min-

imum particle image diameter d_r of at least 2-4 pixel, to prevent bias errors towards integer values caused by peak-locking. Lastly, the f-stop setting can be adjusted to vary the focal depth δz , which corresponds to the volumetric depth in which the imaged objects are in focus, according to:

$$\delta z = 4.88\lambda f_{\#}^2 \left(\frac{M+1}{M} \right)^2 \quad (3.11)$$

Typically, the focal depth should exceed the laser sheet thickness to guarantee that all illuminated particles are in focus. The desired focal length f of the lens itself can be formulated as:

$$\frac{1}{f} = \frac{1}{d_i} + \frac{1}{d_o} \quad (3.12)$$

, where d_i is the distance between the image sensor and the lens and d_o is the distance between the lens and the imaged object.

3.3.3. STEREOSCOPIC PIV

The single-camera setup as shown in Figure 3.4 is limited to the reconstruction of only the two in-plane velocity components in x- and y-direction. Any out-of-plane movement within the measurement domain introduces an error of the in-plane component. Planar PIV is therefore not recommended for highly three-dimensional flows. Instead, Stereoscopic PIV provides a method to reconstruct the three component velocity vectors, by adding a second camera. Both cameras simultaneously record the same object but from different perspectives. Two common configurations for stereoscopic PIV setups are used, namely the translation method and the angular-displacement method, which are shown in Figure 3.6 and 3.7, respectively.

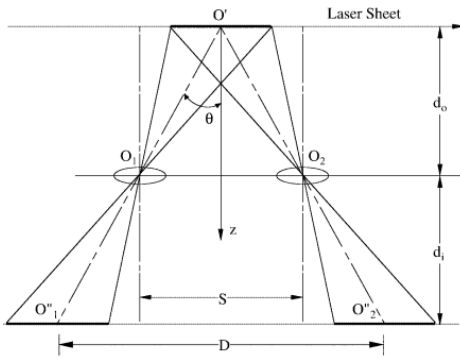


Figure 3.6: Translation stereo-PIV configuration (Prasad, 2000)

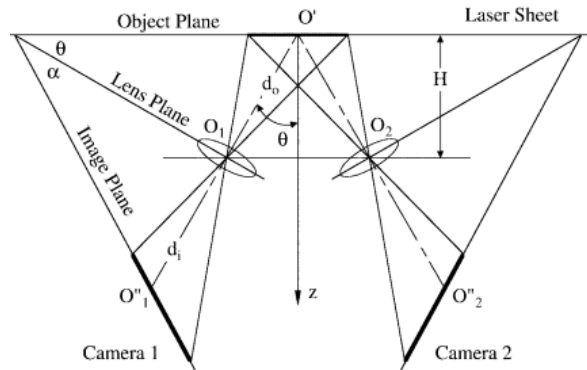


Figure 3.7: Angular-displacement stereo-PIV configuration (Prasad, 2000)

The translation method benefits from a parallel alignment between the image plane, lens plane and object plane. Perspective distortions are minimized due to a constant magnification factor across the image plane, leading to higher accuracies. However, this method is limited by the degrading image quality due to increased optical aberrations at large opening angles between the cameras (stereo-angle, 2θ). Prasad (2000) suggests a maximum stereo-angle of 30° for the translation configuration.

Larger stereo angles can be achieved with the more commonly used angular displacement setup, as the lens plane is positioned under an angle to the object plane. For maximum accuracy of the out-of-plane component, the stereo-angle is advised to be as close as possible to 90° (Raffel et al., 2007). Increasing stereo-angles on the other hand, lead to more non-uniform magnification factors across the image plane, which compromise the in-plane accuracy. Furthermore, the interrogation

windows of the two cameras are differently sized when mapped to the object plane due to the distortion caused by the stereo-angle, as shown in Figure 3.8.

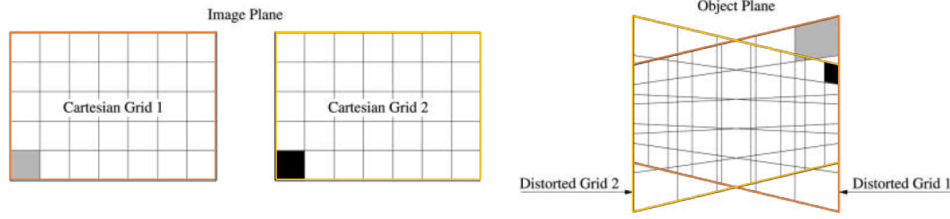


Figure 3.8: Stereo angle causes uniform grid in image plane to become warped in object plane. Adapted from Prasad (2000).

It is therefore required to perform an additional interpolation step to merge the two images onto one common de-warped mesh (Prasad, 2000). Furthermore, the angle between each camera and the measurement plane causes the outer edges of the image to lose focus. To compensate for this effect, a Scheimpflug adapter can be added to create an angle between the camera and the lens. The Scheimpflug angle, α , is ideally selected such that the object, lens and image plane coincide in one common point, which ensures that the entire object plane is in focus (Figure 3.7). For the angular-displacement setup, Lawson et al. (1997) showed that the error-ratio, e , between the out-of-plane component and in-plane components increases with decreasing half stereo-angle ($\theta = 45^\circ : e \approx 1$, $\theta = 15^\circ : e \approx 3.7$, $\theta = 5^\circ : e > 10$). For large-scale PIV measurements, the field of view requires the cameras to be placed at a large distance and thus stereo-angles above 30° are challenging to achieve.

Using two cameras with different view angles onto the measurement plane provides six unique variables, namely the u and v velocities of a particle on each of the two sensors and the angles α and β , which are measured between the cameras and the z -axis in the XZ - and YZ -plane, respectively. The construction of the out-of-plane velocity vector in an angular-displacement stereo configuration is displayed in Figure 3.9. Particle velocities u and v for each camera are defined by:

$$u_1 = -\frac{\Delta x_1}{M\Delta t} \quad (3.13) \quad u_2 = -\frac{\Delta x_2}{M\Delta t} \quad (3.14)$$

$$v_1 = -\frac{\Delta y_1}{M\Delta t} \quad (3.15) \quad v_2 = -\frac{\Delta y_2}{M\Delta t} \quad (3.16)$$

, with Δx and Δy being the horizontal and vertical displacement of the particle in the image plane. Δt is the pulse separation time and M is the magnification factor. It is common practice to mount the cameras at the same height, with the lens axis parallel to the ground. As a consequence, the angle β measured in the YZ -plane is very close to 0. According to Raffel et al. (2007), the three velocity components u, v, w can then be determined by:

$$u = \frac{u_1 \tan \alpha_2 + u_2 \tan \alpha_1}{\tan \alpha_1 + \tan \alpha_2} \quad (3.17) \quad v = \frac{v_1 + v_2}{2} \quad (3.18) \quad w = \frac{u_1 - u_2}{\tan \alpha_1 + \tan \alpha_2} \quad (3.19)$$

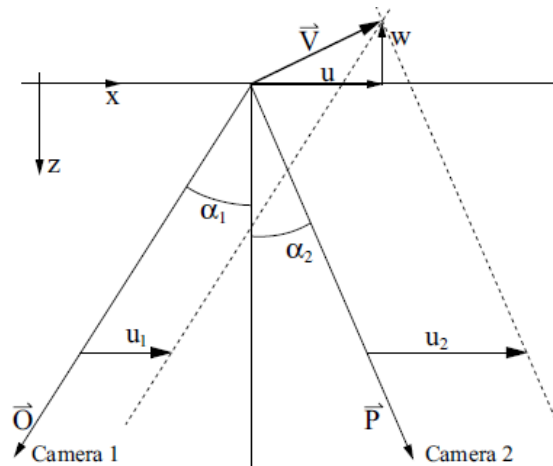


Figure 3.9: Construct out-of-plane velocity vector (Raffel et al., 2007)

In order to map the two trapezoidal image planes onto a common rectangular mesh in the object plane, the relative position between the cameras and the magnification factor distribution across the image planes need to be known. For this, a calibration plate with known dimensions is placed in the laser sheet plane, which consists of markings distributed over two levels of depth. A pinhole approach approximates the camera's positions with respect to each point on the calibration plate, by means of triangulation. For each camera, the second-order mapping function, as employed by Willert (1997), consists of twelve coefficients. A minimum of six calibration points is necessary to determine the coefficients based on a least-square method. Wieneke (2005) further proposes to perform a self-calibration procedure on 5 – 50 image pairs showing particles in motion. A disparity map between the image planes is then created, using the ensemble-averaged cross-correlation. The calibration error can be further reduced by shrinking and deforming the interrogation windows of the disparity map, based on the previous self-calibration procedure.

3.4. CONTROL VOLUME APPROACH

Based on Anderson (2011), the aerodynamic drag force of a test object can be obtained, by solving the instantaneous momentum equation within a control volume surrounding the test object. Upstream and downstream of the test object, the control volume is bound by one inlet and one outlet plane, which are oriented perpendicular to the primary flow direction. For the Ring of Fire experiment, the ground describes an impermeable boundary, while the sides of the control volume, as well as the top surfaces, are assumed to be streamlines of the flow around the cyclist (see Figure 3.10).

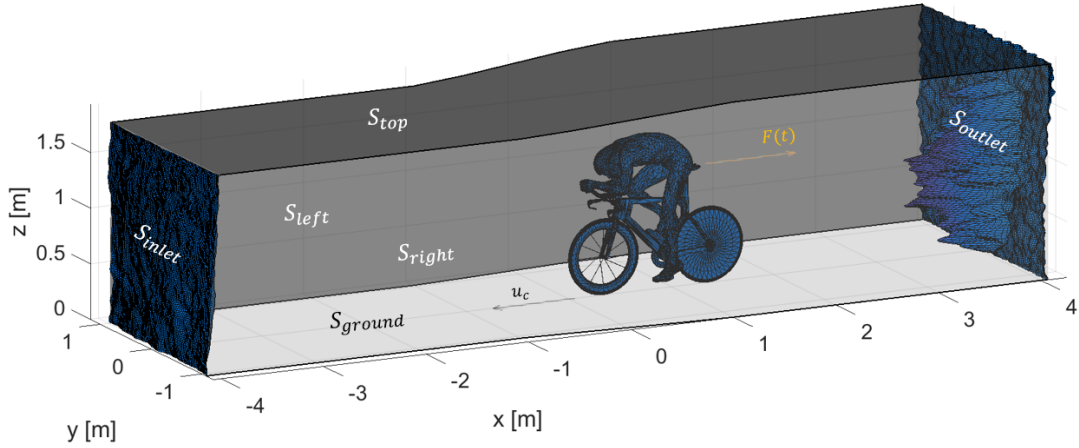


Figure 3.10: Control Volume around a cyclist

The instantaneous aerodynamic drag force $F(t)$ of the cyclist can then be determined by the integral form of the momentum equation, which holds for incompressible flows and is defined in an inertial frame of reference, thus assuming a constant test velocity, u_c (Mohebbian et al., 2012).

$$\underbrace{F(t)}_{\text{Force term}} = -\rho \underbrace{\iiint_V \frac{\partial \mathbf{u}}{\partial t} dV}_{\text{Unsteady term}} - \rho \underbrace{\iint_S \mathbf{u}(\mathbf{u} \cdot \mathbf{n}) dS}_{\text{Momentum term}} - \underbrace{\iint_S (p - p_\infty) \mathbf{n} dS}_{\text{Pressure term}} + \underbrace{\iint_S (\bar{\boldsymbol{\tau}} \cdot \mathbf{n}) dS}_{\text{Viscous term}} \quad (3.20)$$

, where $F(t)$ is the instantaneous drag force of the object, S the control surface enclosing the control volume V , \mathbf{n} the vector normal to S , while \mathbf{u} , p , p_∞ , ρ and $\boldsymbol{\tau}$ are the fluid velocity, local static pressure, freestream static pressure, density and viscous stress, respectively. In order to avoid volumetric velocity measurements, Wu et al. (2005) utilizes a derivative-momentum transformation to reformulate the volume integral of the unsteady term into a surface integral after which equation 3.20 can be rewritten into:

$$\underbrace{F(t)}_{\text{Force term}} = -\rho \underbrace{\frac{\partial}{\partial t} \iint_S \mathbf{x}(\mathbf{u} \cdot \mathbf{n}) dS}_{\text{Unsteady term}} - \rho \underbrace{\iint_S \mathbf{u}(\mathbf{u} \cdot \mathbf{n}) dS}_{\text{Momentum term}} - \underbrace{\iint_S (p - p_\infty) \mathbf{n} dS}_{\text{Pressure term}} + \underbrace{\iint_S (\bar{\boldsymbol{\tau}} \cdot \mathbf{n}) dS}_{\text{Viscous term}} \quad (3.21)$$

, where the position vector \mathbf{x} is defined in any fixed reference frame. In the following, each term of the previous expression is revisited and assumptions are made to reduce formula 3.21.

- **Unsteady term** Similar to de Martino Norante (2018) and Spoelstra et al. (2018), the unsteady contribution to the drag force due to the pedalling motion of the cyclist and the rotation of the wheels is considered to be small and is subsequently neglected.
- **Momentum term** The change in momentum within the control volume is defined by the product of the mass flow through all control surfaces and the velocity. As stated above the side and top boundaries of the control volume are streamlines, so by definition, no mass crosses these surfaces ($\mathbf{u} \cdot \mathbf{n} = 0$). Furthermore, no mass can enter or leave through the ground plane. The net momentum flow across the control surfaces can thus be obtained by the surface integral over the inlet and outlet plane alone.
- **Pressure term** In most cases the side and top surfaces are chosen far away from the body, such that freestream pressure conditions are recovered and thus the contribution to the aerodynamic drag force is zero. In case the side and top surfaces are chosen closer to the body, a pressure gradient across the surface would be present. However, due to the near-perpendicular

orientation of the normal vector \mathbf{n} with respect to the x-axis, the contribution to the drag force can still be considered as small. The pressure forces on the ground act perpendicular to the X-Y plane and thus do not add to the drag. [Blocken et al. \(2016\)](#) plot the pressure field in front of a cyclist, from which it can be concluded that beyond 6 m upstream of the cyclist, pressure effects are sufficiently decayed to be disregarded. Concerning the outlet plane, [Terra et al. \(2017\)](#) showed that in the far wake (more than five characteristic length scales) behind a spherical object the contribution of the pressure term approaches zero. More representative to the present study, [Shah \(2017\)](#) reports a negligible pressure contribution at already 80 cm behind the saddle of a time-trialing cyclist. When choosing the inlet and outlet plane outside of these pressure-affected regions, the pressure term does not influence the instantaneous drag force.

- **Viscous term** The viscous effect on the drag force, measured at the control surfaces, is negligible, according to [Kurtulus et al. \(2007\)](#) and [Mohebbian et al. \(2012\)](#).

Unlike in the wind tunnel, where the flow passes over a fixed test object, the Ring of Fire experiment is conducted by a cyclist in motion, transiting through a fixed measurement plane. The PIV measurements acquired in the planes before the transit are equivalent to the upstream planes in a wind tunnel, while the planes after the transit are regarded as the downstream planes. For the Ring of Fire experiment, a control volume is considered that moves with the cyclist at test velocity. The cyclist is thus at a fixed location in the control volume and the cyclist's velocity is superimposed over the streamwise velocity distribution of the inlet and outlet plane.

Rewriting equation 3.21 considering the previously stated assumptions results in:

$$F(t) = \rho \iint_{S_{inlet}} (u_{inlet}(y, z) + u_c)^2 dS - \rho \iint_{S_{outlet}} (u_{outlet}(y, z) + u_c)^2 dS \quad (3.22)$$

In addition to the momentum conservation within the control volume, also mass conservation is invoked, which is stated in expression 3.23. As a result of the velocity deficit present in the outlet plane and the assumption that no mass crosses the side walls, the inlet plane needs to be smaller-sized than the outlet plane.

$$\rho \iint_{S_{inlet}} (u_{inlet}(y, z) + u_c) dS = \rho \iint_{S_{outlet}} (u_{outlet}(y, z) + u_c) dS \quad (3.23)$$

The resultant drag force from equation 3.22 is transformed into the non-dimensional drag coefficient C_D :

$$C_D(t) = \frac{2F(t)}{\rho (\overline{u_{inlet}} + u_c)^2 A} \quad (3.24)$$

, where A is the frontal surface area of the cyclist. In the denominator of equation 3.24, the relative velocity of the cyclist with respect to the surrounding fluid must be substituted and therefore the velocity in the inlet plane is averaged and added to the velocity of the cyclist. Given that S_{inlet} and S_{outlet} are chosen in accordance with the mass preservation law, the final expression is:

$$C_D A(t) = \frac{2\rho \left[\iint_{S_{inlet}} (u_{inlet}(y, z) + u_c)^2 dS - \iint_{S_{outlet}} (u_{outlet}(y, z) + u_c)^2 dS \right]}{\rho (\overline{u_{inlet}} + u_c)^2} \quad (3.25)$$

4

EXPERIMENTAL INSTALLATION, SETTINGS AND PROCEDURE

This chapter begins with an introduction to the experimental installation, which includes the setup of the Ring of Fire system (section 4.1) and the description of the test objects (section 4.2). In addition, the acquisition settings for the PIV system are presented in section 4.3, as well as the system's calibration procedure (section 4.4). The chapter concludes with the test matrix of the campaign and the task sequence to be performed for each individual test, in sections 4.5 and 4.6, respectively.

4.1. RING OF FIRE SETUP

The current campaign envisages operating the Ring of Fire system with continuous motion of the cyclist, which requires a spacious testing facility, preferably located indoors, to eliminate environmental factors. The selected test location is presented before providing relevant information on the individual components of the Ring of Fire system. The description is supported by a dimetric and a frontal view of the installation shown in Figure 4.5.

4.1.1. TEST FACILITY

The measurement campaign is conducted in an indoor ice-rink, located at Vondellaan 41 in 2332 AA Leiden, Netherlands. The facility offers a 39.1 m wide and 77.4 m long flat concrete surface and allows the cyclist to ride loops of 190 m length in clockwise direction. The lap can be described as two semi-circles with a radius of 17.66 m, which are connected by two 39.5 m long parallel straights (see Figure 4.1). A preliminary test has shown that the highest velocity that can be ridden continuously and safely on this track is 33 km h^{-1} . During the PIV measurements, the overhead lamps above the track are switched off to increase the contrast between the tracer particles and the background. By illuminating the infield of the track and directing one external lamp into a darker region, it is ensured that the riders have sufficient visibility throughout the test. Ambient temperature, humidity and pressure are measured by a mobile digital weather station.

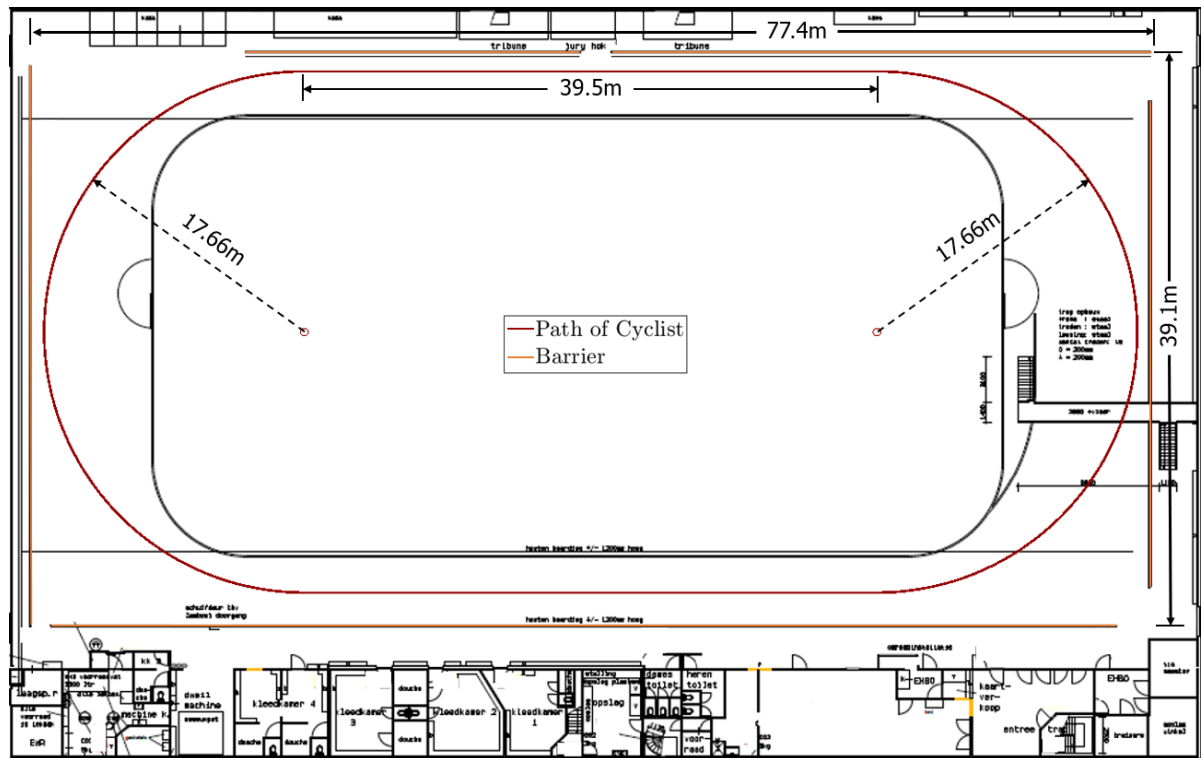


Figure 4.1: Top view of testing ground

4.1.2. TUNNEL STRUCTURE

In order to concentrate the seeding particles near the measurement plane, a 10 m long, 4 m wide, and 3 m tall tunnel structure is erected and placed at the end of one of the two straights (Figure 4.2). Larger gaps in the modular panel construction are taped with black duct tape. An overhead laser, installed at the tunnel ceiling, projects a thin red line onto the ground. Along with markings on the floor the laser line guides the cyclists to the lateral centre of the tunnel when transiting the measurement plane.

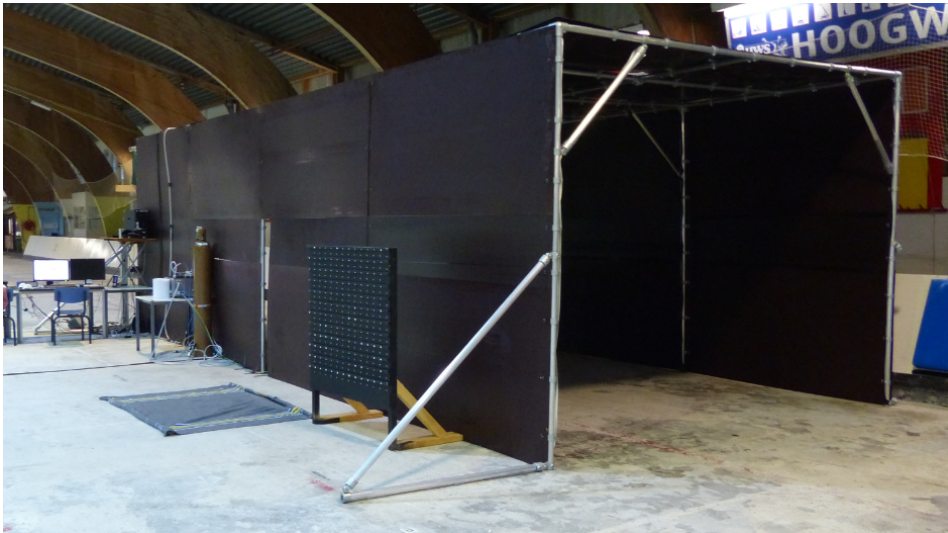


Figure 4.2: Tunnel structure (side/rear view)

4.1.3. LASER LIGHT

The laser sheet itself is positioned 5.15 m downstream of the tunnel entrance and passes through a 175 cm tall and 20 cm wide opening in the side wall. To avoid strong unwanted laser reflections, which might lead to pixel saturation on the camera sensor, all metal beams in the field of view of the cameras are covered with black duct tape. The tracer particles are illuminated with a double-pulse Nd:YAG Evergreen 200 laser from the manufacturer Quantel, emitting a green laser with a wavelength of 532 nm, a maximum pulse energy of 200 mJ, and a maximum repetition rate of 15 Hz (Quantel, 2015). The optical laser head unit is placed in the infield of the track on a horizontal profile beam, at a distance of 5.5 m measured from the side wall of the tunnel. To convert the 6.35 mm wide circular light beam as emitted by the laser into the desired laser sheet, a combination of three lenses are mounted on the head unit. First, the beam is expanded with a diverging spherical lens of focal length $f = -50\text{mm}$, before a converging cylindrical lens with $f = 60\text{mm}$ reduces the widening in horizontal direction. Finally, a strong diverging cylindrical lens with $f = -30\text{mm}$ is used to expand the beam in vertical direction. The lenses are mounted at a distance of 200 mm, 225 mm and 275 mm from the laser output aperture. The laser sheet in the tunnel spans the entire width and is of trapezoidal shape by measuring 2 m height on the right and 3 m height on the left. The laser sheet thickens from 32 mm on the right side to 50 mm on the left side, equating to an average thickness of 41 mm. Thinner light sheets would increase the laser light intensity, but would lower the amount of illuminated particles and reduce the depth of view in streamwise direction captured by the two PIV-cameras.

4.1.4. ACQUISITION HARDWARE

Two scientific CMOS Imager cameras by LaVision are utilized to capture the PIV images (see Figure 4.3). This camera model is capable of recording images at 50 Hz in full resolution at 2560 px x 2160 px. A 16-bit image depth allows for 65,536 intensity levels to be distinguished. The pixel pitch is given at 6.5 μm , which corresponds to a sensor area of 16.6 mm x 14.0 mm. Both cameras are equipped with a AF Nikkor 35 mm 1:2D lens, an optical bandpass filter, transmitting green wavelengths and a Scheimpflug adapter to reduce the out-of-focus effect caused by the inclination between the sensor plane and the measurement plane. On the lens, the f-stop setting is tuned to 8 to ensure that all particles in the measurement plane are in focus.

The pair of cameras is placed 5.20 m upstream of the measurement plane in an angular-displacement

stereo configuration. At either side of the 4 m wide tunnel entry, one sCMOS camera is mounted horizontally at 0.91 m height, pointing towards the laser sheet's center. The resultant field of view captured by both cameras is 2533 mm x 2132 mm, yielding a magnification factor of 0.0065 and a digital image resolution of 1.01 px/mm. Two MDR cables, transmitting the data from the left camera to the computer terminal, need to cross the track, but are limited to 5 m length. According to the camera manufacturer, longer cable length could lead to data loss. The cables are therefore suspended by ropes from the tunnel ceiling at a height of 2.5 m above the ground, where the cyclists can safely pass underneath.

4.1.5. SEEDING PRODUCTION

The tracer particles dispensed into the tunnel are helium-filled-soap-bubbles (HFSB) with a diameter of 0.3 mm (Scarano et al., 2015), suitable for large-scale PIV measurements, as discussed in section 2.1. The bubble production is operated through a Fluid Supply Unit (FSU) provided by LaVision, where the pressure for helium, air and soap is adjusted. An air compressor unit is already permanently installed at the testing facility, which serves as the air supply for the control unit. Prior to the two main testing days, an external air filter from the manufacturer HBM Machines is installed between the air compressor and the control unit to dehumidify the air and filter out small dust particles, which would otherwise clog the control unit. The helium is supplied by a pressurized bottle while the soap solution is poured into a reservoir inside the FSU. In Scarano et al. (2015), the soap solution is described as a mixture between water, glycerine and soap, and is commonly referred to as bubble fluid solution (BFS). Continuous production of the tracer bubbles is achieved at helium, air and soap pressures of 2.6bar, 2.1bar and 1.7bar, respectively. The control unit feeds the air, helium and soap through separate hoses into a seeding rake, designed by the aerodynamics department of the TU Delft. The seeding rake consists of 10 vertical wings, on which in total 200 3D-printed nozzles are installed with a uniform spacing of 5 cm. Inside the nozzles, the helium, air and soap are mixed to form the HFSB tracers. The bubble production rate per nozzle in nominal conditions lies between 20.000–60.000 bubbles per second according to Engler Faleiros et al. (2018). Of the 200 nozzles one can expect at least 10 % not to function properly. The seeding rake itself is placed 2.5 m upstream of the measurement plane, parallel and adjacent to the tunnel side wall (see Figure 4.4). Foaming on the seeding rake eventually led to the soap dripping from the wing elements into a collection basin. At the end of the campaign, which covered in total four full days of testing, three bottles with dirt-contaminated soap were retrieved from the sump. During the last two days of the experiment, the seeding system was operational for approximately 2.5 h, while 4 full bottles of the bubble fluid solution were used, amounting to 37.5 min per bottle.



Figure 4.3: 1) BNC cable - 2) Multi-angle mount - 3) MDR cables - 4) sCMOS camera - 5) Scheimpflug adapter - 6) Lens - 7) Bandpass filter



Figure 4.4: Seeding rake attached to vertical tunnel beam standing in a sump

The continuous motion of the cyclist in the hall created a large-scale circulation in the building, which was evident when the bubbles were carried downstream as soon as they were produced at the seeding rake. After a number of passages, this led to inhomogeneous and insufficient seeding in the measurement plane, as the particles agglomerated on the side of the seeding rake. To counteract this circulation, a person carrying a 1.8 m x 1.55 m blanket, walked slowly, at approximately 1.25 ms^{-1} , through the tunnel in opposite cycling direction as soon as acquisition for each loop ended. A more detailed explanation of this encountered problem is provided in appendix A.

4.1.6. TRIGGERING HARDWARE

To automate the process of image acquisition and thus improve the consistency between datasets, a WS/WE12L-2P410 photo-detector (PHD) from SICK is installed 13.4 m upstream of the measurement plane. The receiver and transmitter are placed on the ground on either side of the track at a separation distance of 4.1 m. Each of the two components are connected by a round 6 mm thick cable to the interface box. Since the cable to the transmitter has to cross the track, the effect on the rider is minimized by replacing the standard cable with a flexible flat cable, which is then taped to the ground. The photo-detector system feeds the triggering signal through a BNC cable from the interface box to the Trigger Input terminal of the Programmable Timing Unit (PTU) through the Trigger pin of the PTU connector 1008431.

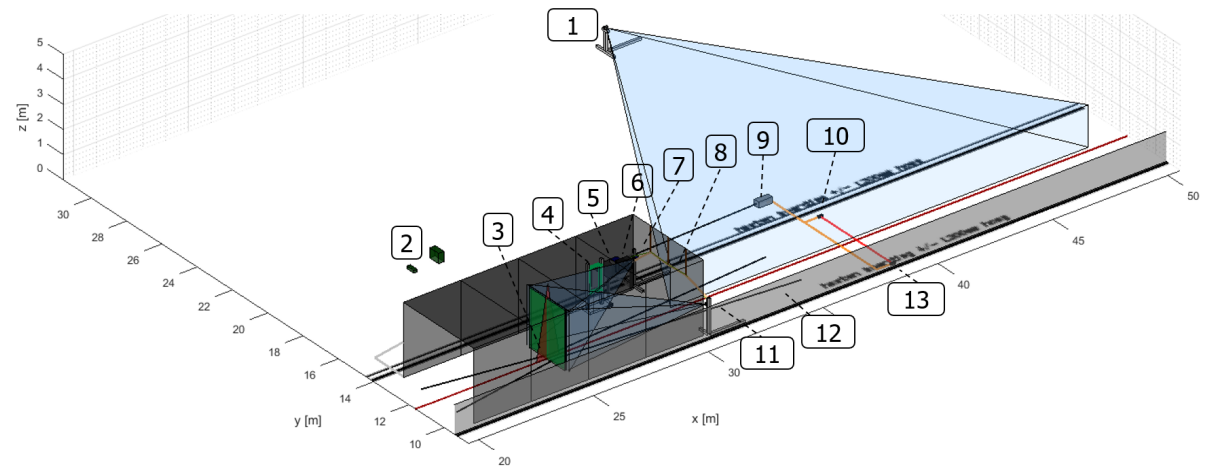
The acquisition system is controlled through the *Davis* 8.4.0 software from LaVision, where a recording sequence is created. In the image acquisition menu, the desired number of images and the recording frequency are chosen. Furthermore, the trigger input is set to *by "Start" input* to disable manual triggering by the *Davis*-user. The passage of the cyclist momentarily interrupts the laser beam between the transmitter and the receiver, which triggers a signal transmission from the photo-detector to the PTU. Image acquisition then either starts instantaneously or after a user-defined time delay. After all images from one transit are acquired and saved, the system is active again and waits for the next trigger input by the cyclist. Inside *Davis*, the number of repetitions of this sequence can be controlled through the *Loop* item, which should be added into the recording sequence in front of *Image Acquisition*.

During the test, no false triggering due to external objects passing the photo-detector occurred. In some cases, the cyclist's velocity was too high and storing of previously acquired images was not completed in time. In these instances, the triggering system was not yet active, and for the single cyclist no images were recorded for that particular transit, while in the drafting configuration the second cyclist triggered the system and the amount of images in front of the leading cyclist were reduced. Here, verbal communication between the *Davis*-operator and the test riders was necessary to re-synchronize their speed with the acquisition system.

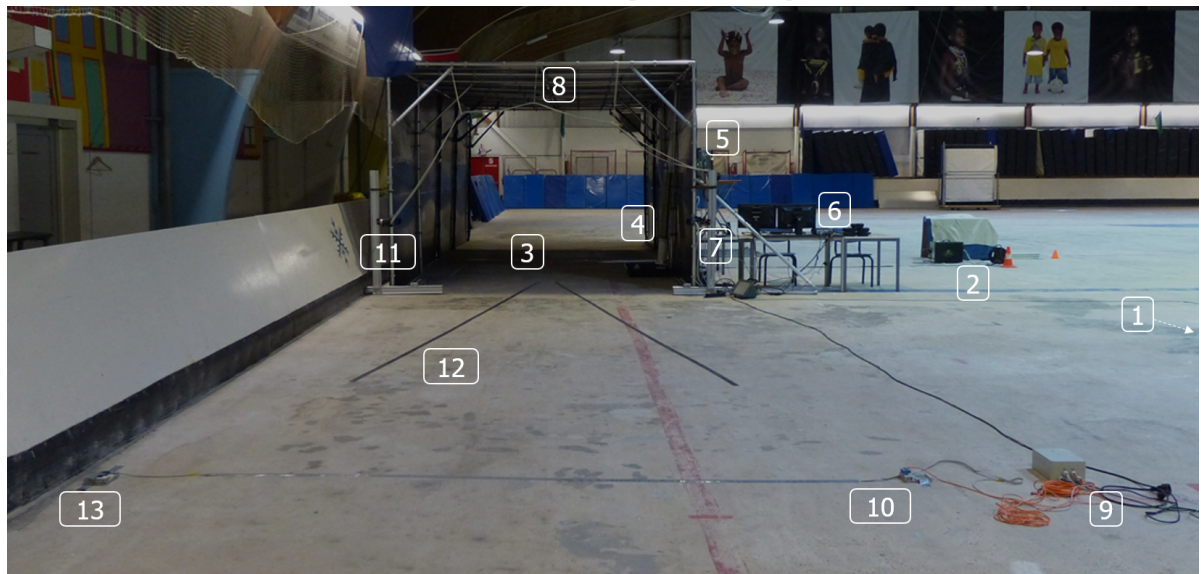
4.1.7. DRAFTING DISTANCE

The second of the two main testing days focuses on drafting effects at separation distances between the two riders of 8 m and 12 m. The drafting distance is measured from the front wheel of the leading cyclist to the front wheel of the trailing cyclist. At two locations around the lap, a pair of two cones are placed and separated by the respective targeted drafting distance. The trailing cyclist is responsible for maintaining a constant gap to the leading cyclist, but is supported by verbal feedback from a third person that visually monitors the distance between the riders from the infield of the track. In order to quantify the rider's spacing, a digital Panasonic Lumix DMC-FZ2000 camera is placed in the infield 15.5 m away from the track, 9.2 m in front of the tunnel entry and at a height of 1 m. This results in a side view of both cyclists capturing 18.2 m upstream of the tunnel and the tunnel entry itself. Throughout the test, a video is recorded with minimum resolution of 640 px x

480 px at 25 Hz to keep the data size low. The separation distance is then determined using digital image processing, which is presented in section 5.7.



(a) Dimetric view of experimental setup



(b) Front view of experimental setup

Figure 4.5: 1) Drafting camera - 2) Evergreen Laser - 3) Laser line for lateral position - 4) Seeding rake - 5) PC Terminal - 6) PTU - 7) sCMOS camera right - 8) Suspended MDR cable - 9) PHD interface box - 10) PHD receiver - 11) sCMOS camera left - 12) Convergent trajectory markings - 13) PHD transmitter

4.2. TEST OBJECTS

The Ring of Fire experiment is conducted focusing on cycling aerodynamics. For this experiment, a total of three test riders attended the campaign, namely one amateur and two professional cyclists. Throughout two days with the amateur cyclist, the measurement procedure was revised. The final results of chapter 6 are exclusively extracted from the measurements carried out with the professionals, so this section is limited to the information of these two participants and their respective bicycles. Additionally, a description of the utilized power meter device is given.

4.2.1. THE RIDERS

For the main testing phase of this campaign, a male and a female cyclist from Team Sunweb are invited. The individual tests on the first testing day are conducted by the male athlete only, while the drafting tests on the next day are carried out by both cyclists.

The female athlete is a current professional and performs the role of the leading rider during the drafting experiment. Throughout the test, she wears a time trial skin suit with short legs and long arms provided by Team Sunweb, as well as a Giant Rev Road Cycling helmet from 2017. Her body height and weight amount to 170 cm and 59.1 kg, respectively.

The male is a former professional athlete and conducts the individual tests, as well as the drafting tests, where he is assigned the role of the trailing cyclist. For the tests, the athlete wears a short leg and short arm time trial skin suit from Team Sunweb. Throughout the two testing days two different helmet types are tested, namely the 2017 Giant Rev Road Cycling helmet and the 2017 Rivet TT Time Trial helmet, which are displayed in Figures 4.6a and 4.6b, respectively. His body height is measured to be 187 cm, while his weight amounts to 79 kg.

In addition to the skin suit and helmets, the riders wear over-shoes extending to half of their calves, as well as laser safety goggles that absorb the wavelengths of the light emitted by the PIV laser unit.



(a) 2017 Giant Rev Road Cycling helmet (b) 2017 Giant Rivet TT Time Trial helmet

Figure 4.6: Helmet types used throughout the campaign

4.2.2. THE BICYCLES

The bikes utilized in this experiment are the Team Sunweb time trial bikes, model Trinity Advanced SL 2018 from Giant (LIV branded for the female athlete). Both bikes are equipped with a PRO Tubular disc as a rear wheel. The male athlete uses a 625 mm deep front wheel, whereas the female athlete rides a four-spoke front wheel. All wheels have a diameter of 66.7 cm, including the Tubular Vittoria Corsa G 23mm tyre. The tyre pressure is checked with a SKS Rennkompressor pump and set to 5 bar. On the male athlete's bike, a magnetic sensor attached to the chainstay measures the rear wheel rotations per time by detecting the passage of a magnet, which is taped to the disc wheel. In combination with the tyre circumference of 2096 mm, the cyclist's velocity can be determined. The same bike is equipped with a 39 – 53 chainring arrangement and an 11-speed cassette with sprocket teeth of: 11-12-13-14-15-17-19-21-23-25-28. The overall length for the female bike amounts to 1.60 m, while the male bike measures 1.666 m in length and weighs 8.8 kg.



(a) Time trial bike of female rider

(b) Time trial bike of male rider

Figure 4.7: Giant Trinity Advanced SL 2018

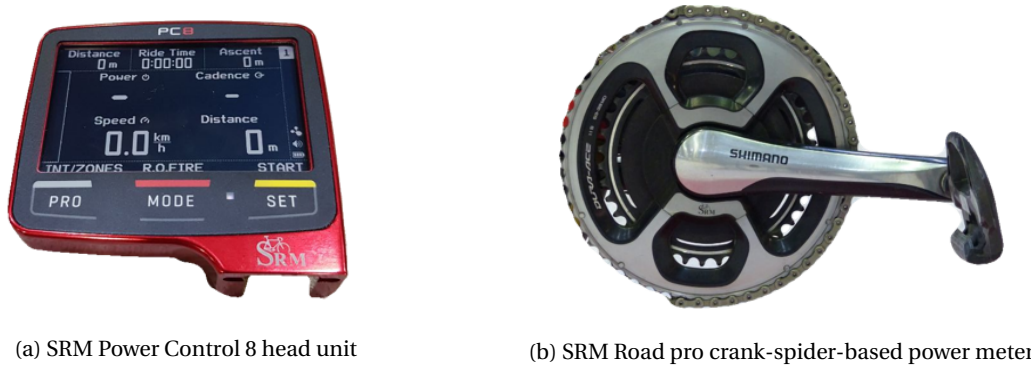
4.2.3. POWER MEASURING DEVICE

The main objective of this thesis is the comparison of the Ring of Fire measurements with simultaneously acquired power meter data. For this campaign, a crank-spider-based power meter is provided by Schober Rad Messtechnik (SRM), which is widely regarded as the benchmark for power meter devices (Duc et al. (2007) and Passfield et al. (2017)). The model SRM Road Pro comes with a crank length of 175 mm and is installed through the Shimano pressfit BB86 bottom bracket of the male athlete's bike (Figure 4.8b). Four strain gauges are placed with 90° spacing to each other inside the crank-spider, measuring the deformation of the material, which is proportional to the torque applied by the rider Betrucci et al. (2005). The torque is derived from the product of force on the pedal and the length of the crank arm. To obtain the power output by the rider, the torque is multiplied by the angular velocity of the crankset. SRM claims a power output accuracy of $\pm 2\%$ over a range of 0–4096 W. The measurable cadence range of this battery-powered SRM Road Pro model is indicated to be 30–255 rpm SRM (2010). After each complete crank revolution, new power and cadence numbers are obtained, which are then linearly interpolated with equation 4.1 (Underwood, 2012), before being transmitted from the power meter to the SRM PC8 head unit via the wireless ANT+Sport protocol at 1 Hz.

$$P_{athlete}^i = P_i^p + \frac{t_i - t_i^p}{t_i^s - t_i^p} (P_i^s - P_i^p) \quad (4.1)$$

, where $P_{athlete}^i$ is the instantaneous power produced by the rider in Watts at time t_i , P_i^p and t_i^p are the power and time of the previous recording, while P_i^s and t_i^s are the power and time readings at the subsequent recording.

The power data recording is initialized with a 5 s time delay after the cyclist has gotten the bike rolling, while the first velocity data is recorded after the magnet on the rear disc has passed the speed sensor twice, which is typically within 1 s. The display background color of the PC8 head unit is changed to black with white letters for better visibility. During the test, the following parameters are shown on the display: Power in [W], velocity in [kmh] with one decimal digit, cadence in [rpm] and the distance in [km] with three decimal digits (Figure 4.8a). After the test, the data are transferred to the computer, where SRMX Training Software is executed before further processing in MatLab is performed.



(a) SRM Power Control 8 head unit

(b) SRM Road pro crank-spider-based power meter

Figure 4.8: Power measuring system

4.3. ACQUISITION SYSTEM TEST SETTINGS

The PIV image recording procedure is controlled through four main parameters, which are elaborated on in this section. The selected values for each test throughout the campaign are summarized in table 4.1.

4.3.1. PULSE SEPARATION TIME, Δt

The PIV-images are recorded in double-frame double exposure mode. The two frames are temporally spaced by a pulse separation time, Δt . In theory, long pulse separation times reduce the measurement error, however, it also causes a decrease in the amount of particles that can be correlated to each other and thus leads to an increase in measurement noise [Raffel et al. \(2007\)](#). Literature suggests the maximum out-of-plane displacement of a particle to be 1/4 of the laser sheet thickness [Keane and Adrian \(1990\)](#). The pulse separation between the two consecutive images is then derived from this one-quarter rule. In section 4.1.3, it is established that the laser sheet has an average thickness of 41 mm and therefore, according to the one-quarter rule, the maximum out-of-plane displacement of the particles amounts to 10.25 mm. The seeding particles are transported by the velocity field in the wake of the cyclist, which is a function of the cyclist's velocity itself. Due to turbulent diffusion, the wake velocity behind the rider decreases in streamwise direction. Ideally, a non-constant Δt would be defined, which increases with reducing wake strength. However, this option is currently not available with the used acquisition software. A compromise for computing Δt is thus found by using the average maximum out-of-plane velocity in the near wake, which is equal to approximately 75 % of the cyclist velocity.

4.3.2. TIME DELAY OF TRIGGER

As mentioned in section 4.1.6, the trigger system is placed 13.4 m in front of the measurement plane. To avoid excessive freestream data ahead of the cyclist and thus extensive storing times, a time delay t_{delay} is introduced, which retards the triggering of the PIV-system after the cyclist transits through the photo-detector. The maximum time delay $t_{delay_{max}}$ of the solo test is derived from the requirement that at least 10 m in front of the cyclist are acquired by the PIV-system, which ensures a sufficient number of freestream planes that are neither influenced by pressure effects nor by the obstruction caused by the cyclist.

$$t_{delay_{max}} = \frac{d_{phd-laser} - 10m}{V} \quad (4.2)$$

, where $d_{phd-laser}$ is the distance between the photo-detector and the measurement plane and V is the test velocity. During the individual tests, smaller t_{delay} values are used to account for a possible uncertainty in the triggering time. In the drafting configuration, the time delay is increased to reduce the number of freestream images in front of the leading cyclist, as those are of limited interest

for the current investigation.

4.3.3. IMAGES PER LOOP

The upper limit of PIV-images taken per loop is determined by the number of images that can be recorded and saved before the cyclist passes the photo-detector on the subsequent loop. This requirement can be summarized as:

$$t_{lap} > t_{delay} + t_{acquisition} + t_{storing} \quad (4.3)$$

, with t_{lap} indicating the necessary time for the rider to complete one lap and $t_{acquisition}$ representing the recording time of the PIV-system. The last parameter, $t_{storing}$, is the time it takes to transfer the images from the RAM storage of the camera onto the computer's hard drive. The required time is highly dependent on the writing speed to the hard drive. The installed SSD hard disk with a nominal writing speed of 500 MB/s allowed a storage rate of 2.25 image pairs per second at full 5.524Mpx resolution.

For this test, it is desired to capture at least 10 m in front and 10 m behind the cyclist of interest, which is the trailing cyclist in the drafting scenario. Additionally, the length of the bike needs to be taken into account, which then amounts to a total measurement length of 21.66 m. The minimum number of images is then a function of test velocity and recording frequency, f_{rec} .

$$n_{images_{min}} = \frac{21.66m}{V} f_{rec} \quad (4.4)$$

4.3.4. RECORDING FREQUENCY OF THE PIV-SYSTEM

The maximum recording frequency for this setup is limited by the Evergreen laser to 15 Hz. For the individual runs, this settings is used while for the drafting tests, a lower recording frequency is chosen to capture a larger measurement volume without increasing the amount of total images that need to be stored.

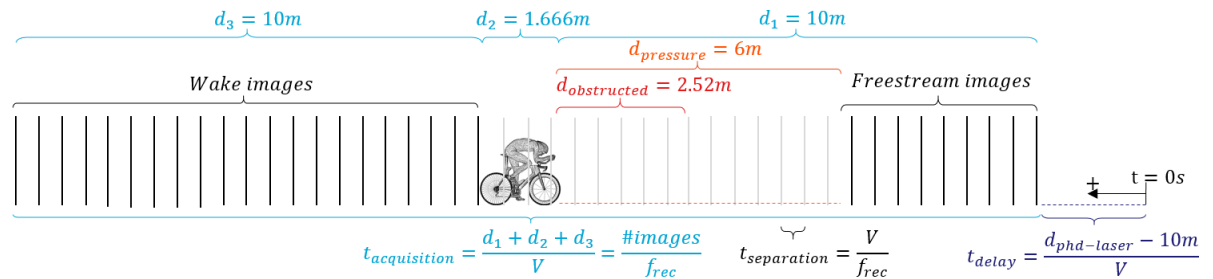


Figure 4.9: Side view to scale of acquisition phase at $V = 30kmh^{-1}$ and $f_{rec} = 15Hz$. Time starts at passage of photo-detector

4.4. SYSTEM CALIBRATION

At the beginning of each testing day, the PIV-system is calibrated using a wooden 1.2 m x 1.2 m x 0.04 m large calibration plate, manufactured by the aerodynamic department of the TU Delft. For the calibration procedure, the calibration plate is placed in the tunnel centre, aligned with the plane of the laser sheet. The front of the calibration plate consists of two levels, which are offset in depth by 20 mm. On each plane, 156 white dots of 8 mm diameter are placed, with a horizontal and vertical spacing of 90 mm to the neighbouring dot on the same plane, and a 45 mm horizontal and vertical spacing to the adjacent dot on the other plane. During the transport, 44 white dots were damaged and needed to be replaced by larger white round markings with a diameter of 15 mm. This self-produced calibration plate requires the definition of a new calibration plate in Davis, where

the above stated parameters are entered.

Initially, an intensity calibration of the cameras is performed with covered lenses. The aperture setting on each lens is reduced to 2 for the calibration procedure. The Scheimpflug and focal length is then manually adjusted, until the best focus for the area of interest is found. 10 images of the calibration plate are acquired and averaged, to perform the geometrical calibration. The final RMS fit did not exceed $5.3px$ for one camera and $1.48px$ for the other. Compared to previous Ring of Fire experiments, conducted by [Spoelstra et al. \(2018\)](#) and [de Martino Norante \(2018\)](#) these root mean square fits show large values. One possible cause might be the two differently sized white dots placed on the calibration plate. As shown in Figure 4.10, the software is unable to precisely locate the centre of these larger-sized dots during the geometrical calibration, and could thus lead to a discrepancy between the two cameras. To refine the calibration an additional self-calibration step is undertaken, which requires the recording of 100 images capturing sufficient movement of tracer particles. For this, the far wake of the cyclist is recorded at 15 Hz. In total, the self-calibration sequence is repeated 4 times, employing the procedure of [Wieneke \(2005\)](#) until convergence is reached. Two passes with an interrogation window size of $64px \times 64px$ and an overlap of 50% are performed, followed by two passes using a $32px \times 32px$ interrogation window size and 75% overlap. After self-calibration the disparity reduced to $0.5px$ and is thus in the acceptable range according to [Raffel et al. \(2007\)](#). The recreated stereo angle between the cameras amounted to 34.1° .

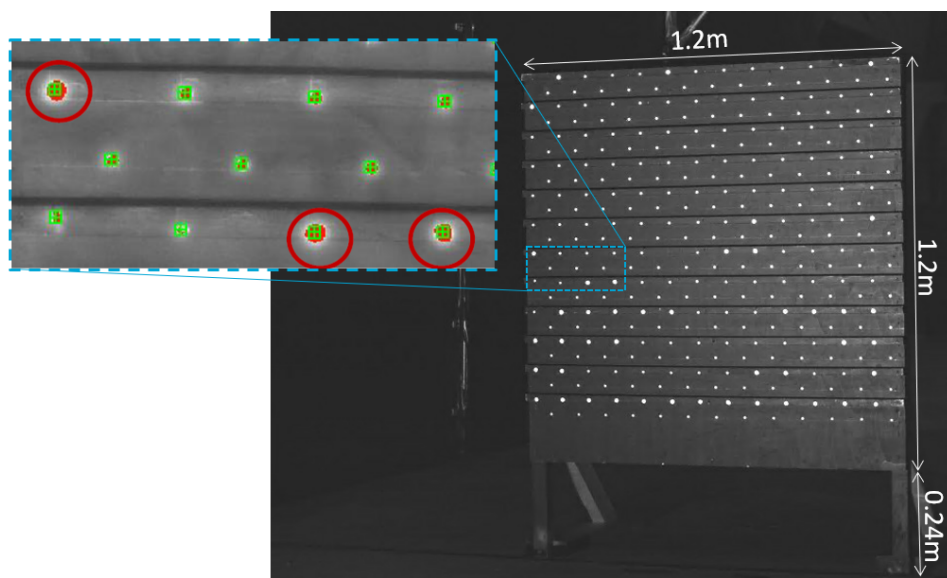


Figure 4.10: Big calibration plate with enlarged image of geometrical calibration

4.5. TESTING SCHEDULE

The experiment is scheduled for two weeks, the first day of which is used to transport and set up the modular tunnel structure. A van with a loading bay, exceeding the length of the longest tunnel beam (4 m) is required for transportation. With eight people, the tunnel structure is constructed within one day. The second day is used to install the PIV-system, whereas the third day is spent on creating the laser sheet and aligning, as well as calibrating the cameras. On the fourth and fifth day, an amateur cyclist attends the campaign to troubleshoot the procedure planned for the following two main testing days, where the former professional male athlete participates on both days and the professional female athlete attends for the second day. The test matrix of these two days is presented in table 4.1. On the first of the two main days, the male athlete initially performs the

rolling coefficient test, which is based on the method explained in section 3.2. Thereafter, individual PIV-measurements are acquired from the male athlete alone, comparing the aerodynamic drag differences between upright and time trial positions, as well as between time trial and road helmets. On the second day, the female rider is assigned the role of the lead cyclist, while the male rider follows her at a predefined distance at a target velocity. Here, the aerodynamic drag of only the male rider is of interest and is compared to his individual runs performed previously. For this second testing day, local journalists are invited to attend the campaign. Two days are then spent to dismantle the entire experiment including the tunnel structure, which is taken down by four people within half a day.

Table 4.1: Test matrix

Test name	Pos.	Velocity [kmh^{-1}]	Gap [m]	Helmet			Acquisition system			
				#1	#2	# Laps	Δt [ms]	# Images	t_{delay} [s]	f_{rec} [Hz]
<i>Rolling coef.</i>										
		15								
		18								
		21								
	UR ¹	24	-	-	TT	10	-	-	-	-
		27								
		30								
		33								
<i>Individual</i>										
	UR	30	-	-	TT	60	1.6	40	0.26	15
	TT ²	30	-	-	TT	60	1.6	40	0.26	15
	TT	30	-	-	Road	60	1.6	40	0.26	15
<i>Drafting</i>										
	TT	30	12	Road	Road	40	1.6	37	0.8	10
	TT	30	8	Road	Road	40	1.6	37	0.8	12.5

¹ Upright

² Time-trial

4.6. TESTING PROCEDURE

The testing procedure can be divided into tasks that are performed once per testing day, once per morning or afternoon session, as well as immediately prior to, during or after each run. Figure 4.11 provides an overview of the task sequence that needs to be executed throughout the experiment.

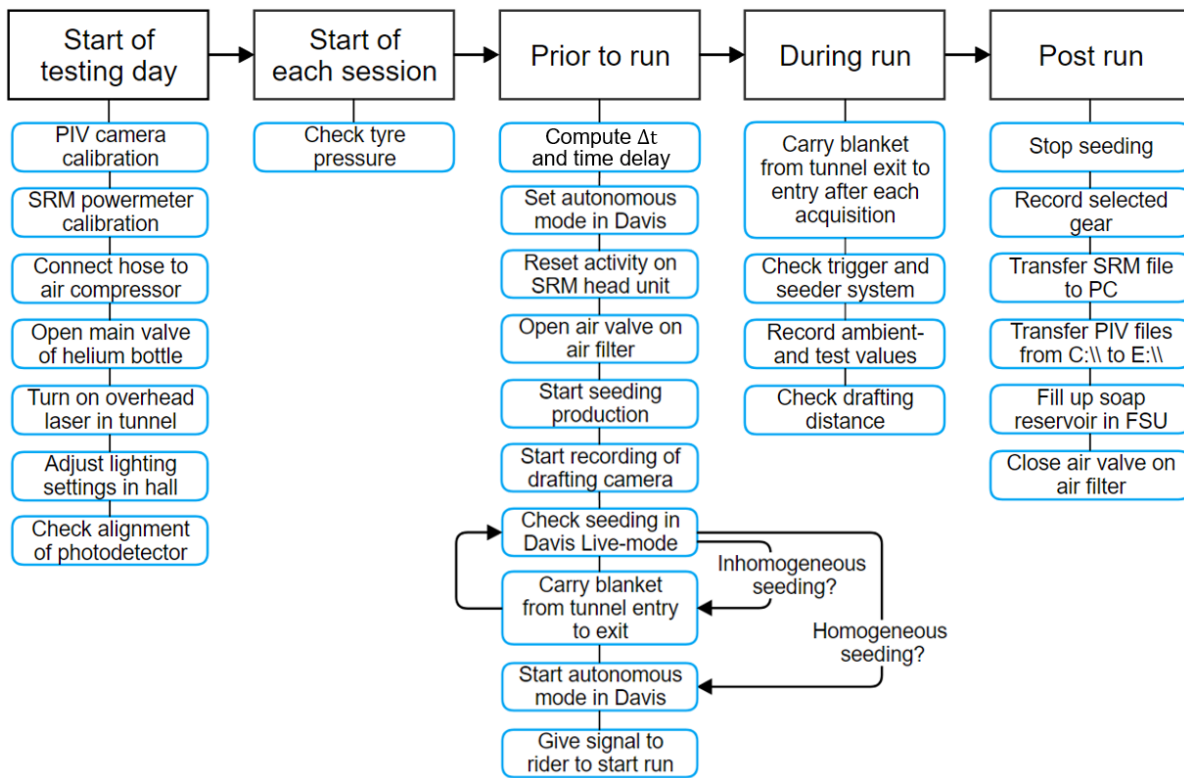


Figure 4.11: Experimental procedure

5

DATA REDUCTION AND ANALYSIS TECHNIQUES

The following chapter is intended to inform the reader about the processing techniques employed after the measurement campaign to eventually obtain drag area values for both the power meter and the Ring of Fire approach. This chapter begins with a description of the data reduction methods applied to the power meter data in section 5.1, in which a necessary velocity correction during cornering is explained, followed by the implementation of the relative velocity, as well as the outlier removal process. Section 5.2 covers the three main steps undertaken in the Davis software to obtain vector information from the raw PIV images. Next, an algorithm is introduced in section 5.3, which aims to contour the wake region behind the cyclist. An approach to compensate for upstream pressure effects is proposed in section 5.4. The choice of the appropriate inlet plane under drafting conditions is examined in section 5.5, before the wake alignment procedure is elaborated on in section 5.6. This chapter concludes with the ansatz chosen to evaluate the drafting distance and to synchronize the Ring of Fire and power meter data, which are given in sections 5.7 and 5.8, respectively.

5.1. DATA REDUCTION OF POWER METER DATA

In the beginning the post-processing steps are described, which are applied to the power meter data. The recorded files from the SRM head unit were converted into a text file and loaded into the MATLAB software, where further data processing takes place.

5.1.1. VELOCITY CORRECTION

The cyclist's power output is utilized to move the mass of the entire bike-rider system around the track. The mass can representatively be collapsed into the centre of gravity (CG), which is estimated to be at the rider's saddle height of 1.01 m. When negotiating the straight parts of the track, the velocity measured by the speed magnet at the wheel coincides with the velocity of the centre of gravity. However, in the corners, the cyclist leans towards the infield of the track, resulting in an inboard shift of the CG, with respect to the contact patches of the wheels, which is a function of the CG height and the lean angle Φ . Throughout the corner, a shorter distance is thus travelled by the CG, which must be corrected. The difference between the two trajectories is illustrated in Figure 5.1.

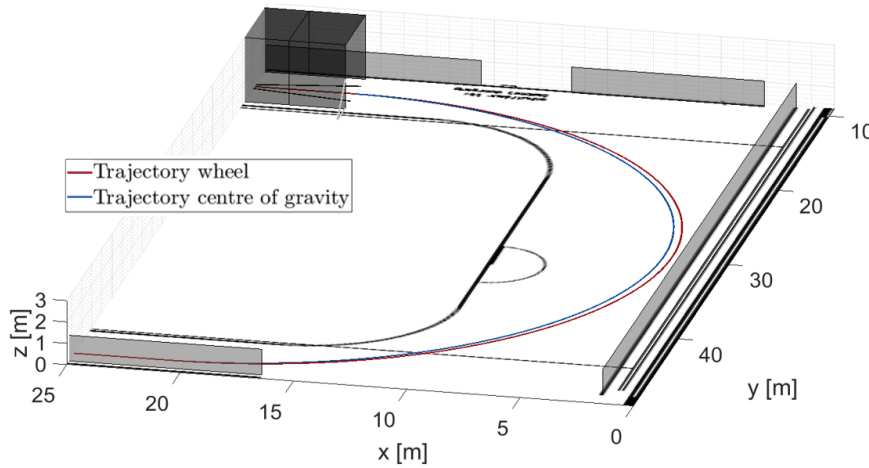
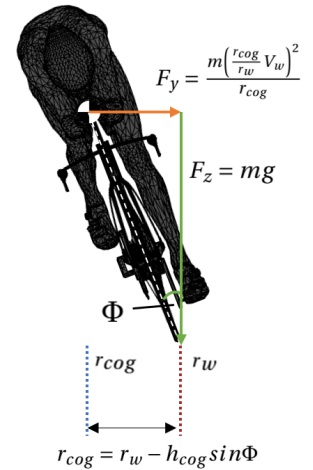


Figure 5.1: Difference in trajectory between wheel and CG

Figure 5.2: FBD during cornering to obtain lean angle Φ .

Additionally, a free-body diagram (FBD) is depicted in Figure 5.2 that enables the cyclist's lean angle Φ to be calculated through an iterative process. For this experiment, the corner radius followed by the wheels is $r_w = 17.66m$. At a test velocity of 8.33 ms^{-1} , the maximum lean angle is determined to be 21.4° , which is not reached instantaneously when entering the corner, but rather increases gradually towards the corner apex and decreases again towards the exit of the corner. This behaviour is modelled by an underlying sinusoidal function in the range of $0^\circ \leq \theta \leq 180^\circ$, representing the position in the corner. It follows:

$$\Phi(\theta) = 21.4^\circ \cdot \text{sind}(\theta) \quad (5.1)$$

The maximum difference in corner radius of the centre of gravity and the wheels is 0.37 m , obtained at the apex of the corner. To achieve a larger corner radius, the cyclist aimed to exit the corner as close to the wall as possible, which required additional steering and consequently leaning in the 10 m behind the corner to correct the lateral position on the straight. This region is modelled by assuming an average lean angle of 5° . A comparison between the corrected and uncorrected phase-averaged velocity around the track is given in Figure 5.3, where the green vertical line indicates the position of the laser sheet in the tunnel.

Figure 5.3: Phase-averaged velocity plot using data of individual upright test at 8.33 ms^{-1} .

5.1.2. RELATIVE VELOCITY

The velocity recorded by the SRM head unit represents the ground speed of the cyclist. By limiting the computation of the drag area coefficient derived from the power meter data to this ground speed velocity, it is assumed that the air mass within the test facility is quiescent. Throughout the test, it became apparent that a large-scale circulation was forming in the hall, due to the rider's motion, which acted as a tailwind component and thus reduced the relative velocity between rider and air. This phenomenon is implemented in the model by extracting the average velocity of the freestream plane, $\overline{V}_{x_{inlet}}$, acquired by the PIV system and adding it to the cyclist's velocity. The final term for the

CdA value changes then to:

$$CdA = \frac{2 \left(\eta_{drivetrain} \frac{P_{total}}{V} - C_{rr} mg - (91 + 8.7V) \cdot 10^{-3} \right)}{\rho \left(V + \overline{V_{inlet}} \right)^2} \quad (5.2)$$

Here, the sign convention of the PIV system is used for the parameter $\overline{V_{inlet}}$, which defines the velocity in the cycling direction as negative.

5.1.3. OUTLIER REMOVAL POWER METER DATA

The power and velocity traces are manually checked for outliers, such as power spikes or inconsistent velocities. In particular, the first loop of each run is excluded, as the cyclist is still gradually approaching the targeted test velocity throughout this lap. Furthermore, in order to maintain the drafting gap, the trailing cyclist had to occasionally coast. Those laps are also discarded from the data set.

5.2. DATA REDUCTION OF PIV MEASUREMENT DATA

In this section, the data reduction process for the PIV measurement data is presented, which comprises three stages, namely: image pre-processing, vector calculations and post-processing. [de Martino Norante \(2018\)](#) performed a thorough analysis of the appropriate settings used throughout the processing steps. The study is based on a seeding density of 0.004 – 0.017 particles per pixel (ppp), which is comparable to the seeding density present in the current experiment: 0.008 – 0.018ppp. The processing procedure revealed that the settings adopted from [de Martino Norante \(2018\)](#) resulted in a good compromise between resolution and robustness of the PIV data. To evaluate the particles per pixel, small regions of known dimensions are extracted from the field of view, in which the number of tracers is manually counted.

5.2.1. PRE-PROCESSING

Several pre-processing steps within the software `Davis 8.4.0` are undertaken before flow field data are drawn from the raw images. To begin with, a set of images is acquired with each camera in the absence of seeding particles in the tunnel. Other conditions, such as the shooting laser, the lighting in the hall, or the placement of objects in the camera's field of view are equal to those present during the measurements. These images then serve as background images and their intensity values are subtracted pixel by pixel from each subsequent image set recorded throughout the campaign to remove the appearance of background objects and reduce the laser glare on the PIV images.

Before the vector calculation, two additional image pre-processing routines are employed. Within the vector processing operation in `Davis 8.4.0`, the option of subtracting the sliding background is chosen. This option further improves the background removal, by subtracting the minimum intensity value found in a sliding window containing a predefined number of pixel. The window size is chosen as 10×10 px to exceed the average particle image size and thus not dampen the intensity of the tracers ([Deen et al., 2010](#)). Subsequently, a local min/max-filter, as proposed by [Westerweel \(1993\)](#), is applied to normalize the particle's intensity over a 10×10 px window size and thus balance their contribution to the cross-correlation function ([Shavit et al., 2006](#)). Non-uniform light intensities can predominantly be attributed to inconsistent particle size, but also to varying properties of the light sheet and reflections from the transiting test object.

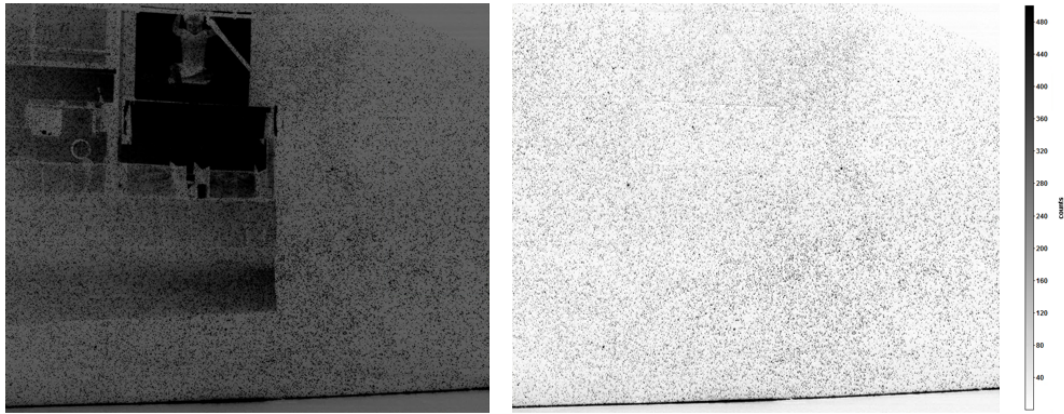


Figure 5.4: Comparison between raw image (left) and fully pre-processed image (right)

The effect of the pre-processing steps is apparent when comparing the two images in Figure 5.4. Both images show an inverted grey-scale ranging from 0-500 counts. While the laser glare, as well as objects in the background, are visible in the raw image, they are weakened or removed in the filtered image.

The signal-to-noise ratio, defined as the ratio between the highest and second highest correlation peak, is a measure of the robustness of the cross-correlation. High SNR values are desirable, as they indicate good agreement between the displacements of multiple particle pairs within one interrogation window. In Figure 5.5, a comparison is made between the signal-to-noise ratio obtained when vector processing the raw image and the filtered image. The settings used to generate the vector-processed images are identical to those presented in the upcoming vector processing text.

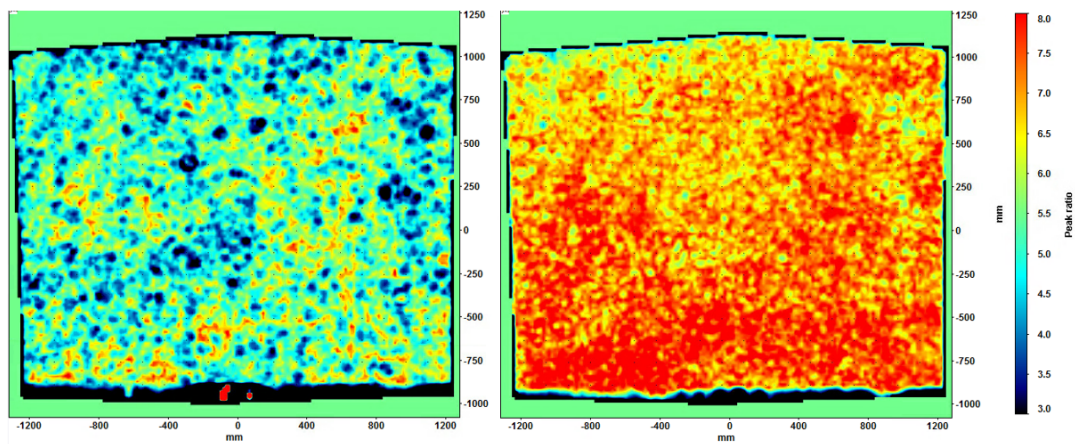


Figure 5.5: Signal-to-noise ratio for each vector resulting from the vector processing of the raw image (left) and the filtered image (right)

The importance of adequate image filtering is visible, as unwanted low SNR values are removed from the image and instead a consistently high SNR is achieved throughout the area of interest, disregarding the border regions, as they will be excluded during a masking operation at a later stage. It should be remarked that the min/max normalization filter yields the greatest enhancement of the SNR from the three pre-processing steps.

Concerning the signal-to-noise ratio in the wake region behind the cyclist, Figure 5.6 shows that the ratio between the two highest correlation peaks in the near-wake is lower than in the far-wake. The presence of the cyclist in an image, shortly acquired after the transit, mitigates the contrast be-

tween the seeding particles and the background. Together with the increased turbulence level in the near-wake region, this leads to a lower signal-to-noise ratio. Primarily recordings within 2.5 m behind the rear wheel are affected, where the SNR in the wake reaches values below 3. In the far wake, beyond 2.5 m, the SNR recovers to values of at least 3 with the majority of interrogation windows exceeding 4.

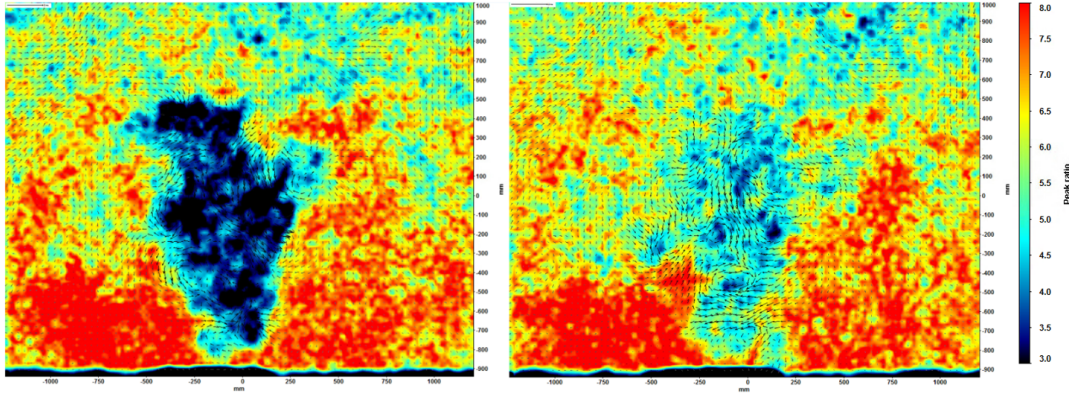


Figure 5.6: Signal-to-noise ratio for 1.5 m behind cyclist (left) and 4 m behind cyclist (right)

5.2.2. VECTOR PROCESSING

In order to extract velocity vectors from the PIV measurement, the pre-processed image pairs need to be cross-correlated. For this purpose, the domain is partitioned into smaller cells, so-called "interrogation windows", with predefined pixel count. Within each cell a correlation peak is identified, depicting the mean particle displacement between the two frames in pixel. To obtain the velocity vector in ms^{-1} , the evaluated particle image shift is multiplied by the pixel size and divided by the magnification factor M , as well as the time separation between the two acquisitions, dt . In Davis 8.4.0 the stereo-cross correlation option is selected, employing a multi-pass correlation method with decreasing interrogation window size. The interrogation windows between the image pairs are shifted according to the mean displacement recorded in the prior iteration, to increase the number of matched particle pairs and thus the SNR. Convergence between the window shift and the mean particle displacement is commonly reached after 3 passes (Raffel et al., 2007). The initial cell size is set to $96 \times 96 px$ and reduces after 3 iterations to $64 \times 64 px$, where additional 3 passes are performed. Further cell size shrinkage would lower the signal-to-noise ratio, particularly in sparsely seeded regions, as the number of correlated particles decreases. For instance, a final interrogation window size of $48 \times 48 px$ leads to an SNR decrease of approximately 1.5 compared to the image shown on the right in Figure 5.5, and even shows local regions of absolute SNR values below 3. For each iteration, the window overlap is set to 75% to enhance the spatial resolution with the given seeding density. Within one interrogation window pair, all pixel are weighted with an underlying roundly-shaped Gaussian curve, whose peak coincides with the centre of the cell. As opposed to an elliptical Gaussian weighting function, the circular distribution does not bias towards a certain displacement direction. This procedure favours the particle displacements determined from the particles located in the centre of the cells and decreases particle truncation near the edges (Wieneke, 2010).

5.2.3. POST-PROCESSING

In the post-processing stage, the universal outlier detection method introduced by Westerweel and Scarano (2005) is employed on a filter range of $5 \times 5 px$ to remove spurious vectors from the results. In the event of empty cells in the domain, Davis 8.4.0 provides the option to fill them by interpolating surrounding values. In a final step, the raw image size is cropped to exclude the edges of the

domain and the laser reflections on the ground, resulting in a rectangular image with the dimensions of 2442mm and 1944mm in horizontal and vertical direction, respectively.

With a resolution of 1.01 millimetre per pixel, the dynamic spatial range (DSR) can be obtained. [Adrian \(1997\)](#) defines this parameter to be the ratio between the largest to the smallest resolvable scale. The largest is defined by the size of the field of view, while the smallest is at least the size of the interrogation window. The minimum DSR in horizontal and vertical direction is then:

$$DSR_h = \frac{2442\text{mm}}{1.01\text{mmpx}^{-1}64\text{px}} = 38 \quad (5.3)$$

$$DSR_v = \frac{1944\text{mm}}{1.01\text{mmpx}^{-1}64\text{px}} = 30 \quad (5.4)$$

In comparison to the previous Ring of Fire experiments the DSR value is higher, due to a larger field of view and a finer pixel pitch of the sCMOS cameras. ([de Martino Norante \(2018\)](#) $DSR_v = 25$, [Spoelstra \(2017\)](#) $DSR_v = 16$).

As a second indicator [Adrian \(1997\)](#) suggests the dynamic velocity range (DVR) to assess the velocity scales that the PIV system is able to resolve. It is defined as the ratio between the largest measured velocity and the smallest. The maximum particle displacement can be obtained in the near wake behind the cyclist, in which out-of-plane velocities in the neighbourhood of -8ms^{-1} are resolved. For obtaining the smallest resolvable velocity scale, a near quiescent velocity field is considered, in which the values within one standard deviation of the mean are assigned to measurement noise. The standard deviation itself is then regarded as the smallest resolvable velocity scale and amounts in the out-of-plane component to 0.03ms^{-1} .

$$DVR = \frac{|-7\text{ms}^{-1}|}{0.03\text{ms}^{-1}} = 266 \quad (5.5)$$

A higher dynamic velocity range is obtained than in [de Martino Norante \(2018\)](#) $DVR = 250$, which may be substantiated by a higher test velocity and thus also a higher maximum velocity in the wake. In [Spoelstra \(2017\)](#) a DVR of 100 was reported. In case the author employed the same technique to acquire the smallest resolvable velocity scale, the presence of environmental winds in the outdoor test would yield a higher standard deviation, causing the DVR value to reduce.

5.2.4. OUTLIER REMOVAL PIV DATA

Similar to the power meter data, selected loops are also omitted from the PIV measurements. In particular, those that show low seeding concentration in the measurement plane, which commonly occurs in the first loops of a run, before the draft of the cyclist transports the bubbles downstream towards the laser sheet. Moreover, in the drafting configuration, loops are neglected in which the two cyclists are laterally staggered by more than 20 cm. Loops in which miscellaneous errors have occurred, such as laser blockage or corrupted data, are also discarded.

5.3. CONTOURING OF INLET AND OUTLET PLANE

This section describes the applied contouring procedure, to confine the considered region of the inlet and outlet plane within the control volume. This process serves to reduce the measurement noise and to comply with the law of mass preservation within the control volume.

5.3.1. SELECTING WAKE CONTOUR

Several steps are performed to define the wake region behind the cyclist, which are presented in the schematic [5.7](#). A sample matrix is shown underneath each step, purely for illustration purposes. The dimensions of the actual matrix are defined by the number of reconstructed velocity vectors within the PIV image and exceed the size of the sample matrix. The out-of-plane velocity in the measurement plane is shown, with negative velocity being defined in the direction of the cyclist.

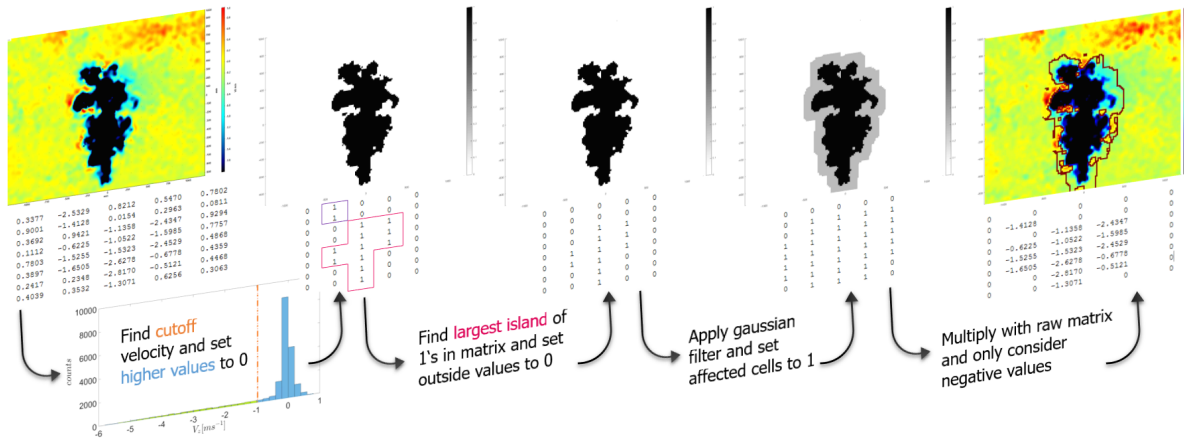


Figure 5.7: Flow schematic of contouring procedure

- **Find cut-off velocity** In the first step, a suitable cut-off velocity is defined, above which all values are set to 0. Smaller velocities than the cut-off value are set to 1. The cut-off velocity is dependent on two variables. First, one defines the wake velocity to be a certain percentage of the largest negative velocity within the plane. Instead of using the single minimum velocity value for this, a low percentile value around the *5th* is chosen. Using the percentile rather than the minimum velocity prevents the usage of outliers. As an example considering the sample matrix: The *5th* percentile is computed to be -3.266 ms^{-1} . The percentage value is chosen to be 30%, yielding a final cut-off velocity of -0.98 ms^{-1} . The two variables for the individual and drafting scenario are found by manually inspecting the wake contours. The percentage values are chosen to be 30% and 50%, respectively, while the 5th percentile within the regarded planes proved to produce good results in both cases. Due to the attenuation of the velocity deficit in downstream direction, it is important to define the cut-off value as a function of the flow field within the examined plane. The use of one fixed value for all planes would lead to excessive cutting of the wake in the far downstream planes or unnecessary inclusion of the non-wake region in the planes close to the cyclist.
- **Isolate largest island** The wake behind a cyclist can be considered as one coherent structure. This property can be utilized to filter out any regions outside the wake that show high negative velocities but are not related to the cyclist. Since the size of the rider's wake is always dominant over structures in the surrounding, the largest cluster of 1's is found in the velocity matrix. Unity values, which are not included within that group, are set to 0.
- **Dilate wake** The cut-off velocity in the first step is chosen rather stringently in order to include only those regions with a strong velocity deficit. In this step, a predefined number of 3×3 Gaussian filter operations are applied to the logical matrix, which dilates the wake region in an attempt to also include the surrounding shear layers. In the resultant matrix, cells adjacent to the "largest island" are affected by the Gaussian filter and show values above 0. To indicate their inclusion in the wake, those cells are set to 1.
- **Apply contour to original image** The previously determined filter matrix is multiplied with the velocity matrix of the raw image. This way, cells where the filter matrix is 0 remain 0 and thus do not contribute to the momentum term. Those cells that show unity value are assigned their original velocity value and therefore add to the momentum term. As a final step, positive values in the resultant matrix are set to 0 as they are not considered to be part of the wake.

An exemplary code of the previously described procedure is contained in Appendix B, creating an

$N \times N$ sample matrix.

In order to achieve satisfactory enclosure of the wake region, three values need to be adjusted based on visual inspection, namely the two variables defining the cut-off velocity, as well as the number of Gaussian filter operations. It should be noted that while this algorithm typically generates good results, occasional misinterpretations of the wake region occur, which need to be manually detected and removed from the sample pool.

5.3.2. CONTOUR ADAPTATION FOR MASS CONSERVATION

As explained in section 3.4, the control volume approach is predicated on the conservation of mass. To comply with this requirement, the inlet plane must be smaller than the outlet plane, due to the present velocity deficit in the outlet plane, under the assumption that no mass crosses the control volume through the side or top boundaries.

Two different approaches are chosen, where in the first approach, the drag area evolution downstream of the cyclist is of interest. Here, the upstream plane is fixed and different wake planes are considered. This method is used for both individual and drafting scenarios, while the second method is only relevant for drafting cases. It aims to determine the CdA evolution when examining different inlet planes and one fixed outlet plane.

Fixed inlet plane, variable outlet plane For the single rider test, a minimum of 5 planes far upstream ($> 6m$) of the cyclist are averaged. For the drafting case, one inlet plane approximately 1.5 m upstream of the trailing cyclist is considered, when investigating the CdA evolution in the wake, as will be justified later in section 5.5. In both cases, the single resultant plane serves as the freestream plane. Downstream of the cyclist the wake evolution over a distance of 10 m is of interest. Again, with reference to section 3.4, it is mentioned that the cyclist's velocity is superimposed onto the streamwise velocity distribution obtained through the PIV images to fix the cyclist in place. Due to the underlying cyclist's velocity, a broader wake structure demands more mass to pass the control volume through the inlet than a narrow wake region, as can be seen in Figure 5.8.

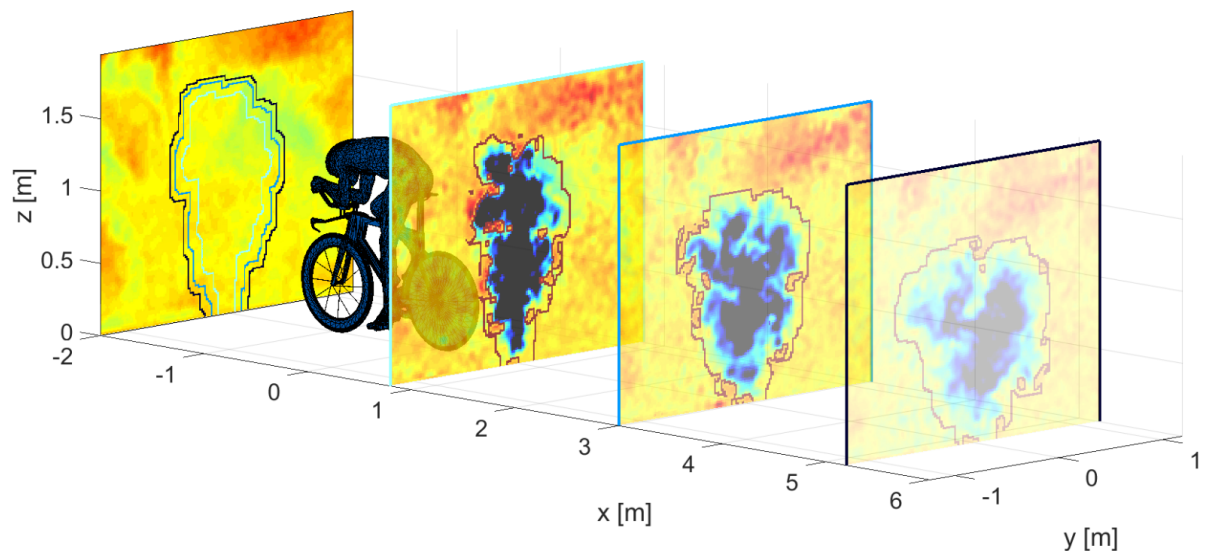


Figure 5.8: Contour adaptation of fixed inlet, variable outlet plane case (contour color corresponds to color framing the wake plane)

The initial contour of the freestream plane is the projected wake contour of the first wake plane behind the cyclist, as this is most representative of the flow the cyclist encounters when transiting

the air upstream. The contour of the inlet plane is then narrowed or broadened according to the mass flow of the outlet plane.

Fixed Outlet Plane, Variable Inlet Plane As the flow conditions behind the leading cyclist are changing rapidly, an appropriate inlet for the drafting case needs to be selected. For this investigation, the previously described approach is modified, by using different inlet planes and one fixed wake plane. For a better comparison between the inlet planes, the projected inlet contour remains unchanged and the contour in the wake plane is altered to satisfy mass preservation.

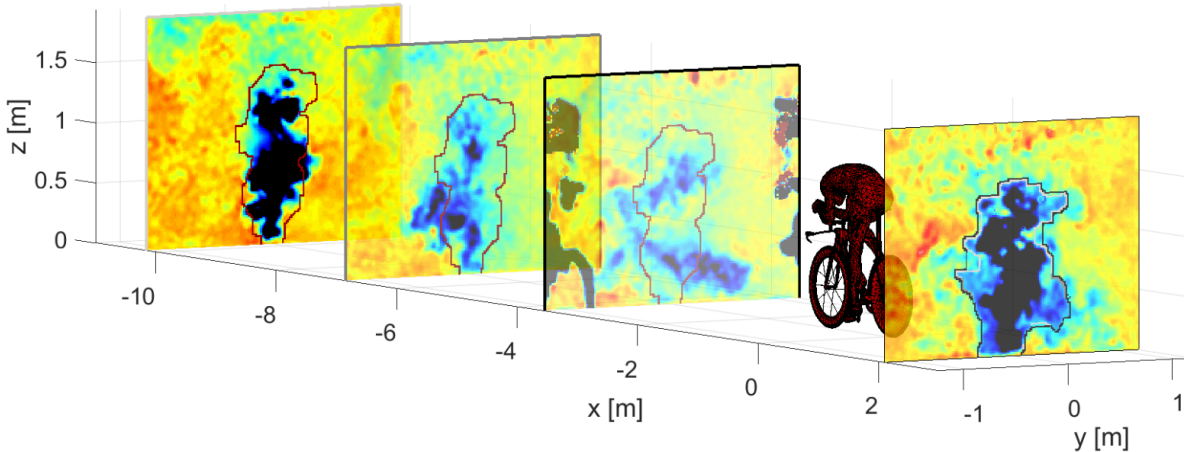


Figure 5.9: Contour adaptation of fixed outlet, variable inlet plane case (contour color corresponds to color framing the inlet plane)

As can be seen in Figure 5.9 the plane furthest upstream shows the largest velocity deficit caused by the leading cyclist. The corresponding wake contour is smallest and enlarges marginally for the inlet planes closer to the cyclist, compensating for a decreasing wake strength of the lead cyclist.

5.4. UPSTREAM PRESSURE PROPAGATION OF CYCLIST

For the drafting study, the preceding discussion included inlet planes that were located in close vicinity to the cyclist. Upstream pressure propagation from the cyclist can lead to an additional drag contribution in the control volume approach when the inlet plane is not chosen at a sufficient distance from the cyclist. Pressure reconstruction from the PIV data is not performed. Apart from the limitation that the out-of-plane velocity gradient cannot be reconstructed from stereo-PIV (van Oudheusden, 2013), the blockage of the cyclist in the PIV image causes spurious velocity field data, which make a cell-marching approach difficult. On the other hand, the expanded wake of the leading cyclist reaches the edges of the field of view, which makes it challenging to establish valid boundary conditions for the Poisson's equation used in the pressure reconstruction process.

It is therefore decided to utilize the numerically-obtained pressure coefficients of a cyclist in time-trial position from Blocken et al. (2016), in which the authors suggest a pressure coefficient (C_p) of 0.019, 1.5 m upstream of the cyclist. In the configuration shown in Figure 5.10, negligible benefits for the leading cyclist are reported and it is thusly assumed that the pressure field upstream is unaffected by the motorcycle and representative for the current study. Using an inlet surface in near proximity to the cyclist, the pressure integrated over the inlet surface yields a total drag increase of around 10 %, which should not be neglected. For the individual case, where the inlet plane is more than 6 m upstream of the cyclist, no pressure effects are taken into account, as the data from the reference study suggest an exponential decay of the C_p at increasing upstream distances. In the region between 1.5–6 m, the pressure coefficient is interpolated using the data from Blocken et al. (2016).

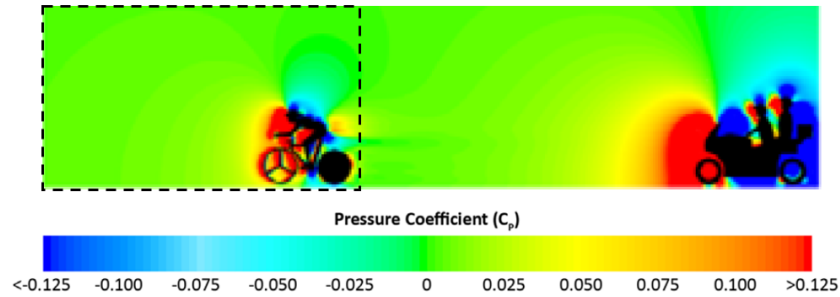


Figure 5.10: Pressure coefficient in centre line plane (Blocken et al., 2016). Box illustrates area of interest. (Gap between cyclist and motorbike is 7.5 m.)

5.5. CHOICE OF INLET PLANE UNDER DRAFTING CONDITIONS

The choice of the inlet plane for the control volume approach under drafting conditions is important, as the wake of the leading cyclist diffuses in downstream direction. Consequently, an inlet plane in close proximity to the lead rider contains a large momentum deficit, as the entire wake is concentrated within the contour bounding the inlet plane. Further downstream, the wake region grows and mitigates and will eventually exceed the contour of the inlet plane, such that the momentum deficit reduces. A study is performed where different recordings between the cyclists are used as inlet planes for the control volume around the second cyclist. This approach follows the procedure shown in Figure 5.9, where the first wake contour is projected onto the chosen inlet plane and thereby defines the flow seen by the trailing cyclist. For the outlet, the first recorded plane in the far wake is taken ($x_{rw} > 2.5m$). To satisfy mass conservation within the control volume, the wake contour of the outlet plane is modified. Figure 5.11 is limited to the drafting distances between 11–13 m for illustration purposes, measured from front wheel to front wheel and indicated as $d_{drafting}$. The sample pool consists of 16 transits, of which the average CdA value is plotted. The near wake behind the leading cyclist is represented by a dashed line and values in this region should be treated with care, as will be explained later in section 6.2. In the region between 1.5–6 m upstream of the trailing cyclist, the effects due to the pressure propagation are included according to the data fit performed with the results of Blocken et al. (2016). Velocity fields closer than 1.5 m cannot be employed due to the field of view blockage caused by the incoming cyclist. In Figure 5.11, the dashed line illustrates the distance between the last "freestream" image and the position of the trailing cyclist.

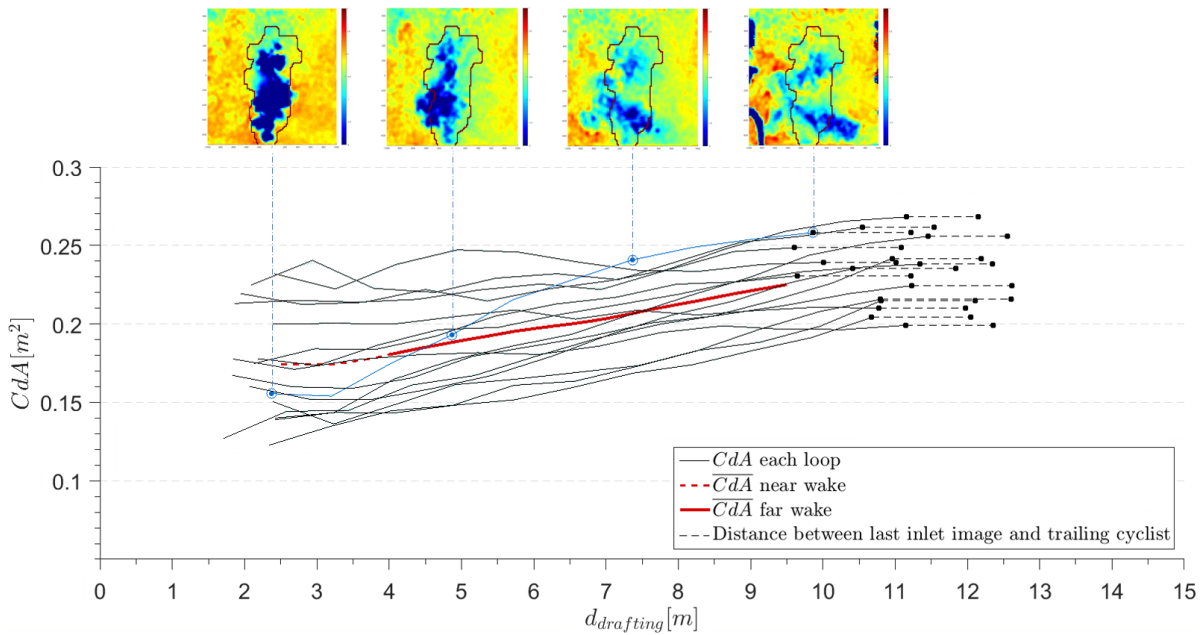


Figure 5.11: Effect of inlet plane choice on the CdA value for trailing cyclist at 11–13 m drafting distance. Images above show out-of-plane velocity, ranging from -2 to 1 m s^{-1} , together with the applied contour

From the previous plot, it can be observed that the overall trend shows an increase of the mean drag area value at inlet planes closer to the trailing cyclist. Four "freestream" flow fields along the downstream direction are shown in Figure 5.11, which provide an example of the diffusion process. In the first picture, the entire wake of the lead cyclist is enclosed by the contour and thus considered for the control volume approach. In the following images, the intensity of the wake core reduces and turbulent diffusion processes encourage the surrounding flow to be entrained. This leads to a decreasing velocity deficit within the inlet plane contour, an overall increased momentum deficit and subsequently an increase in CdA . The final image shows the silhouette of the incoming cyclist. It has to be manually checked that none of the blocked regions are inside the contour, as this would cause a high level of inaccuracies. The most representative incoming flow field is chosen to be the final recording that is not closer than 1.5 m to the trailing cyclist. Using a more upstream location would otherwise lead to an under-prediction of the drag area value due to the increased velocity deficit. It is therefore decided to use the 1.5 m upstream location as inlet plane for the upcoming analysis of the CdA evolution in the wake of the trailing cyclist in section 6.2 and use the data from Blocken et al. (2016) to correct for the presence of upstream pressure propagation.

5.6. LONGITUDINAL WAKE ALIGNMENT

In order to draw conclusions about the streamwise drag evolution behind the cyclist between a series of loops, it is necessary to know the precise distance of the acquired wake planes behind the cyclist. By definition, the wake images capture the flow field after the entire cyclist has passed through the laser sheet. Due to a non-constant velocity of the cyclist and an inconsistent trigger delay, the time between transiting the photo-detector and leaving the measurement plane varies. Consequently, the cyclist's position is slightly different at each transit. For the upright case, a test velocity of 8.33 m s^{-1} was targeted. Considering 57 loops, the velocity at the passage of the laser sheet is on average 8.24 m s^{-1} , with 8.01 m s^{-1} and 8.48 m s^{-1} being the minimum and maximum-recorded velocities, respectively. The velocity of the passage is determined by utilizing the acquired velocity data of the bike computer and averaging those over a 3 s time interval centred around the transit of the measurement plane.

In the following reference case, the number of recorded images between triggering the photo-detector and exiting the laser sheet is assessed. The total travelled distance by the cyclist ($d_{total} = d_{phd-laser} + l_{bike}$) amounts to $13.2m + 1.666m = 14.866m$. Using the minimum and maximum-recorded velocity, this distance is covered in a time of either 1.856 s or 1.75 s, respectively. In addition, a non-constant time delay of 5–70 ms is estimated by the acquisition software Davis 8.4.0 between the triggering and the recording of the first image. Given a recording frequency of 15 Hz the PIV system acquires an image every 0.066 s. In the worst case, when both uncertainties, introduced by the velocity and the time delay, are combined, the cyclist could exit the plane after 25.45 acquired images or after 28.05. The maximum longitudinal positioning error results then in 2.5 images, which justifies a correction procedure. It should be noted that setting a pre-defined time delay does not eliminate the triggering uncertainty and moreover only affects the number of images acquired until the transit is completed, not the relative error of 2.5 images between the two cases.

To relocate the wake images in streamwise direction with respect to the rear portion of the back wheel, the last image in which the cyclist intersects the laser sheet is considered. Here, the longitudinal position, d_{inter} , of the intersecting laser sheet on the bike is determined. Using a side view image of the bike the distance with respect to the most upstream point on the front wheel can be measured. Given the bike length l_{bike} , the cyclist's velocity V and the acquisition frequency f of the PIV system, the location of the first wake plane w.r.t the rear wheel, $d_{\#1}$, can be obtained, as well as the distance of each subsequent image $d_{\#n}$. A schematic of this process is given in Figure 5.12.

$$d_{\#1} = \frac{V}{f} - (l_{bike} - d_{inter}) \quad (5.6) \quad d_{\#n} = d_{\#1} + (n-1) * \frac{V}{f} \quad (5.7)$$

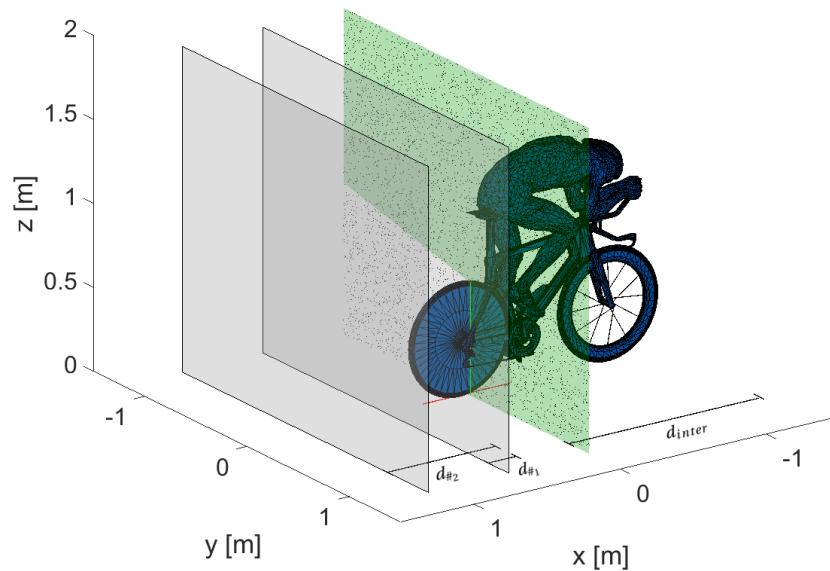


Figure 5.12: Streamwise relocation of wake planes with respect to the rear portion of the rear wheel

5.7. DETERMINATION OF DRAFTING DISTANCE

Throughout the drafting experiments, the distance between the riders needs to be measured. In accordance with the official rules stated in UCI (2018), the drafting distance between two riders is

measured from the front wheel of the leading cyclist to the front wheel of the trailing cyclist. Two different approaches were used to obtain this distance, which are presented below.

5.7.1. DRAFTING DISTANCE EXTRACTED FROM VIDEO

The first approach relies on extracting images from a video recorded by a DSLR camera, capturing both cyclists in side view. The uncropped field of view of this camera ranges from 18.2 m upstream of the tunnel entrance to the beginning of the tunnel itself. As mentioned in section 4.1, the resolution of the video was set to $640\text{px} \times 480\text{px}$ to keep the file size small for video lengths of approximately 20 min. This choice negatively affects the quality of the extracted image, which needed to be desaturated and further processed to enhance the contrast within the image. Figure 5.13 shows one of the filtered images in cropped form. For this approach, it is assumed that the cyclists are aligned with each other in streamwise direction. A reference length in that same x-z plane is taken between the entry of the tunnel and the photo-detector, which is known to be 8.2 m. Measuring the pixel length of the dashed line with the image processing ImageJ software, one can determine the pixel to meter conversion of the image, which is then applied to the drafting distance, represented by the solid line. Since the bicycles' disc wheels provide a good contrast against the white background, it is decided to measure the distance between the two most rearwards points of each bike. To be consistent with the UCI definition, which is defined between the front wheels, the difference in bike lengths between the leading female and trailing male bike needs to be subtracted from the resulting distance.

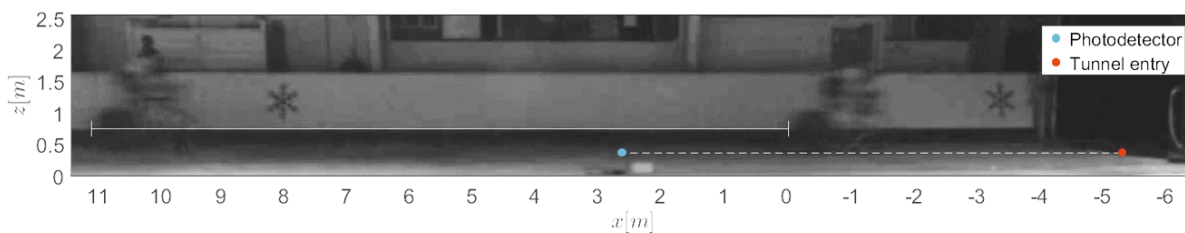


Figure 5.13: Cropped and filtered image extracted from video, capturing side view of the cyclists before entering the tunnel

The drawback of this approach is the spatial and temporal separation between capturing the image to measure the drafting distance and the actual PIV acquisition. The separation distance between the cyclists would only remain constant if the velocity of both cyclists were exactly the same. The velocity recordings of the trailing cyclist show an almost constant velocity in the region of the measurement plane. However, no velocity data are available of the leading cyclist, which entails an uncertainty.

To assess the possible error caused by a difference in velocity of the two riders, a case study is performed employing the data obtained in the 12 m drafting test, which is aimed at a test velocity of 8.33 m s^{-1} . Averaging the velocity of the trailing cyclist over the 3 s time interval centred around the transit of the laser sheet amounts to 8.35 m s^{-1} , with a standard deviation of 0.137 m s^{-1} . The photograph, as seen in Figure 5.13, shows the trailing cyclist approximately 22 m upstream of the laser sheet. For each transit velocity the time is computed, in which the trailing cyclist covers those 22 m to reach the measurement plane, where the drafting distance is of interest. The minimum and maximum distance travelled by the leading cyclist within this time span is computed using the velocity from the trailing cyclist plus minus the standard deviation of 0.137 m s^{-1} . The resultant upper and lower bounds are calculated for each transit and are displayed in Figure 5.15.

5.7.2. DRAFTING DISTANCE EXTRACTED FROM PIV IMAGES

In the second selected ansatz, the acquired PIV images are employed. Similar to the procedure explained in section 5.6, the image set is searched for the last capture of the leading cyclist intersecting the laser plane, $\#I_1$. Additionally, the first image showing the pursuing cyclist traversing the measuring plane is of interest, $\#I_2$ (see Figure 5.14). At these two locations in the image set, the location of the intersection on the bike with respect to the front portion of the front wheel is manually determined. Together with the bike's length of the leading cyclist, the recorded test velocity and the acquisition frequency of the PIV system the drafting distance between the two front wheels can be determined through the following formula:

$$d_{drafting} = \frac{(\#I_2 - \#I_1) V}{f} - (l_{bike_1} - d_{inter_1}) - d_{inter_2} + l_{bike_1} = \frac{(\#I_2 - \#I_1) V}{f} + d_{inter_1} - d_{inter_2} \quad (5.8)$$

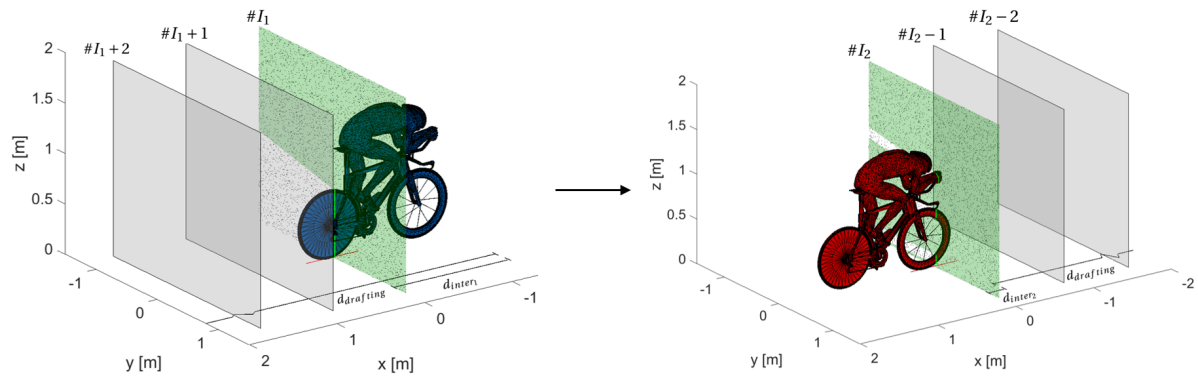


Figure 5.14: Last image of leading cyclist (left) and first image of trailing cyclist (right) traversing the laser sheet at two different time stamps

Similar to the preceding video approach, the drafting distance measurement does not temporally correspond with the PIV measurement. The drafting distance is measured over a time interval, between the acquisitions of planes $\#I_1$ and $\#I_2$. In an ideal scenario, both cyclists follow the same velocity and the true drafting distance would be found. However, in case the velocities are different, the relative position of the cyclists' alters. To assess the uncertainty, the conditions of the previous reference case are revisited using the data from the 12 m drafting case at 8.33 m s^{-1} . The time difference of arrival at the laser sheet between the two cyclists can be obtained with:

$$t = \frac{(\#I_2 - \#I_1)}{f} + \frac{d_{inter_1} - d_{inter_2}}{V} \quad (5.9)$$

Again, the velocity of the trailing cyclist is adapted for the leading cyclist plus minus one standard deviation of 0.137 m s^{-1} . Within this time interval t the two cyclists then cover different distances and thus the spatial separation between the cyclist at the time of the laser sheet transit of the trailing cyclist has changed. The measured drafting distances using this approach, together with the uncertainties are presented in Figure 5.15.

5.7.3. DRAFTING DISTANCE MEASUREMENT TECHNIQUE COMPARISON

In the following plot 5.15 the two previously described approaches are applied to the 12 m drafting case with an aimed test velocity of 8.33 m s^{-1} . In total, 31 loops are included in this comparison, while throughout 8 loops in the middle of the run, no PIV images were acquired from the first cyclist because the PIV system was triggered by the second rider. The remaining loop was disregarded due to a non-constant velocity of the trailing cyclist in the measurement region.

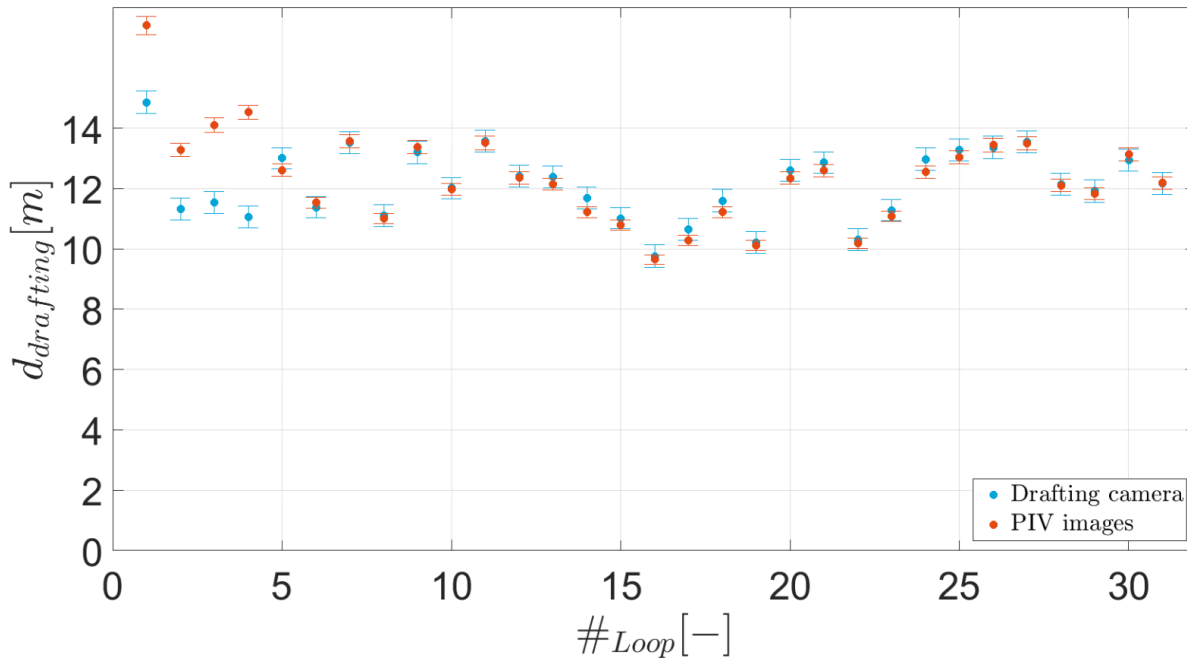


Figure 5.15: Comparison between the two approaches based on the video and the PIV images, respectively

The preceding Figure shows discrepancies between the two techniques within the first four loops of the run. During this time, the two riders had to find a steady rhythm by approaching the correct drafting distance while reaching and maintaining the aimed test velocity, which caused fluctuations in the drafting distance. Beyond loop 4, the results between the two approaches are in good agreement. Due to the longer time between the drafting distance measurement and the transit of the laser sheet, the video approach shows a larger uncertainty. It is therefore decided to proceed with the PIV-image based technique as primary source of the drafting distance, but to confirm the results with the data obtained through the video method.

5.8. SYNCHRONIZATION OF THE DATA ACQUISITION SYSTEMS

In order to assess the measured drag difference between the Ring of Fire and the power meter, both systems must be synchronized in time. Unfortunately, the system time stamp between the acquisition computer and the power meter did not coincide, requiring manual effort to match the two data sources. For this, an externally recorded video is used showing the initial acceleration of the cyclist from standstill up to the point where the laser is triggered for the first time. The time duration between the two events amounts to 16 s, according to the video. In the power meter file the time stamp representing the start of the run can be easily identified, from which the time stamp of the first laser sheet transit can be derived by adding 16 s. As a final step, the derived power meter time stamp of the transit is compared with the PIV acquisition time stamp of the first passage. A constant time offset of 2 min 20 s between the two systems is found, which needs to be corrected. Likewise, the snapshots captured with the drafting camera must be manually linked to the corresponding PIV acquisition.

6

RESULTS AND DISCUSSION

The forthcoming chapter discusses the results of both the power meter and the Ring of Fire measurement techniques, obtained in the campaign conducted within the framework of this project. Sections 6.1 and 6.2 discuss the CdA results of the power meter and the Ring of Fire individually, before a comparison between the two approaches is drawn in section 6.3. Thereupon, the drag savings under drafting conditions are discussed in section 6.4. The chapter is concluded with an examination of the flow conditions encountered upstream and downstream of the trailing cyclist (section 6.5).

6.1. POWER METER RESULTS

To begin with, the power meter (PM) data are presented in the following section, which are fed into a model to isolate the aerodynamic drag from the other resistances. The rolling coefficient is one of the model constants and its evaluation is given below. Furthermore, a phase-averaged data plot around one lap is depicted in Figure 6.2, before the resulting drag area values for the different test cases are presented in Figure 6.3.

6.1.1. LINEAR REGRESSION ANALYSIS FOR C_{rr} VALUE

Second to aerodynamic drag, rolling resistance is the next largest opposing force when cycling at steady velocity on level ground. To evaluate its contribution to the current experiment the linear regression method from Debraux et al. (2011), as described in section 3.2, is utilized. For this test, the cyclist maintains a constant posture and rides 10 loops as close as possible to target velocity, which is increased in steps of 3 km h^{-1} ranging from $15\text{--}33 \text{ km h}^{-1}$. Figure 6.1 plots the scalar values of the total resistive force against the square of velocity. All data are extracted from the power meter recordings. Each circle in the upcoming figure represents the average value over one loop.

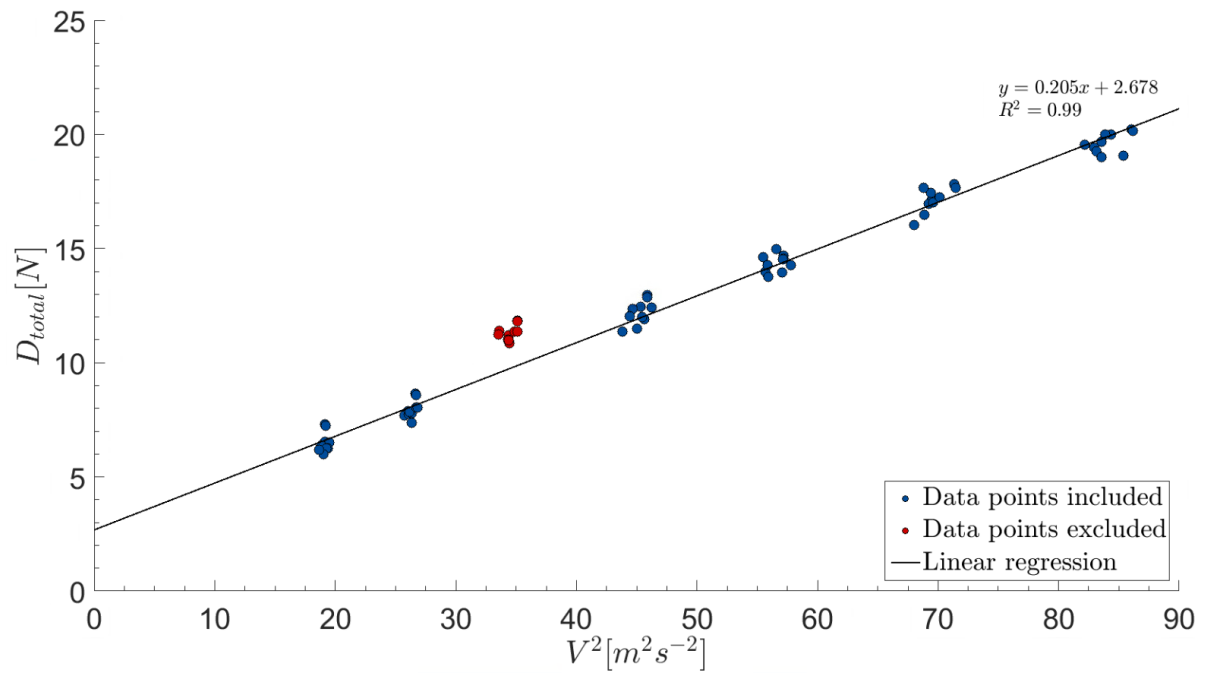


Figure 6.1: Linear regression to determine C_{rr} . Data recorded at velocities of 15–33 km h⁻¹ in steps of 3 km h⁻¹

The preceding Figure illustrates an outlier behaviour of the recordings taken at 21 km h⁻¹. The cause of this is after investigating the data traces still unclear but might be assigned to an inconsistent posture of the cyclist. Ultimately, it is decided to discard the third measurement block and perform the linear regression with the remaining data. The y-intercept of the resultant straight is found to be 2.678 N, with a slope of 0.205 kg m⁻¹ and a coefficient of determination of 0.99. Despite a good linear regression fit, the determined C_{rr} value of 0.003 is low compared to literature. At 5 bar inflation pressure a rolling resistance coefficient in the range of 0.005–0.006 is suggested by [Grappe et al. \(1999\)](#) and [Wilson et al. \(2004\)](#). In the following power meter analysis, it is decided to continue with the literature based value of $C_{rr} = 0.0055$. However, the rolling coefficient derived from the linear regression procedure is revisited when comparing the power meter data to the Ring of Fire data in section 6.3, to assess the importance of a correctly chosen C_{rr} value for the absolute CdA value.

6.1.2. PHASE-AVERAGED POWER METER DATA

The power meter data of all runs are post-processed, using the model described in section 5.1 to obtain instantaneous drag area values. Given the velocity and the time stamp of the laser sheet passage, the phase-locked traces of velocity, power, cadence, and drag area value around the track can be created, which are shown in Figure 6.2 for the individual upright measurements. Besides the instantaneous traces of each loop, the mean value of all loops is included. The x-axis origin in this plot represents the location on the back straight, which is exactly half a lap away from the laser sheet. The southern-facing corner is negotiated before entering the tunnel, while "Corner North" is located behind the tunnel.

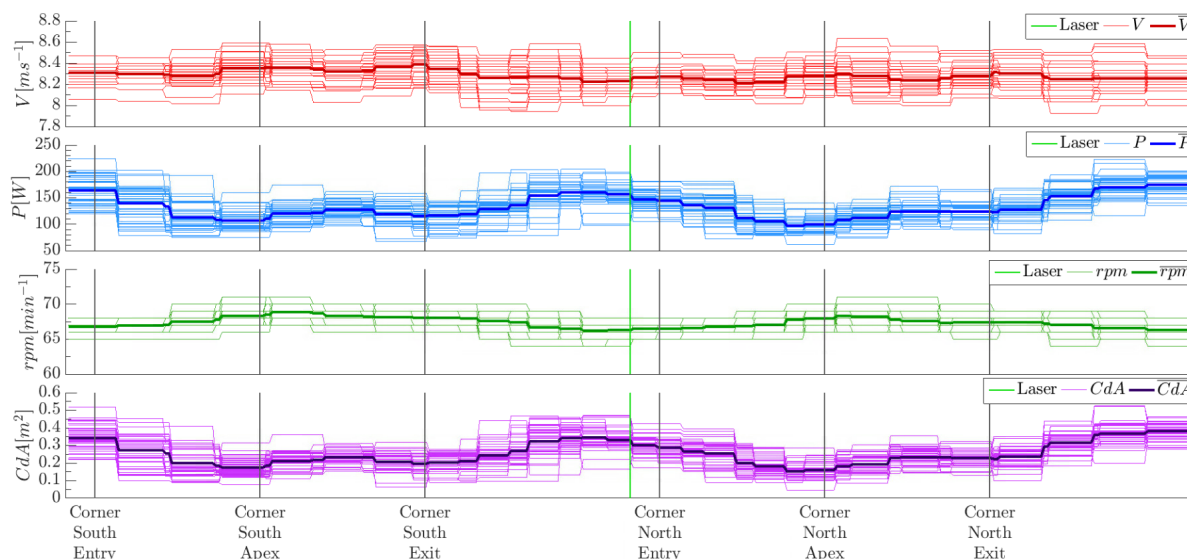


Figure 6.2: Phase-locked velocity, power, cadence, and drag area traces over one lap. Data from 30 km h^{-1} upright individual test

From the previous image, it becomes apparent that while the velocity and cadence trace can be regarded as near constant, the power and subsequently the drag area curve throughout one lap cannot. The cyclist evidently outputs less power in cornering than on the straights. This observation is in line with [Olds et al. \(2001\)](#) and [Lukes et al. \(2012\)](#). The latter reports that professional cyclists in a velodrome have a subjective feeling of riding downhill in corners and uphill on straights. Given the corner radius and the cyclist's velocity, an average yaw angle of 1.35° is determined, at which aerodynamic benefits in the range of 0–2 % are found ([Barry et al., 2012](#)). On the other hand, [Kyle \(2003\)](#) reports an overall drag increase in cornering conditions due to tyre scrubbing between 0.4–2.9 % as a function of the steering angle. The two previous phenomena counteract each other, which makes their resultant effect small and therefore cannot be the cause of the power fluctuations as observed in Figure 6.2. One possible source of error might be an underestimation of either the bank angle or the centre of gravity height, which in turn would lead to a shorter corner radius of the (CG) itself. As a result, the CG would travel slower in the corners than on the straights and inertial effects due to acceleration at the exit of the corner and deceleration at the corner entry could cause the fluctuating behaviour of the power trace. However, during the experiment, neither the centre of gravity height nor the bank angle was accurately determined. It is therefore decided to eliminate possible inertial effects by averaging the velocity and power values over one lap, where the number of acceleration and deceleration phases is equal and thus cancel each other. The lap-averaging-method is a common approach when aerodynamic tests are conducted in a velodrome to assign CdA value to cyclists, as applied by [Grappe et al. \(1997\)](#), [Broker et al. \(1999\)](#) and [Garcia-Lopez et al. \(2013\)](#).

6.1.3. CdA VALUE FROM POWER METER

The previously described lap-averaging-method is employed to the different runs, performed throughout the measurement campaign. Loops at the beginning of each run are excluded, as the target velocity has not been reached. Furthermore, laps with high power fluctuations or inconsistent pedalling are also discarded, which occur mostly in the drafting scenario, while the trailing cyclist is managing the separation gap to the leading rider. Figure 6.3 shows the resultant drag area coefficient for the male athlete when riding solo and under drafting conditions behind the female rider, obtained from equation 3.6. Initially, only two distinct drafting distances of 8 m and 12 m were tar-

geted. However, due to widespread of drafting distances over all laps, 4 zones are defined dividing the range of drafting distances from 7–15 m in steps of 2 m. As mentioned in table 4.1, the drafting experiment is conducted in time-trial (TT) posture, while the cyclist is wearing the road helmet. In order to determine the CdA value, the wind speed relative to the cyclist needs to be known. In addition to the cyclist's velocity, as recorded by the head unit, the average velocity in the PIV plane upstream of the cyclist is considered. This accounts for both the tail-wind velocity component induced by the large-scale circulation in the hall and the encountered velocity deficit under drafting conditions.

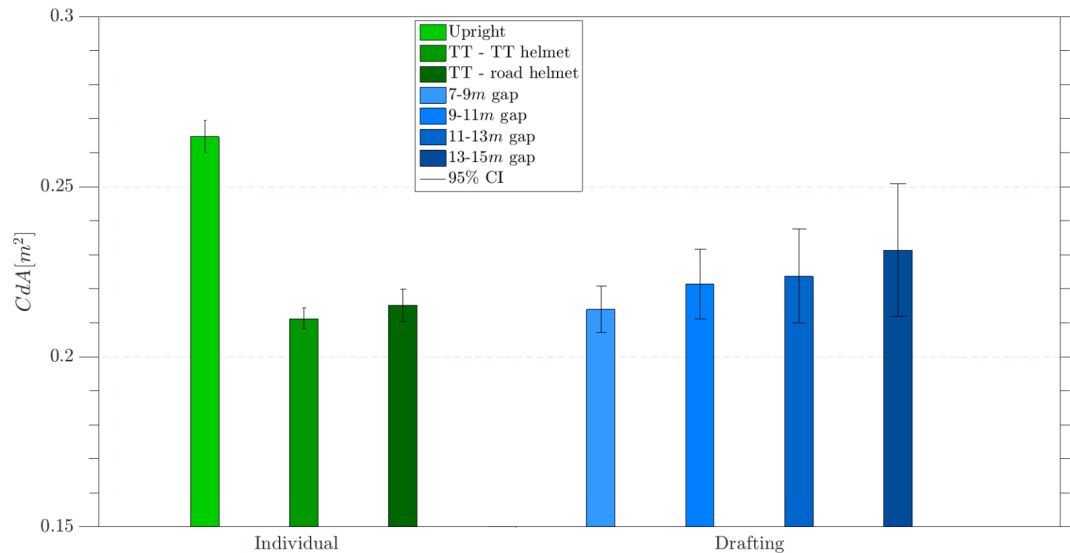


Figure 6.3: Drag area coefficient derived from power meter results. Drafting tests were conducted in time-trial posture with a road helmet

For the individual test series, the previous plot confirms two trends reported by literature, namely a decrease in drag area value, when comparing the time-trial posture against the upright posture (Gibertini and Grassi (2008) and Barry et al. (2014b)) and a smaller-scale CdA increase when comparing the road helmet against the time-trial helmet (Alam et al. (2010), Blair and Sidelko (2009) and Chowdhury et al. (2014)). It can furthermore be said that the 95 % confidence intervals for the individual case depict a range of maximum 0.01 m² and thus show high reliability. Contrarily, the resultant CdA values from the drafting experiments show a large uncertainty, which can have several reasons. Firstly, the number of samples in the 4 zones with increasing drafting distance are: 20, 15, 12 and 9, whereas on the other hand, each individual run consists of at least 40 samples. Secondly, the drafting distance is derived from one local measurement, namely at the laser sheet plane. Throughout the lap, this distance can vary and cause the resultant drag area values to be more widespread. Finally, the effect of the drafting effect during cornering is unknown and it can be questioned whether the trailing cyclist experiences the same velocity deficit or if the leading cyclist's wake is carried outwards. It is because of the aforementioned reasons that the CdA values obtained in the drafting experiment should be regarded with care. A general trend towards lower drag area values at smaller separation distances can be observed. Unexpectedly, the drafting cases beyond 9 m show a higher drag area coefficient than the individual case under equal time-trial position and using the same road helmet. However, the individual case still falls well within the large confidence interval of the drafting cases and no conclusion should be drawn from this. The discussion about the drag area values is continued in section 6.3, when the Ring of Fire data are added. There, the exact drag area values for each test are also presented in table 6.2.

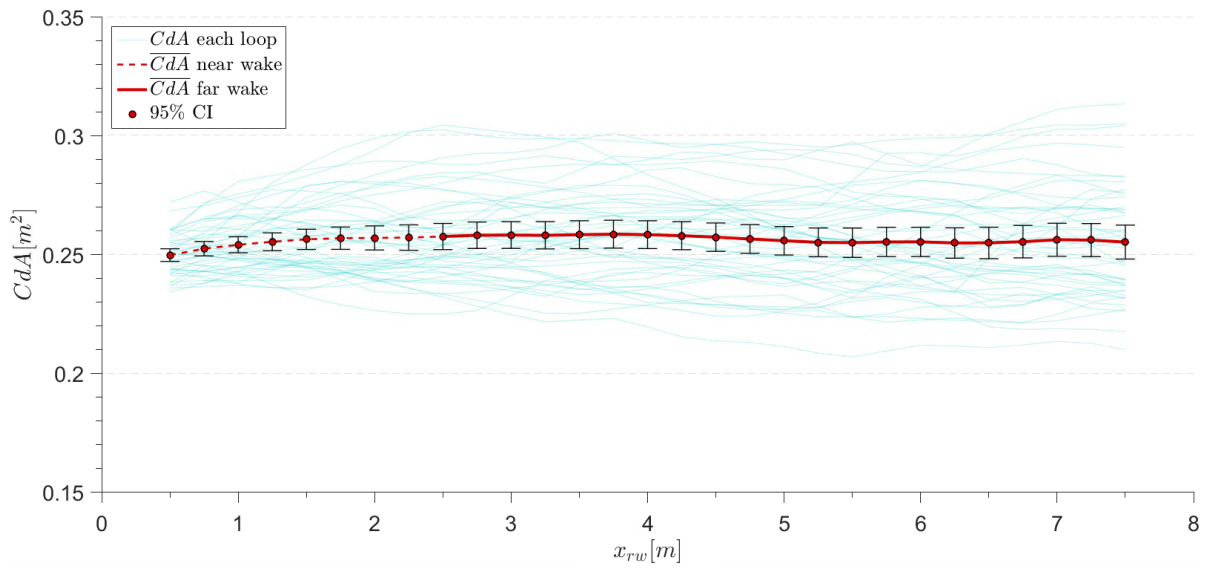
6.2. RING OF FIRE RESULTS

In the following section, the Ring of Fire results are presented, obtained from the control volume approach introduced in section 3.4. First, the drag area values of the three single-rider tests are presented before the drafting scenario is considered. Concerning the drafting related results, the drag area evolution in the wake of the trailing cyclist is examined.

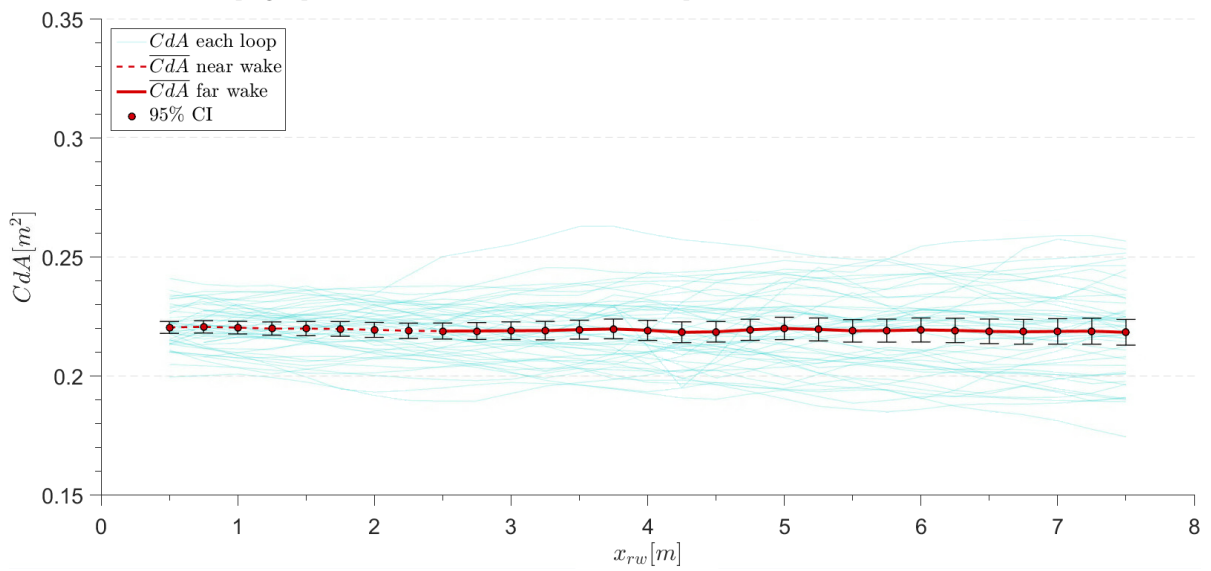
6.2.1. CdA VALUE FROM INDIVIDUAL TESTS

The individual measurements were conducted by the male athlete on the first of the two main testing days. Three separate runs were performed, starting with the cyclist in upright position with his hands on the brake hoods while wearing the time-trial helmet. For the next measurement, the cyclist changed into the time-trial position, while the helmet model remained unchanged. The last test was again carried out in time-trial posture, but the time-trial helmet was replaced by a road helmet. Under each test setting, at least 50 laps were negotiated. From the total 170 transits in the individual test, approximately 9 % had to be excluded due to improper wake enclosure by the applied wake contouring procedure, as described in section 5.3. Some of these failures can be assigned to cases where the wake splits up and the algorithm only considers the largest wake structure. The other misinterpretation occurs when the wake structure merges with non-wake high-velocity fields, which is predominantly an issue in the far wake, where the peak velocity deficit in the wake and subsequently the cut-off velocity of the algorithm is approaching the velocity of the surrounding air mass. Further, 6 % of the passages needed to be discarded, due to insufficient seeding. Finally, 4 % of the PIV data set was not processed due to miscellaneous events, such as blockage of the laser, corrupt data, or poor positioning of the cyclist. Overall 81 % of the acquired PIV data is used for the following analysis.

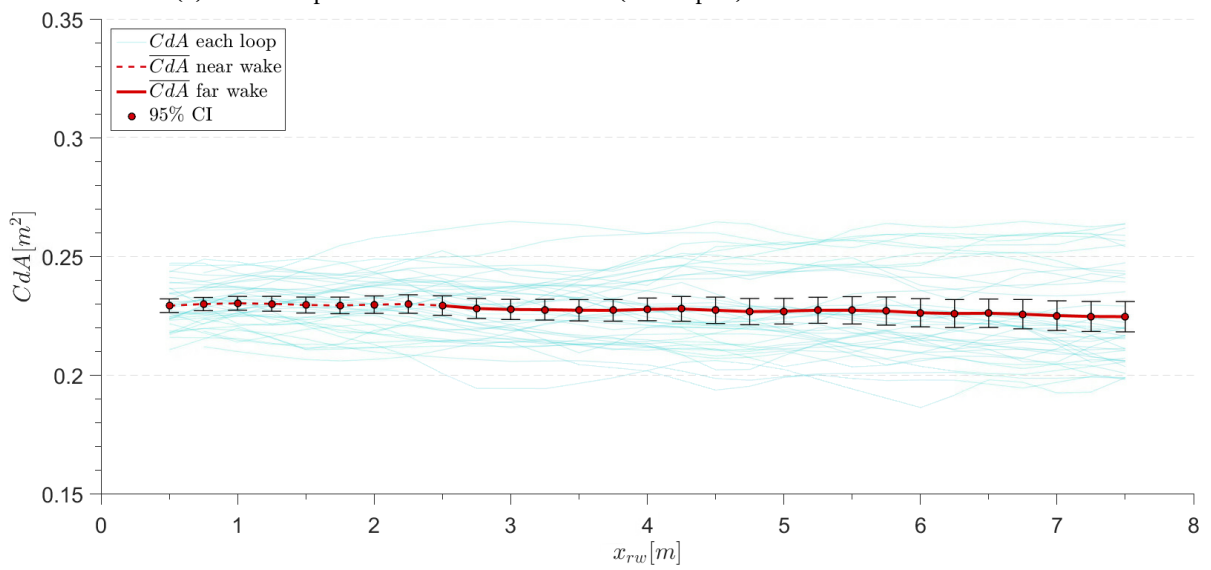
The choice of inlet plane follows the discussion of section 5.3, where 5 inlet planes far upstream, beyond 6 m, are averaged and the first wake contour is projected onto the resultant plane, which describes the considered inlet area. Similarly, the applied wake contouring encloses the considered area in the outlet planes. The wake is divided into two zones, namely the near and the far wake. In the near wake zone, within five characteristic length scales behind a sphere, pressure effects cannot be disregarded according to Terra et al. (2017). This is a conservative approach, as Shah (2017) reports no pressure effects beyond 0.8 m behind a cyclist, with respect to the saddle. Pressure reconstruction was not performed for this experiment due to the inability of a stereo-PIV setup to obtain the out-of-plane velocity gradient, which consequently introduces an error in the planar pressure field of highly three-dimensional flow (van Oudheusden, 2013). As a characteristic length, the shoulder width of the cyclist is measured to be $w_{shoulder} = 0.47\text{ m}$, which amounts to a pressure affected region of 2.35 m following Terra et al. (2017). During the experiment, no predefined crank-angle was chosen for the laser sheet transit. However, according to de Martino Norante (2018), the information of the pedal position is lost in the far wake due to mixing of the flow. Following the previous arguments and the discussion about the reduced SNR in the near-wake region (Figure 5.6), it is decided to limit the CdA computation to the region of the far wake, which is indicated by a solid line in the upcoming Figure 6.4. Additionally, the near wake is included as dashed line, together with the drag area evolution of each transit, measured from the most rearward point of the rear wheel x_{rw} .



(a) Upright posture with time-trial helmet (46 samples) - \overline{CdA} in far wake: $0.2565 m^2$



(b) Time-trial posture with time-trial helmet (49 samples) - \overline{CdA} in far wake: $0.2183 m^2$



(c) Time-trial posture with road helmet (42 samples) - \overline{CdA} in far wake: $0.2268 m^2$

Figure 6.4: Streamwise CdA evolution in wake of individual cyclist at $30 km h^{-1}$

The preceding Figure 6.4 shows the results of the three individual tests. The evaluated mean drag area values in the distant wake between 2.5–7.5 m are once more averaged to obtain a single representative CdA number. Beyond 7.5 m the diffusive process of the wake makes it increasingly difficult to accurately define a contour in the outlet plane including both, the wake and the shear layers. This trend is already noticeable in all three plots of Figure 6.4, where the dispersion of the CdA measurements per loop and consequently the 95 % confidence interval grows at large distances behind the rear wheel. At the same time, the spread in the near wake is smallest, as the contour of the wake structure is easily identifiable with the used algorithm. In all three tests, the drag area coefficient remains rather constant throughout the wake region, which is contrary to the previous two Ring of Fire experiments, where a lower drag area value in the near wake gradually increases in downstream direction until it plateaus in the far wake. [de Martino Norante \(2018\)](#) assigns this behaviour to the underestimation of the reconstructed pressure. The pressure effects behind the cyclist in upright position can be considered small (Figure 6.4a) and negligible in time-trial position based on the near-constant CdA evolution in downstream direction, which would be in agreement with [Shah \(2017\)](#).

For the upright case, shown in Figure 6.4a, the computed CdA amounts to 0.2565 m^2 , with a probability of 95 % that a repeated experiment would result in a mean drag area value that falls within the range of $\pm 0.0061 \text{ m}^2$ around 0.2565 m^2 . For the time-trial position the drag area coefficient reduces for the time-trial helmet down to 0.2183 m^2 (Figure 6.4b), and for the road helmet to 0.2268 m^2 (Figure 6.4c) with a 95 % confidence interval of $\pm 0.0046 \text{ m}^2$ and $\pm 0.0053 \text{ m}^2$, respectively. Compared to the previous Ring of Fire campaigns conducted by [de Martino Norante \(2018\)](#) and [Spoelstra \(2017\)](#), the 95 % confidence intervals in the wake are narrowed, from ± 2.7 – 5.3 % and ± 5 %, respectively, down to ± 2.1 – 2.3 % in the current measurement. This is likely due to a 1.5 – 2 times larger sample pool with respect to the experiment conducted by [de Martino Norante \(2018\)](#) and a 4 times larger sample size compared to the first Ring of Fire test by [Spoelstra \(2017\)](#). Additionally, the implemented wake contouring procedure disregards the surrounding flow field and thus reduces the induced noise, which yields less dispersed drag area values.

6.2.2. CdA VALUE FROM DRAFTING TESTS

On the second main testing day, the drafting experiment was carried out, where the female rider was assigned the lead role, while the male cyclist followed her in a predefined distance. As already mentioned in section 6.1, the drafting distance measured between the front wheel of the cyclists varied considerably, such that 4 zones in steps of 2 m between 7–15 m are investigated rather than two distinct drafting distances at 8 m and 12 m, as initially planned. Similarly to the individual test, the near wake flow field at less than 2.5 m behind the cyclist is not considered. As established in section 5.5, the control volume approach utilizes the next available inlet plane beyond 1.5 m in front of the trailing cyclist, which is then modified according to the contoured wake of the outlet plane to satisfy mass conservation. In total, 90 laps were negotiated during the drafting experiment. Regrettably, two periods of 20 and 6 consecutive laps had to be discarded due to insufficient seeding within the measurement plane, which consequently led to low signal-to-noise ratios in the PIV images. In total, 27 of the 90 laps showed seeding issues, while in 7 passages the lateral alignment between the two riders was poor and exceeded 200 mm. The observed drag area value in those passages is increased and is excluded from the data pool, as it is not representative of the targeted in-line drafting configuration. However, it underlines the result from [Kyle \(1979\)](#) and [Zdravkovich et al. \(1996\)](#), which report a decreased drafting effect in staggered arrangement, albeit the maximum longitudinal separation between the riders was only 0.3 m and 0.9 m, respectively. Finally, 5 further transits needed to be removed due to excessive wake contouring. Contrary to the individual run, the percentage parameter defining the cut-off velocity in the algorithm is increased from 30 % to 50 %,

which results in a more stringent wake contouring. This is necessary to avoid enclosure of the wake originating from the lead cyclist, as it is still present in the wake planes behind the trailing cyclist. In total, 51 of the 90 acquisitions could be used for this analysis. Figure 6.5 plots the downstream evolution of the drag area coefficient for the four zones.

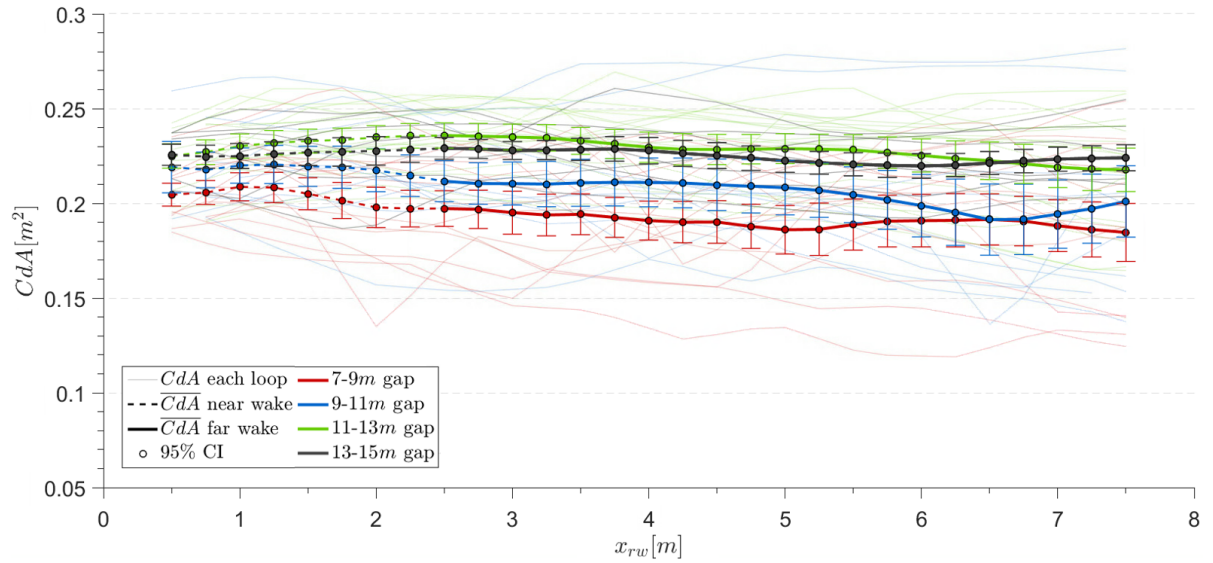


Figure 6.5: Streamwise CdA evolution in wake of trailing cyclist at 30 km h^{-1} under drafting conditions

The previous plot illustrates that the lowest drag area coefficient is achieved at drafting distances of 7–9 m, followed by the 9–11 m range. Interestingly, for the two largest separation distances this trend does not continue, as the 13–15 m zone indicates a smaller CdA value than the 11–13 m one. This behaviour is more elaborately discussed in the upcoming section 6.3. To assign one representative CdA value to each of the four drafting ranges, the region of 2.5–5.5 m behind the rear wheel is averaged. Further downstream, the algorithm becomes less reliable in clearly separating the wake of the trailing cyclist with the wake of the leading cyclist, which is noticeable in the larger dispersion and the tendency of lower drag area values of the CdA values per loop. Those mean values and their 95 % confidence interval, together with the average and the standard deviation of the drafting distance and the number of samples per zones can be obtained in table 6.1. The results of the 9–11 m and 13–15 m drafting distances in particular should be treated with care, as the sample pool size is small. The confidence interval for the drafting case is larger compared to the previously conducted Ring of Fire measurements and thus also larger than the individual cases. It spans ± 9 –9.5 %, which can be explained not only by the low sample pool size but also by the additionally added drafting distance parameter, including values within a 2 m range. Together with the turbulent flow behaviour behind the leading cyclist, wake inflow conditions will change for each transit and thus yield more dispersed CdA results.

Table 6.1: Drag area coefficient in the four drafting zones. Standard deviation of drafting distance in brackets.

Zone	$\overline{d_{drafting}} [m]$	$\overline{CdA} [m^2]$	95% CI [m^2]	# $_{samples} [-]$
7-9m	7.93 (0.78)	0.1915	0.1756-0.2074	16
9-11m	9.92 (0.61)	0.2096	0.1892-0.2300	10
11-13m	11.9 (0.58)	0.2312	0.2210-0.2414	17
13-15m	14.1 (1.39)	0.2260	0.2164-0.2356	8

6.3. COMPARISON CdA BETWEEN POWER METER AND RING OF FIRE

In this section, the comparison between power meter and Ring of Fire derived drag area coefficients is drawn, which was the main objective of this work. For this, both individual and drafting scenarios are considered, which cover a wide range of CdA values. The results are depicted in Figure 6.6, where the drag area values from the Ring of Fire, as well as from the power meter are plotted. For the power meter approach, two different rolling resistance coefficients are utilized to assess the sensitivity of this parameter, namely the literature based value of $C_{rr} = 0.0055$ and the coefficient derived from the linear regression, performed in section 6.1, $C_{rr} = 0.003$.

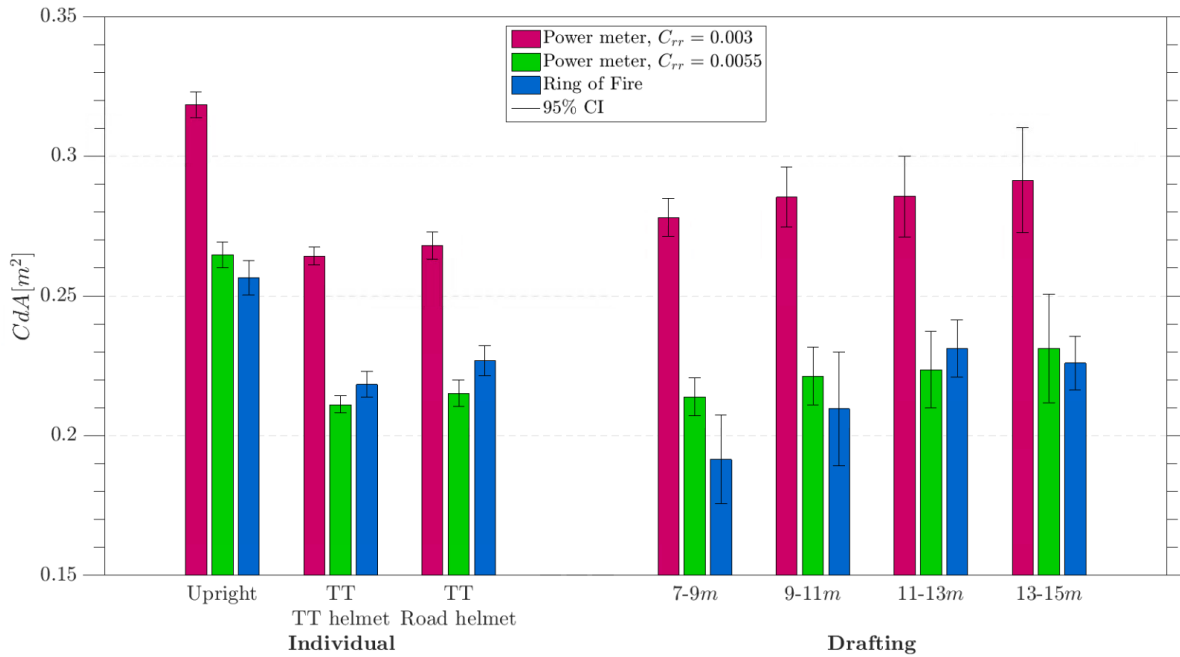


Figure 6.6: Comparison of drag area coefficients between power meter and Ring of Fire.

The preceding histogram can be studied in two different ways, namely by assessing the relative difference of the measurement techniques between each test condition, or by evaluating the absolute values of the predicted CdA . Considering the relative performance for the individual cases, the trends of the power meter and the Ring of Fire show good agreement, as a large-scale drag area increase from time-trial to upright position is obtained. While the Ring of Fire predicts an increase in CdA of 0.039 m^2 , the power meter results increase by 0.054 m^2 , regardless of the chosen rolling coefficient. Between the two helmet types a small-scale increase of 0.009 m^2 can be extracted from the Ring of Fire measurements, compared to a delta of 0.004 m^2 for the two power meter approaches. Regarding the absolute value, it becomes apparent how important a correctly chosen rolling resistance coefficient is, as the two shown C_{rr} values yield a ΔCdA of 0.053 m^2 , which amounts to 16–20%. At this point, it is clear that the power meter derived absolute value cannot be blindly trusted due to the high dependency on the underlying model constants, while the relative values are independent of the model, assuming a constant velocity of 30 km h^{-1} between all tests.

Table 6.2: $\overline{CdA}[m^2]$ with $\Delta\overline{CdA}[m^2]$ in brackets w.r.t to individual time-trial test with time-trial helmet

	Individual			Drafting [<i>m</i>]			
	Upright	TT TT helmet	TT Road helmet	7-9	9-11	11-13	13-15
PM, $C_{rr} = 0.003$	0.318 (+0.054)	0.264	0.268 (+0.004)	0.278	0.285	0.286	0.291
PM, $C_{rr} = 0.0055$	0.265 (+0.054)	0.211	0.215 (+0.004)	0.214	0.221	0.224	0.231
Ring of Fire	0.257 (+0.039)	0.218	0.227 (+0.009)	0.192	0.21	0.231	0.226

For the individual test, the power meter model, using the literature based C_{rr} of 0.0055, results in similar values as those obtained through the Ring of Fire measurements (within 5%). Both approaches suggest the drag area coefficient in upright position to be around 0.26 m^2 . This value is influenced by many factors, such as the rider's posture, rider's physical appearance, equipment and test conditions, such as freestream turbulence and relative velocity. Therefore, it is difficult to compare this value to available literature, where a CdA value for dynamic upright position in the range of $0.28\text{--}0.343\text{ m}^2$ is reported by [de Martino Norante \(2018\)](#) and [Barry et al. \(2014b\)](#), respectively, where the latter employed a force balance measurement in the wind tunnel. Both also reveal a drag area reduction of 13.6% and 17.5% when the tests are repeated in time-trial posture. This is in accordance with the reduction obtained from the power meter (20%) and the Ring of Fire (15%) in the current experiment.

The helmet change from time-trial to road type resulted in a drag increase of 2%, as measured by the power meter device and 4% for the Ring of Fire approach. This follows the general reported trend in literature that time-trial helmets are aerodynamically more efficient than road helmets, as reported in [Alam et al. \(2010\)](#), [Blair and Sidelko \(2009\)](#) and [Chowdhury et al. \(2014\)](#). For the Ring of Fire, the drag penalty of a road helmet amounts to approximately 0.4 N, compared to the time-trial helmet. [Blair and Sidelko \(2009\)](#) report a difference of 1–1.5 N between the two helmet types in their wind tunnel study. Rescaling the higher test velocity of 13.4 ms^{-1} to 8.3 ms^{-1} , the obtained Ring of Fire value falls within the rescaled range of 0.39–0.58 N. One could additionally argue that the Giant River TT helmet is a conservative time-trial helmet due to the truncated tail, which might lead to lower differences to the road helmet than a helmet with a longer tail. The confidence interval of the Ring of Fire helmet tests show marginal overlap, indicating that the road helmet would very likely be again tested worse than the time-trial helmet, which allows a high assurance in this observation.

The drafting test was conducted in time-trial position with road helmet and thus can be compared to the individual TT-Road helmet run. Under drafting conditions, the power meter does not suggest a CdA benefit when trailing behind another cyclist. However, as discussed in section 6.1 it is difficult to draw strong conclusions, due to the large confidence interval. The Ring of Fire, on the other hand, reliably predicts a reduction in drag area value for drafting distances of less than 9 m, compared to the single-rider test. One would expect a similar drag area coefficient when the same object, in this case the rider in TT position with road helmet, is tested. However, a change in aerodynamic efficiency could be explained by the changed inflow condition the trailing cyclist encounters under drafting. Here, the turbulence intensity is increased and the relative velocity is decreased, resulting in a changed Reynolds number, which could positively affect the flow over the cyclist. A Reynolds number dependency of the drag area coefficient in cycling is presented in the work of [Defraeye et al. \(2011\)](#), as shown in Figure 6.7.

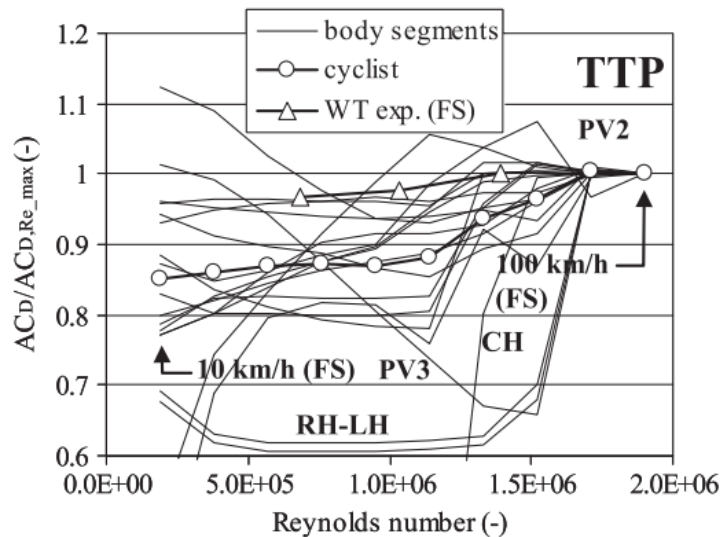


Figure 6.7: Reynolds number dependency of individual body parts and the entire cyclist as computed by numerical studies and a full scale wind tunnel experiment (all tests in TT position). Reproduced from Defraeye et al. (2011)

Considering a characteristic flow length scale equal to 1 m, as used in the study of Defraeye et al. (2011), and the corresponding relative velocities for the individual, 7–9 m and 11–13 m drafting range, the Reynolds numbers amount to: $5.5280 \cdot 10^5$, $4.6988 \cdot 10^5$ and $4.1460 \cdot 10^5$, respectively. Comparing those values to Figure 6.7 it is evident that they are located in a region with Reynolds number sensitivity, of both the individual body parts and the entire cyclist. It should be mentioned that the results of Defraeye et al. (2011) act more as an illustration of the Reynolds number dependency in cycling, rather than a comparison in absolute terms, as the graph is expected to change for different riders, equipment, and turbulence intensity levels, which are certainly present during drafting.

For the individual tests, it can be concluded that the relative drag area results of both measurement techniques compared in this work show good agreement when considering the ensemble average of all loops. Under drafting conditions, a direct comparison between the Ring of Fire method and the power meter is not meaningful as the latter is influenced by variant drafting distances throughout the lap and drafting effects during cornering, which are unknown.

6.4. DRAG SAVINGS UNDER DRAFTING CONDITION

The following discussion deals with the aerodynamic drag savings experienced in drafting conditions. As baseline, the individual time-trial test with road helmet is used, against which the drafting cases are compared. All five measurements are conducted at 30 km h^{-1} in time-trial position, utilizing the road helmet. Figure 6.8 displays the normalized drag area value with respect to the single-rider benchmark, as extracted from the Ring of Fire measurements. It should be noted that the 95 % confidence intervals of the drafting cases are computed with a fixed $CdA_{individual}$ value, which in itself has a small uncertainty.

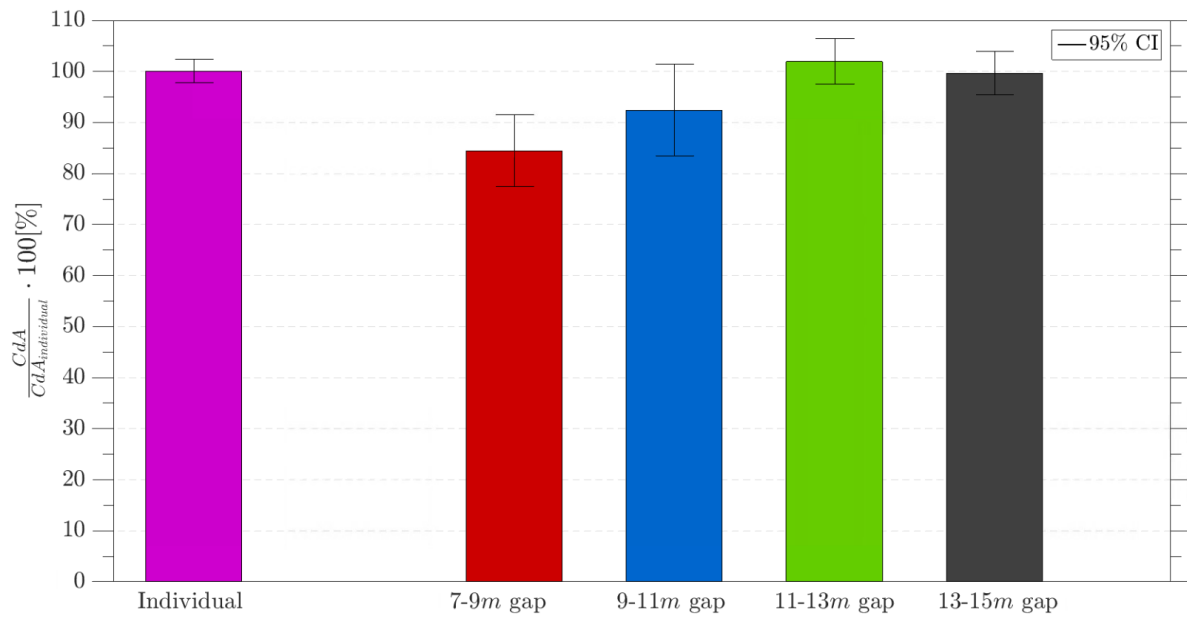


Figure 6.8: Drag area coefficient change in drafting conditions at 30 km h^{-1} as measured by the Ring of Fire

The previous Figure depicts a 15 % drag area saving in the drafting region of 7–9 m measured from front wheel to front wheel. 2 m further downstream the aerodynamic drag benefit reduces on average to 9 %, while at drafting distances beyond 11 m no benefit is measured. Even though in this region a velocity deficit is faced by the cyclist, as will be later shown in Figure 6.9c, the drag area coefficient is not favourable over the individual case.

To the best knowledge of the author, no academic research has yet been performed on drafting distances beyond 3 m. Olds et al. (1995) suggest negligible drag savings for larger drafting distances exceeding this number. This study, however, reveals a drag area saving of at least 10 % at 7–9 m using the upper limit of the 95 % confidence interval. It is difficult from the investigations performed at small separation distances to predict how the drafting benefit would develop at larger distances. Most recent studies by Barry et al. (2014a), Blocken et al. (2012) and Blocken et al. (2013) measure in time-trial position at 0.8 m, 1 m and 1 m, respectively and report a drag saving of 45 %, 30 % and 25 % for the trailing cyclist. Further, less relevant results of drafting studies can be obtained in table 2.1.

Non-peer reviewed sources such as Swissside (2017), report a drag saving of 13.4 % at drafting distances of 12 m as a result of a numerical study at 45 km h^{-1} . In the same test, a 7 m drafting distance was tested to lower the drag by 20.3 %, which would be comparable to the findings of the current experiment (15 %). A possible explanation for the absent drag savings at large separation distances in this study could be the Reynolds number dependency. As illustrated in Figure 6.7, local drag area plateaus can occur, which represent an insensitivity to the Reynolds number. Despite the decreased inflow velocity at 9–11 m drafting (Figure 6.9c), the Reynolds number dependent CdA might share the same plateau as the unaffected individual test. Additionally, at far drafting distances, the primary velocity deficit is downwashed and thus mostly affects the flow around the lower portion of the bike (Figure 6.9c). The cyclist him/herself, who contributes to around 60–80 % of the overall system drag (Defraeye et al. (2013), Blocken et al. (2013) and Crouch et al. (2017)), encounters a decreased velocity deficit that is in the range of 85–95 % of the freestream velocity only.

Highly hypothetically, one could expect a drag benefit in the 11–13 m range when testing at higher velocities, as the wake behind the leading cyclist has less time to diffuse until the trailing cyclist arrives and thus a more pronounced Reynolds number difference between leading and trailing cyclist would result. The tendency of Figure 6.7 shows a decreasing drag area coefficient at lower Reynolds numbers, which could result in a CdA value, beneficial for the trailing cyclist. As most flow studies around cyclists have shown, it is difficult to generalise the findings due to very individual Reynolds number dependency for each rider and each test conditions.

As a final remark, it should be added that the drafting effect, as investigated by Kyle (1979), Edwards et al. (2007) and Fitton et al. (2017), is furthermore dependent on the physical appearance of the lead cyclist. A rider with a small stature provides less shelter to the trailing cyclist than a larger one. In this experiment, a female athlete with a small stature led the male athlete, which needs to be considered when looking at the drag saving values.

6.5. FLOW TOPOLOGY UNDER DRAFTING CONDITIONS

In this section, the flow topology under drafting condition is compared to the single-rider case. This discussion is limited to the drafting regions of 7–9 m and 11–13 m, as most passages were performed within these two zones. Even though the laser line on the ground helped to guide the cyclist to the lateral centre of the tunnel, a manual correction method after de Martino Norante (2018) needed to be applied to laterally align all images with respect to the $y = 0\text{ m}$ coordinate.

6.5.1. MEAN OUT-OF-PLANE VELOCITY UPSTREAM

To start, the out-of-plane velocity in the inlet plane, 1.3–1.7 m upstream of the cyclist, is ensemble averaged. The results are normalized according to a reference frame that is moving with the cyclist, such that:

$$\overline{V_{x_{norm}}}(y, z) = \frac{\overline{V_x(y, z) + V}}{V} \quad (6.1)$$

, with V_x being the PIV-measured out-of-plane velocity component and V representing the cyclist's velocity. The flow field of the inlet planes are depicted in Figure 6.9. It should be noted that due to the close proximity of the inlet plane to the cyclist, the incoming rider is captured at the edge of the field of view, which cause spurious vector reconstruction. However, this region of the inlet plane is not important, as the rider transits the plane in the centre.

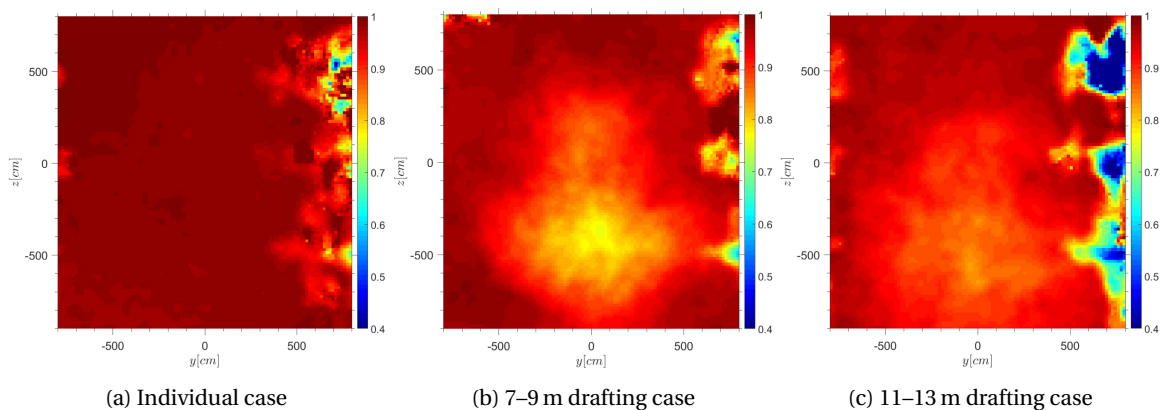


Figure 6.9: Normalized out-of-plane velocity 1.3–1.7 m upstream of cyclist

First to be observed in Figure 6.9a is the less than unity normalized out-of-plane velocity. This can be explained by the circulation forming in the testing facility, due to the continuing looping of the cyclist, which effectively induces a tail-wind component. Considering the drafting cases, an expected

trend is shown, in that the trailing cyclist faces a region of increased velocity deficit compared to a solo rider. The averaged wake velocity in the 7–9 m drafting case, shows its peak deficit to be around 75 % of the cyclist's velocity, while for 11–13 m the lowest velocity is found at 80 %. A comparative study by Barry et al. (2016a) manifests this observation, where a velocity deficit is measured just upstream of the trailing cyclist. In the previously mentioned paper, the authors find a peak velocity deficit of 10 % and 40 %, defined according to equation 6.1, at drafting distances of 1/11 bike length and 1 bike length, respectively (Figure 2.20). From Figure 6.9 it can be further stated, that the wake region in the closer drafting case is spatially more concentrated, while at further drafting distances a more expanded wake region is faced. The previous two observations underline the diffusive nature of the wake in downstream direction, in which it broadens and weakens. The wake behind the leading cyclist is furthermore downwashed, as can be obtained from image 6.9b and 6.9c. Given that the cyclist's body contributes to 60–80 % of the overall drag (Defraeye et al. (2013), Blocken et al. (2013) and Crouch et al. (2017)), it would likely be beneficial for drafting effects at large distances if the region of the velocity deficit would remain at the height of the rider.

6.5.2. MEAN OUT-OF-PLANE VELOCITY DOWNSTREAM

The following investigation deals with the ensemble-averaged out-of-plane velocity in the near wake of the individual and trailing cyclist. In order to capture a well-defined wake structure, acquired planes 0.4–0.6 m behind the cyclist of interest are considered. However, as mentioned before, the PIV vector reconstruction in this region is impaired by the low signal-to-noise ratios caused by the presence of the cyclist in the background of the field of view and the high flow turbulence. For this investigation, images with locally appearing SNR of below 3 are tolerated, while samples with large-scale patches consisting of worse SNR are discarded. The velocity field is once again normalized, according to equation 6.1.

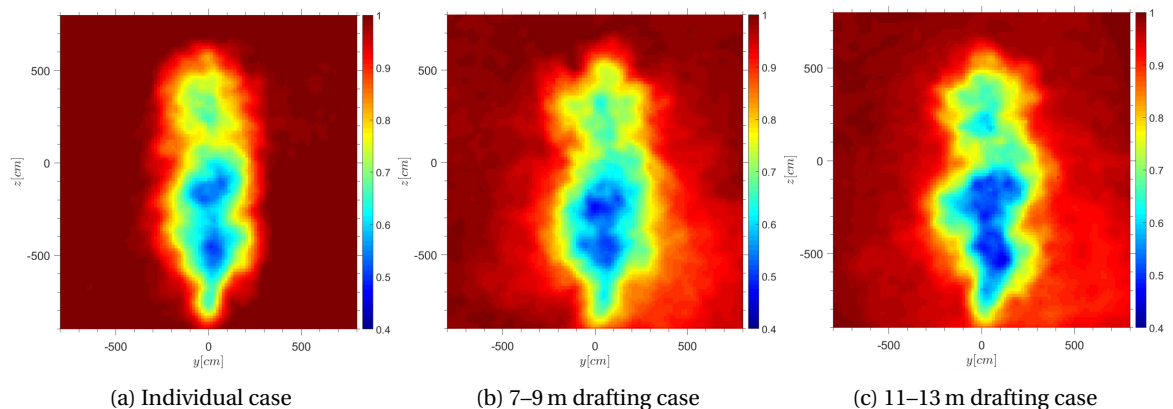


Figure 6.10: Normalized out-of-plane velocity 0.4–0.6 m downstream of cyclist

The mean streamwise velocity plots, shown in Figure 6.10, are comparable with each other, in that the shape and peak velocity deficit resemble each other. The narrowest part of the wake can be obtained near the ground, where the wheels of the bicycle are the main contributors. At increased heights, the wake structure broadens. Its peak velocity deficit can be found between $-600 \text{ cm} < z < 0 \text{ cm}$ in all three images, which is in line with the results from Barry et al. (2016a), in terms of location and magnitude. The reference study suggests a slight widening of the wake for the trailing cyclist, which cannot be strongly identified in the present results.

6.5.3. MEAN VORTICITY IN WAKE

To conclude, the flow topology investigation of the drafting cyclist, an averaged streamwise vorticity plot is provided in Figure 6.11. Once again, all considered planes are acquired between 0.4–0.6 m

downstream of the rear wheel. Previously conducted experiments shown in Figure 2.16 agree, that the dominant flow structures, emerging from the cyclist, originate in the hip region. This statement is clearly observed in Figure 6.11b, which shows the individual case. For the ease of comparison one reference plot is replotted in Figure 6.11a. Additional similarities between the individual and the reference case can be found, namely the head counter-rotating head vortex pair, which has not been observed prior to the Ring of Fire experiment of [de Martino Norante \(2018\)](#). Furthermore, distinct structures stemming from the lower hip, upper hip, and inner thighs can be identified. No conclusion can be drawn from the lower part of the wake structure, as the different pedal positions between the passages prohibit a consistent wake topology. The peak vorticity is increased compared to the reference case, likely due to an increased Reynolds number, which is 1.6 times higher in the current study.

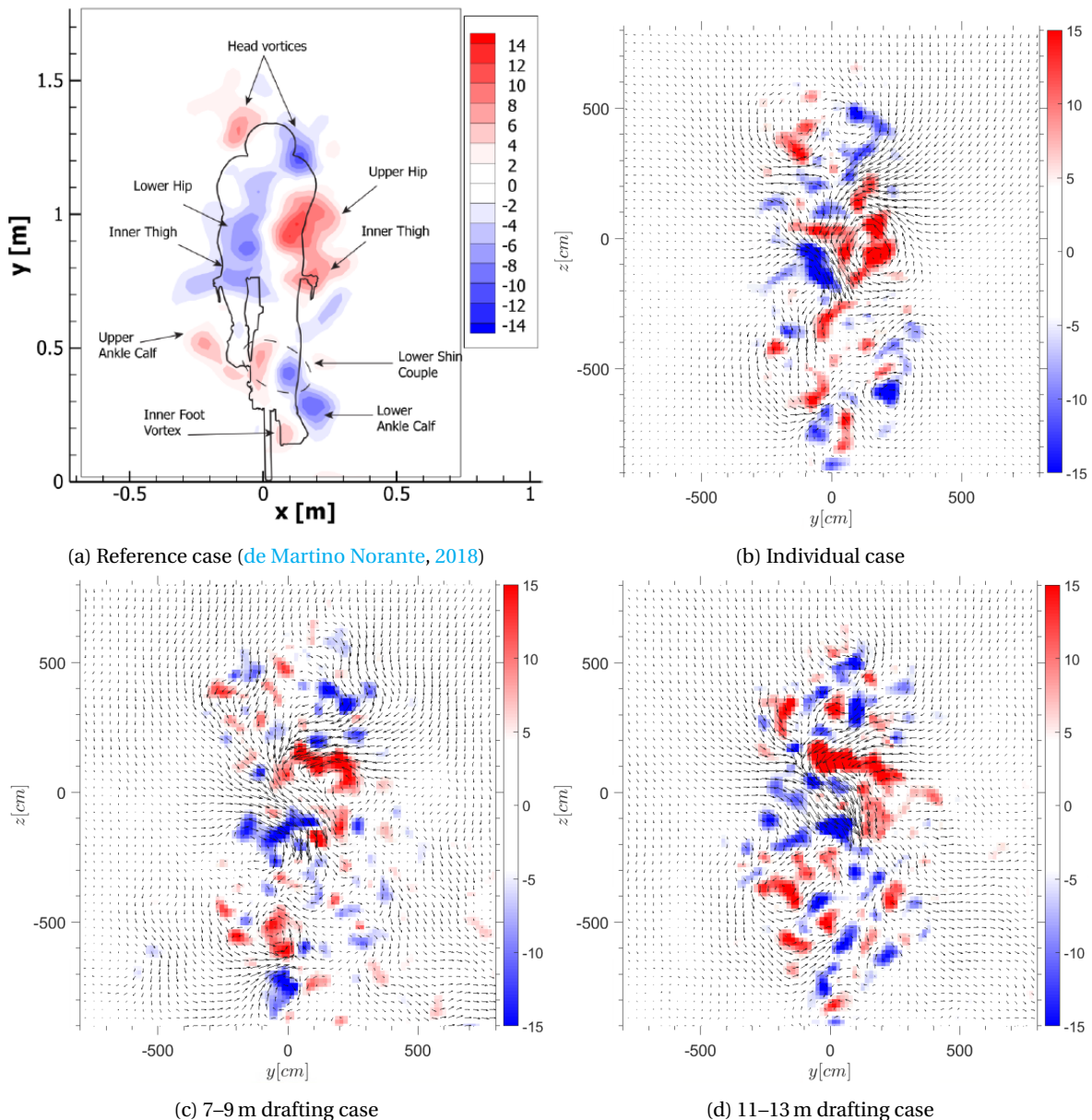


Figure 6.11: Streamwise vorticity 0.4–0.6 m downstream of cyclist

In the drafting cases, depicted in Figure 6.11c and 6.11d, the vortex structures are less coherent, as the sample pool size is small ($14 < n_{samples} < 18$) and the inconsistent inflow creates large variabil-

ity between the cases. Again, disregarding the lower portion of the wake, one can obtain that the region around $z = 0$ is dominated by two counter-rotating structures, which can be assigned to the hip/thigh region, as illustrated in Figure 2.24. Compared to the present study, Barry et al. (2016a) and Barry et al. (2016b) obtain more coherent and consistent wake structures, as these particular tests are conducted in a controlled water/wind tunnel environment at smaller drafting distances.

Next to the vorticity, one can also look at the in-plane velocity vectors, to assess the similarity between the flow field in isolated and drafting conditions. Here it becomes apparent that the primary features are consistent throughout Figures 6.11b, 6.11c and 6.11d, in that a strong downwash exist near the vertical centreline. It can be reasoned that this characteristic is responsible for the downward movement of the wake structure, as seen in Figure 6.10. Furthermore, a strong inwash between $0 \text{ cm} < z < 300 \text{ cm}$ is induced by the main hip vortices in all cases, which is further increased by the head vortices as present in Figure 6.11b. Image 2.25 suggests the hip/thigh vortex structure to outlast the smaller vortex structures, which in turn means that those will dominate the wake behaviour in the far wake. There, the induced inwash causes a narrowing of the upper wake, while the broadening of the lower wake structure can be assigned to the induced outwash by the vortex pair, as well as the present ground, which constrains the downwash, as illustrated in schematic 6.12. A narrow upper wake together with a broadened lower wake structure has already been observed by Spoelstra (2017) and de Martino Norante (2018) in the preceding Ring of Fire campaigns.

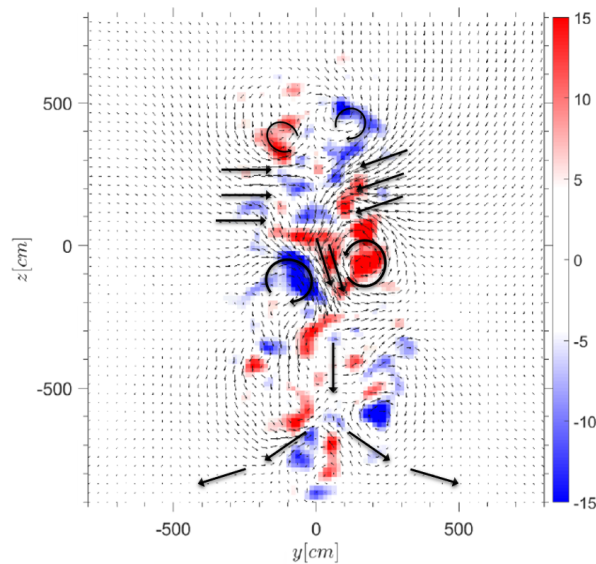


Figure 6.12: Schematic showing responsible flow features for downwashed wake, as well as upper wake narrowing and lower wake broadening.

7

CONCLUSION AND RECOMMENDATIONS

Two days of testing with professional cyclists in an indoor ice-rink were scheduled, during which continuous riding of a 190 m long loop aimed at a target velocity of 30 km h^{-1} was possible. The Ring of Fire system was kept in ongoing operation for 20 min at a time, to acquire around 40 transits of the cyclist through the measurement plane. Initially, the large-scale circulation within the hall, caused by the repeated looping, resulted in seeding problems, which were cured by walking a 2.8 m^2 blanket through the tunnel in opposite cycling direction after each transit.

The main objective of this Master's Thesis was to compare the drag area value of a cyclist obtained with the Ring of Fire technique against the CdA derived from simultaneously acquired power meter data. To assess the concordance between the two approaches in different regimes, three individual tests were performed to first create a large-scale drag area change by comparing upright to time-trial posture. Second, a small-scale CdA delta is investigated by replacing a time-trial helmet with a road helmet, while the posture between the two tests remained unchanged.

An attempt was made to evaluate the rolling resistance coefficient, adapting the approach of [Debraux et al. \(2011\)](#) under test conditions for utilization in the power meter model. However, the linear-regression-derived value under-predicts the rolling coefficient ($C_{rr} = 0.003$), compared to literature values for equally low tyre pressure ($C_{rr} = 0.0055$ according to [Wilson et al. \(2004\)](#) and [Grappe et al. \(1999\)](#)). Due to large power fluctuations between the corner and the straight parts the recordings of the power meter were averaged over one lap.

Regardless of the underlying rolling coefficient in the power meter model, both small- and large-scale deltas were well captured by both the Ring of Fire technique and the power meter approach and are in accordance with available literature values ([de Martino Norante \(2018\)](#), [Barry et al. \(2014b\)](#) and [Blair and Sidelko \(2009\)](#)). Between the time-trial and upright positions, a drag area increase of 0.039 m^2 and 0.054 m^2 , respectively, was determined. Replacing the time-trial helmet with the road helmet led to an increase in the CdA value of 0.009 m^2 and 0.004 m^2 , respectively. In terms of absolute drag area values the literature-based rolling coefficient of $C_{rr} = 0.0055$ shows good agreement in all three test conditions with the CdA numbers derived from the Ring of Fire (within 5%). The Ring of Fire derived drag area value for the upright position is 0.257 m^2 , while for the time-trial position with time-trial helmet the CdA amounts to 0.218 m^2 , and with the road helmet to 0.227 m^2 . In the same order, the power meter with $C_{rr} = 0.0055$ gives 0.265 m^2 , 0.211 m^2 and 0.215 m^2 .

In addition, drafting tests were conducted with a female athlete leading a male cyclist at distances between 7–15 m, measured from front wheel to front wheel. The power meter data in this scenario

have to be treated with care, as drafting effects during cornering are unknown. Additionally, the drafting distance between the cyclists was measured in one location only, but is prone to change throughout the lap, which causes large uncertainties. The Ring of Fire method, on the other hand, shows a clear trend towards lower drag area values at drafting distances below 9 m, which amount to a reduction of 15 %. In the range between 9–11 m, a smaller drag benefit can still be expected, whereas above 11 m, no gain was measured for the trailing cyclist. The observed behaviour is assigned to a reduction in Reynolds number due to lower relative velocities encountered by the drafting rider. The absence of drafting benefits at large separation distances is allocated to non-linear Reynolds number dependencies for a cyclist, as reported in literature (Blocken et al., 2013).

Considering the flow field, it can be concluded that the trailing cyclist encounters a slower velocity due to the wake of the leading rider. This velocity deficit mitigates at larger downstream distances and amounts to 75 % and 85 % of the cyclist velocity, at 7–9 m and 11–13 m, respectively. As already stated in Barry et al. (2016b), the wake in immediate vicinity behind the cyclist does not show noticeable differences between isolated and drafting scenarios. The vortex features behind the cyclist, captured in the individual case, show dominant hip/thigh and head structures comparable to those found in the previous Ring of Fire campaign by de Martino Norante (2018). The lower wake region cannot be compared due to the lack of phase-locked pedal position in this experiment. Behind the trailing cyclist, only dominant features in the hip/thigh region can be identified. Other structures are not coherent due to the high variability of testing conditions. Both individual and drafting flow fields show a downwashing behaviour behind the cyclist, as well as inwash at the upper wake, dominated by the hip/thigh vortices. Further downstream, this will lead to a downwash of the wake, with a narrowing of the upper wake and a broadening at the bottom, due to the ground constraint. At drafting distances beyond 7 m, the main velocity deficit is thus encountered by the lower part of the bike, rather than the cyclist him/herself who, according to literature, accounts for 60–80 % of the drag (Defraeye et al. (2013), Blocken et al. (2013) and Crouch et al. (2017)).

Based on the current campaign, recommendations can be given for future Ring of Fire tests. First, an investigation of the cyclist's upstream pressure propagation should be considered. So far, the pressure is either neglected or reference values from literature are utilized. Placing the acquisition cameras at the tunnel exit would allow for an unobstructed view of the inlet plane, benefiting the pressure reconstruction process. In this setup, the immediate wake region behind the cyclist would be compromised, and near-wake flow topologies could be challenging to retrieve. Two cameras on both tunnel entry and exit would solve this problem, however, it would also increase the complexity of the setup. Concerning the cameras at the tunnel exit, contamination of the lenses should be taken into consideration, as they face the entrained particles.

Furthermore, it is advised to equip the cyclist with a black suit to improve the pixel contrast, when the cyclist is present in the images. For the current campaign, an f-stop setting of 8 was selected, which attenuated the light intensity and consequently reduced the signal-to-noise ratio. It should be investigated whether or not a smaller f-stop setting would also provide sufficient view of depth.

To remove the walking process after each transit, a system should be designed to reduce the draft after acquisition. In the current experiment, an effort was made to block the flow with a 5 m² wall, placed either at the tunnel entry or exit, leading to unsatisfactory results. Closing off the entire tunnel entry/exit area for an endured time period may prove successful. The use of fans facing in opposite cycling direction should be treated with care, as additional turbulence is added into the flow.

Throughout the current project, an attempt was made to quantify the unsteady term of the momentum equation, which led to unreasonably high drag values. By logical reasoning, the unsteady effects in the present scenario were deemed disregarable. However, a simplified numerical case study could provide insight into the importance of this unsteady term.

In case another power meter study will be conducted, it is suggested to place the tunnel on a long straight to achieve more steady power traces before the transit. A future experiment at the Tom-Dumoulin-Bike-Park in Sittard is envisioned, which would provide such desirable track layout.

For future drafting tests, an improved system for indicating the target drafting distance to the trailing cyclist is proposed. Projecting a laser line, as planned in this campaign, is suggested. However, the saddle mount must be revised. More representative values for professional athletes could be derived from test at higher velocities ($40\text{--}45\text{ km h}^{-1}$), where drag savings at 12 m could be measurable.

BIBLIOGRAPHY

- R.J. Adrian. Dynamic ranges of velocity and spatial resolution of particle image velocimetry. *Measurement Science and Technology*, 8(12):pp. 1393–1398, 1997. doi: 10.1088/0957-0233/8/12/003.
- R.J. Adrian and J. Westerweel. *Particle Image Velocimetry*. Cambridge University Press, 2011.
- R.J. Adrian and Chung-Sheng Y. Pulsed laser technique application to liquid and gaseous flows and the scattering power of seed materials. *Applied Optics*, 24(1):pp. 44, 1985. doi: 10.1364/ao.24.000044.
- F. Alam et al. An experimental study of thermal comfort and aerodynamic efficiency of recreational and racing bicycle helmets. *Procedia Engineering*, 2(2):pp. 2413–2418., 2010. doi: 10.1016/j.proeng.2010.04.008.
- F. Alam et al. Aerodynamics of ribbed bicycle racing helmets. *Procedia Engineering*, 72:pp. 691–696., 2014. doi: 10.1016/j.proeng.2014.06.117.
- M. Allen. Image mark allen. <https://goo.gl/images/5Qh9Xp>, 1982. Accessed: 14.06.2018.
- J. D. Anderson. *Fundamentals of Aerodynamics*. McGraw-Hill Education, 2011.
- P. Baldissera et al. Rolling resistance, vertical load and optimal number of wheels in human-powered vehicle design. *Proceedings of the IMechE*, 231(1):pp. 33–42., 2017. doi: 10.1177/1754337115625002.
- N. Barry et al. Effect of crosswinds and wheel selection on the aerodynamic behavior of a cyclist. *Procedia Engineering*, 34:pp. 20–25., 2012. doi: 10.1016/j.proeng.2012.04.005.
- N. Barry et al. The effect of spatial position on the aerodynamic interactions between cyclists. *Procedia Engineering*, 72:pp. 774–779., 2014a. doi: 10.1016/j.proeng.2014.06.131.
- N. Barry et al. Aerodynamic performance and riding posture in road cycling and triathlon. *Proceedings of the Institution of Mechanical Engineers*, 229:pp. 28–38., 2014b. doi: 10.1177/1754337114549876.
- N. Barry et al. Aerodynamic drag interactions between cyclists in a team pursuit. *Sports Engineering*, 18(2):pp. 93–103., 2015. doi: 10.1007/s12283-015-0172-8.
- N. Barry et al. Flow field interactions between two tandem cyclists. *Experiments in Fluids*, 57(12), 2016a. doi: 10.1007/s00348-016-2273-y.
- N. Barry et al. An analysis of the wake of pedalling cyclists in a tandem formation. *Procedia Engineering*, 147:pp. 7–12., 2016b. doi: 10.1016/j.proeng.2016.06.181.
- F. Beaumont et al. Aerodynamic study of time-trial helmets in cycling racing using cfd analysis. *Journal of Biomechanics*, 67:pp. 1–8., 2018. doi: 10.1016/j.jbiomech.2017.10.042.
- M. Belloli et al. Drafting effect in cycling: Investigation by wind tunnel tests. *Procedia Engineering*, 147:pp. 38–43., 2016. doi: 10.1016/j.proeng.2016.06.186.

- N. Belluye et al. Approche biomécanique du cyclisme moderne, données de la littérature. *Science & Sports*, 16(2):pp. 71–87., 2001. doi: 10.1016/S0765-1597(01)00049-1.
- W. Betrucci et al. Validity and reliability of the powertap mobile cycling powermeter when compared with the srm device. *International journal of sports medicine*, 26(10):pp. 868–873., 2005. doi: 10.1055/s-2005-837463.
- K.B. Blair and S. Sidelko. *Aerodynamic Performance Of Cycling Time Trial Helmets. (P76)*. Springer, 2009.
- B. Blocken et al. Rans and les simulations of the interference drag of two cyclists. In Hai-Fan Xiang, Yao-Jun Ge, and Shu-Yang Cao, editors, *7th International Colloquium on Bluff Body Aerodynamics and Applications (BBAA7), September 2-6, 2012, Shanghai, China*, pages 1–10. China Communication Press, 2012. ISBN 978-7-900265-90-6.
- B. Blocken et al. Cfd simulations of the aerodynamic drag of two drafting cyclists. *Comput. Fluids*, 71:pp. 435–445., 2013. doi: 10.1016/j.compfluid.2012.11.012.
- B. Blocken et al. Aerodynamic benefit for a cyclist by a following motorcycle. *Journal of Wind Engineering and Industrial Aerodynamics*, 155:pp. 1–10., 2016. doi: 10.1016/j.jweia.2016.04.008.
- J. Bosbach et al. Large scale particle image velocimetry with helium filled soap bubbles. *Experiments in Fluids*, 46(3):pp. 539–547., 2008. doi: 10.1007/s00348-008-0579-0.
- J.P. Broker et al. Racing cyclist power requirements in the 4000-m individual and team pursuits. *Medicine and Science in Sports and Exercise*, 31(11):p. 1677, 1999. doi: 10.1097/00005768-199911000-00026.
- L. Brownlie et al. The wind-averaged aerodynamic drag of competitive time trial cycling helmets. *Procedia Engineering*, 2(2):pp. 2419–2424., 2010. doi: 10.1016/j.proeng.2010.04.009.
- E. Burke. *High-Tech Cycling*. Human Kinetics, 2003.
- H. Chowdhury et al. An experimental study on aerodynamic performance of time trial bicycle helmets. *Sports Engineering*, 17(3):pp. 165–170., 2014. doi: 10.1007/s12283-014-0151-5.
- T.N. Crouch et al. Flow topology in the wake of a cyclist and its effect on aerodynamic drag. *Journal of Fluid Mechanics*, 748:pp. 5–35., 2014. doi: 10.1017/jfm.2013.678.
- T.N. Crouch et al. Dynamic leg-motion and its effect on the aerodynamic performance of cyclists. *Journal of Fluids and Structures*, 65:pp. 121–137., 2016a. doi: 10.1016/j.jfluidstructs.2016.05.007.
- T.N. Crouch et al. A comparison of the wake structures of scale and full-scale pedalling cycling models. *Procedia Engineering*, 147:pp. 13–19., 2016b. doi: 10.1016/j.proeng.2016.06.182.
- T.N. Crouch et al. Riding against the wind: a review of competition cycling aerodynamics. *Sports Engineering*, 20:pp. 81–110., 2017. doi: 10.1007/s12283-017-0234-1.
- K. Dahn et al. Frictional resistance in bicycle wheel bearings. *Cycling Science*, 3(1):pp. 28–32., 1991.
- L. de Martino Norante. Advances and assessment of the ring of fire concept for on-site cycling aerodynamics. Master’s Thesis, 2018.
- P. Debraux et al. Aerodynamic drag in cycling: methods of assessment. *Sports Biomechanics*, 10(3): pp. 197–218., 2011. doi: 10.1080/14763141.2011.592209.

- N.G. Deen et al. On image pre-processing for piv of single- and two-phase flows over reflecting objects. *Experiments in Fluids*, 49(2):pp. 525–530., 2010. doi: 10.1007/s00348-010-0827-y.
- T. Defraeye et al. Computational fluid dynamics analysis of drag and convective heat transfer of individual body segments for different cyclist positions. *Journal of Biomechanics*, 44(9):1695–1701, 2011. doi: 10.1016/j.jbiomech.2011.03.035.
- T. Defraeye et al. Cyclist drag in team pursuit: Influence of cyclist sequence, stature, and arm spacing. *Journal of Biomechanical Engineering*, 136(1):011005–1/9, 2013. doi: 10.1115/1.4025792.
- P.E. Di Prampero. Cycling on earth, in space, on the moon. *European journal of applied physiology*, 82(5-6):345–360, 2000. doi: 10.1007/s004210000220.
- S. Duc et al. Validity and reproducibility of the ergomo@pro power meter compared with the srm and powertap power meters. *International Journal of Sports Physiology and Performance*, 2(3): 270–281, 2007. doi: 10.1123/ijsp.2.3.270.
- A.G. Edwards et al. Aerodynamic characteristics as determinants of the drafting effect in cycling. *Medicine and Science in Sports and Exercise*, 39(1):pp. 170–176., 2007. doi: 10.1249/01.mss.0000239400.85955.12.
- D. Engler Faleiros et al. Helium-filled soap bubbles tracing fidelity in wall-bounded turbulence. *Experiments in Fluids*, 59(3):56, 2018. doi: 10.1007/s00348-018-2502-7.
- B. Fitton et al. The impact of relative athlete characteristics on the drag reductions caused by drafting when cycling in a velodrome. *Proceedings of the Institution of Mechanical Engineers, Part P: Journal of Sports Engineering and Technology*, 232(1):pp. 39–49., 2017. doi: 10.1177/1754337117692280.
- J. Garcia-Lopez et al. The use of velodrome tests to evaluate aerodynamic drag in professional cyclists. *International Journal of Sports Medicine*, 35(5):pp. 451–455., 2013. doi: 10.1055/s-0033-1355352.
- N. Gardan et al. Numerical investigation of the early flight phase in ski-jumping. *Journal of Biomechanics*, 59:pp. 29–34., 2017. doi: 10.1016/j.jbiomech.2017.05.013.
- D. Giaquinta. Flow topology of ahmed body. Master's Thesis, 2018.
- G. Gibertini and D. Grassi. *Cycling aerodynamics*. Springer Vienna, 2008.
- J.W Goodman. *Introduction to Fourier optics*. Roberts and Company Publishers, 2004.
- F. Grappe et al. Aerodynamic drag in field cycling with special reference to the obree's position. *Ergonomics*, 40(12):pp. 1299–1311., 1997. doi: 10.1080/001401397187388.
- F. Grappe et al. Influence of tyre pressure and vertical load on coefficient of rolling resistance and simulated cycling performance. *Ergonomics*, 42(10):pp. 1361–1371., 1999. doi: 10.1080/001401399185009.
- M.D. Griffith et al. Computational fluid dynamics study of the effect of leg position on cyclist aerodynamic drag. *Journal of Fluids Engineering*, 136(10):pp. 101105., 2014. doi: 10.1115/1.4027428.
- M. Hilger. Image patrick lange aerobar scan. <https://bikerumor.com/2018/10/11/project-101-canyon-swiss-side-sauber-3d-print-titanium-aerobar-extensions/>, 2018. Accessed: 17.11.2018.

- H. Hill. Image norman stadler. <https://www.flickr.com/photos/46340536@N03/4263038353>, 2006. Accessed: 14.06.2018.
- H. Hinzen et al. Wirkungsgrad von fahrradantrieben. Lehre und Forschung, Hochschule Trier, Hochschulreport, 2012.
- Ironman. Ironman 2018 competition rules. Regulations, 2018.
- C. Jux et al. Robotic volumetric piv of a full-scale cyclist. *Experiments in Fluids*, 59(4), 2018. doi: 10.1007/s00348-018-2524-1.
- T.M. Kawamura. Wind drag of bicycles. Report No.1, Tokyo University, 1953.
- R. D. Keane and R.J. Adrian. Optimization of particle image velocimeters. part i. double pulsed systems. *Measurement Science and Technolgy*, 1(11), 1990. doi: 10.1088/0957-0233/1/11/013.
- D.F Kurtulus et al. Unsteady aerodynamic forces estimation on a square cylinder by tr-piv. *Exp Fluids*, 42(2):pp. 185–196., 2007. doi: 10.1007/s00348-006-0228-4.
- C.R. Kyle. Reduction of wind resistance and power output of racing cyclists and runners travelling in groups. *Ergonomics*, 22(4):pp. 387–397., 1979. doi: 10.1080/00140137908924623.
- C.R. Kyle. *Selecting Cycling Equipment*. Human Kinetics, 2003.
- C.R. Kyle et al. Improving the racing bicycle. *Mechanical Engineering*, 106(9):pp. 34–35., 1984.
- C.R. Kyle et al. Rolling resistance. *Bicycling*, pages pp. 141–152., May 1985.
- C.R. Kyle et al. The mechanical efficiency of bicycle derailleur and hub-gear transmissions. *Human Power*, 52:pp. 3–11., 2001.
- C.R. Kyle et al. Aerodynamics of human-powered vehicles. *Proceedings of the Institution of Mechanical Engineers Part A: Journal of Power and Energy* 218, 218(3):pp. 141–154., 2004. doi: 10.1243/095765004323049878.
- J. Lafford. Rolling resistance of bicycle tyres. *Human Power*, 50:pp. 14–19., 2000.
- N.J. Lawson et al. Three-dimensional particle image velocimetry: Error analysis of stereoscopic techniques. *Measurement Science and Technology*, 8(8):pp. 894–900., 1997. doi: 10.1088/0957-0233/8/8/010.
- A.C. Lim et al. Measuring changes in aerodynamic/rolling resistances by cycle-mounted power meters. *Medicine & Science in Sports & Exercise*, 43(5):pp. 853–860., 2011. doi: 10.1249/MSS.0b013e3181fcb140.
- R. Lukes et al. An analytical model for track cycling. *Proceedings of the Institution of Mechanical Engineers, Part P: Journal of Sports Engineering and Technology*, 226(2):pp. 143–151., 2012. doi: 10.1177/1754337111433242.
- J.C. Martin et al. Validation of a mathematical model for road cycling power. *Journal of Applied Biomechanics*, 14(3):pp. 276–291., 1998. doi: 10.1123/jab.14.3.276.
- R. Michels. *Verständnis des mikroskopischen Ursprungs der Lichtstreuung in biologischem Gewebe*. PhD dissertation, Universität Ulm, 2010.
- A. Mohebbian et al. Assessment of the derivative-moment transformation method for unsteady-load estimation. *Exp Fluids*, 53(2):pp. 318–330., 2012. doi: 10.1007/s00348-012-1290-8.

- T.S. Olds et al. Modeling road-cycling performance. *Journal of Applied Physiology*, 78(4):pp. 1596–1611., 1995. doi: 10.1152/jappl.1995.78.4.1596.
- T.S. Olds et al. Modelling human locomotion. *Sports Medicine*, 31(7):pp. 497–509., 2001. doi: 10.2165/00007256-200131070-00005.
- L. Passfield et al. Knowledge is power: Issues of measuring training and performance in cycling. *Journal of Sports Sciences*, 35(14):1426–1434, 2017. doi: 10.1080/02640414.2016.1215504.
- A.K. Prasad. Stereoscopic particle image velocimetry. *Experiments in Fluids*, 29(2):103–116, 2000. doi: 10.1007/s003480000143.
- Quantel. datasheet evergreen v5. https://www.quantel-laser.com/tl_files/client/MY%20QUANTEL%20SPACE/Sales%20Literature/EverGreen_Specs_EN_072015.pdf, 2015. Accessed: 2018-09-28.
- J.C. Quintana-Duque et al. Estimation of torque variation from pedal motion in cycling . *International Journal of Computer Science in Sport*, 14(1), 2015.
- M. Raffel et al. *Particle Image Velocimetry: A Practical Guide*. Springer International Publishing, 2007.
- M. Rauschendorfer. Image sebastian kienle. <https://www.stern.de/sport/sportwelt/sebastian-kienle--volles-risiko-beim-ironman-hawaii-2017-7659548.html>, 2017. Accessed: 14.06.2018.
- M. Rauschendorfer. Image patrick lange with new cockpit. <https://www.tri2b.com/triathlonnews/detail/gallery/articles/15/article/kona-2018-fotostory-6-patrick-lange-testet-sein-neues-cockpit-8375/>, 2018. Accessed: 17.11.2018.
- B. Rohloff et al. Efficiency measurements of bicycle transmissions - a neverending story? *Human Power*, 55:pp. 412–417., 2004. doi: 10.1016/j.proeng.2015.07.217.
- M. Samimy et al. Motion of particles with inertia in a compressible free shear layer. *Physics of Fluids A: Fluid Dynamics*, 3:pp. 1915–1923., 1991. doi: 10.1063/1.857921.
- F. Scarano et al. On the use of helium-filled soap bubbles for large-scale tomographic piv in wind tunnel experiments. *Experiments in Fluids*, 56(2), 2015. doi: 10.1007/s00348-015-1909-7.
- A. Sciacchitano et al. A quantitative flow visualization technique for on-site sport aerodynamics optimization. *Procedia Engineering*, 112:pp. 412–417., 2015. doi: 10.1016/j.proeng.2015.07.217.
- Y. Shah. Drag analysis of full scale cyclist model using large-scale 4d-ptv. Master's Thesis, 2017.
- U. Shavit et al. Intensity capping: a simple method to improve cross-correlation piv results. *Experiments in Fluids*, 42(2):pp. 225–240, 2006. doi: 10.1007/s00348-006-0233-7.
- Bradford W. Sims et al. Aerodynamic bicycle helmet design using a truncated airfoil with trailing edge modifications. *Fluids and Thermal Systems; Advances for Process Industries*, 6(Parts A and B), 2011. doi: 10.1115/imece2011-65411.
- J. Spicer et al. On the efficiency of bicycle chain drives. *Human Power*, 50:pp. 3–9., 2000.
- A. Spoelstra. Aerodynamics of transiting objects via large-scale piv - the ring of fire concept. Master's Thesis, 2017.

- A. Spoelstra et al. The ring of fire for in-field sport aerodynamic investigation. *Proceedings*, 2(6), 2018. doi: 10.3390/proceedings2060221.
- SRM. Technical data srm powermeter. http://www.srm.de/fileadmin/user_upload/images/support/manuals/TechnicalDetails/powermeter_powercontrol/technical_data_powercontrol_powermeter_en.pdf, 2010. Accessed: 2018-09-29.
- Swisside. Drafting - how far is close enough? www.swisside.com/blogs/news/the-deal-with-drafting, 2017. [Online; accessed 24-July-2018].
- W. Terra et al. Evaluation of aerodynamic drag of a full-scale cyclist model by large-scale tomographic-piv., 2016. [International Workshop on Non-Intrusive Optical Flow Diagnostics].
- W. Terra et al. Aerodynamic drag of a transiting sphere by large-scale tomographic-piv. *Experiments in Fluids*, 58(7), 2017. doi: 10.1007/s00348-017-2331-0.
- A.Í. Torre et al. Aerodynamics of a cycling team in a time trial: Does the cyclist at the front benefit? *European Journal of Physics*, 30(6):pp. 1365–1369., 2009. doi: 10.1088/0143-0807/30/6/014.
- UCI. Clarification guide of the uci technical regulation. Regulations, 2018.
- L. Underwood. *Aerodynamics of Track Cycling*. PhD dissertation, University of Canterbury, 2012.
- L. Underwood et al. Helmet position, ventilation holes and drag in cycling. *Sports Engineering*, 18(4):pp. 241–248., 2015. doi: 10.1007/s12283-015-0181-7.
- B.W. van Oudheusden. Piv-based pressure measurement. *Measurement Science and Technology*, 24(3), 2013. doi: 10.1088/0957-0233/24/3/032001.
- F. Wechsel. Image ironman hawaii 2017 pro peleton. <https://tri-mag.de/szene/profi-starterlisten-fuer-ironman-hawaii-2018-146345/pros-fuer-den-13-oktober>, 2017. Accessed: 17.11.2018.
- J. Westerweel. *Digital Particle Image Velocimetry. Theory and Practice*. PhD dissertation, Delft University of Technology, 1993.
- J. Westerweel and F. Scarano. Universal outlier detection for piv data. *Experiments in Fluids*, 39(6): pp. 1096–1100., 2005. doi: 10.1007/s00348-005-0016-6.
- B. Wieneke. Stereo-piv using self-calibration on particle images. *Experiments in Fluids*, 39(2):pp. 267–280., 2005. doi: 10.1007/s00348-005-0962-z.
- B. Wieneke, editor. *Adaptive PIV with variable interrogation window size and shape*, 2010.
- C. Willert. Stereoscopic digital particle image velocimetry for application in wind tunnel flows. *Measurement Science and Technology*, 8(12):pp. 1465–1479., 1997. doi: 10.1088/0957-0233/8/12/010.
- D.G. Wilson, J. Papadopoulos, and E.R. Whitt. *Bicycling science*. MIT Press, 2004.
- J. Wu et al. Unsteady fluid-dynamic force solely in terms of control-surface integral. *Physics of Fluids*, 17(9), 2005. doi: 10.1063/1.2055528.
- M.M. Zdravkovich et al. Effect of cyclist's posture and vicinity of another cyclist on aerodynamic drag. *The Engineering of Sport*, page pp. 21–28., 1996.

A

SEEDING PROBLEM INDUCED BY CIRCULATION

Throughout preliminary tests with the amateur cyclist, it became apparent that the circulation in the hall induced by the cyclist causes the soap bubbles to be entrained downstream, as soon as they were produced by the seeding rake (Figure A.1). This caused inhomogeneous and insufficient seeding in the measurement plane located downstream with the tracers agglomerate on the right hand side, as can be seen in Figure A.2.



Figure A.1: Bubbles carried downstream immediately after production by seeding rake



Figure A.2: Initial seeding distribution in measurement plane

To stop the bubbles from exiting the tunnel and distribute the tracers more evenly in the measurement plane, three different approaches were tested. For the first two attempts a movable wall-like structure was constructed using large mats, which were stacked vertically on a small wagon, resulting in wall dimensions of 2.5 m height and 2 m width. After each passage, the wall was wheeled onto the track to block the circulation caused by the cyclist. Before the cyclist approached, the structure was retrieved. The wall structure was tested once at the entry and once at the exit, whereas neither approaches yielded satisfying seeding distributions. As a third approach, two mats were connected to a rod, which was carried through the tunnel slowly after each passage in opposite cycling direction by one of the operators, as shown in Figure A.3. It has been found that this procedure results in an homogeneous and sufficient seeding distribution in the measurement plane (Figure A.4) and was thus added to the measurement procedure for the rest of the campaign. The mats were later replaced by a lighter blanket with dimensions of 1.8 m x 1.55 m to reduce the human effort.



Figure A.3: Mats and later blanket carried by one operator in opposite cycling direction to reduce circulation effect in tunnel



Figure A.4: Improved seeding distribution in measurement plane due to reduced circulation

B

SAMPLE CODE FOR WAKE CONTOURING PROCEDURE

```
clear all; close all; clc;

% --- Create sample matrix with out-of-plane velocities
size_m = 10; % Define dimensions of sample matrix
v_lower = -8; % Lowest_expected_velocity [m/s]
v_higher = 2; % Highest_expected_velocity [m/s]
Vx_sample = v_lower + (v_higher-v_lower).*rand(size_m,size_m); % Fill sample matrix

% ---3 parameters that define the wake contouring---
percentile = 2; % Percentile to determine "maximum value" (Avoids outliers)
p = 50; % Percentage of maximum value, defining the initial wake boundary [%]
gaussian = 3; % Number of gaussian filter operations (higher -> dilates wake more)

% --- Find cut-off velocity ---
% -----
Cutoff_velocity = p/100*prctile(Vx_sample(:),percentile); % Defines cut-off velocity
Vx_0=Vx_sample; % Save original matrix on variable Vx_0
Vx_sample(Vx_sample>Cutoff_velocity)=0; % Set all values above cut-off velocity to 0
Vx_sample(Vx_sample<Cutoff_velocity)=1; % Set all values below cut-off velocity to 1
% -----
% -----

% --- Isolate largest island ---
% -----
I = bwlabel(Vx_sample,4); % Check 4 neighbours if Vx_sample>0 and cluster cells
stats = regionprops(I,'area'); % Determines number of cells included in each cluster
[~,I_largest] = max([stats.Area]); % Define which cluster/island is largest
Vx_logical = I == I_largest; % Returns logical matrix (Largest island=1 / rest=0)

% Convert logical matrix into numeric matrix
for a=1:size_m % march through matrix in horizontal direction
    for b=1:size_m % march through matrix in vertical direction
```

```

    if Vx_logical(a,b)==true
        Vx_filter(a,b)=1;    % Cells within largest island are set to 1
    else
        Vx_filter(a,b)=0;    % Cells outside largest island are set to 0
    end
end
end
% -----
% -----

% --- Dilate wake ---
% -----
h = fspecial('gaussian'); % Defines 2-D filter as 3x3 gaussian
for i=1:gaussian          % Repeat gaussian filter operation as defined by user
    Vx_filter = filter2(h, Vx_filter); % Apply gaussian filter on sample matrix
end
Vx_filter(Vx_filter>0)=1; % Set cells>0 (affected by gaussian filter) to 1
% -----
% -----

% --- Apply contour to original image ---
% -----
Vx_final=Vx_filter.*Vx_0; % Multiply filter matrix with original matrix
Vx_final(Vx_final>0)=0;   % Set all values above 0 to 0
% -----
% -----

```